# Representing the Fate of Springtime Arctic Clouds

by

Erika L. Roesler

A dissertation submitted in partial fulfillment
of the requirements for the degree of
Doctor of Philosophy
(Atmospheric, Oceanic, and Space Sciences)
in The University of Michigan
2012

Doctoral Committee:

Assistant Professor Derek J. Posselt, Chair
Assistant Professor Sarah M. Aciego
Assistant Professor Mark G. Flanner
Professor Joyce E. Penner
Professor Richard B. Rood

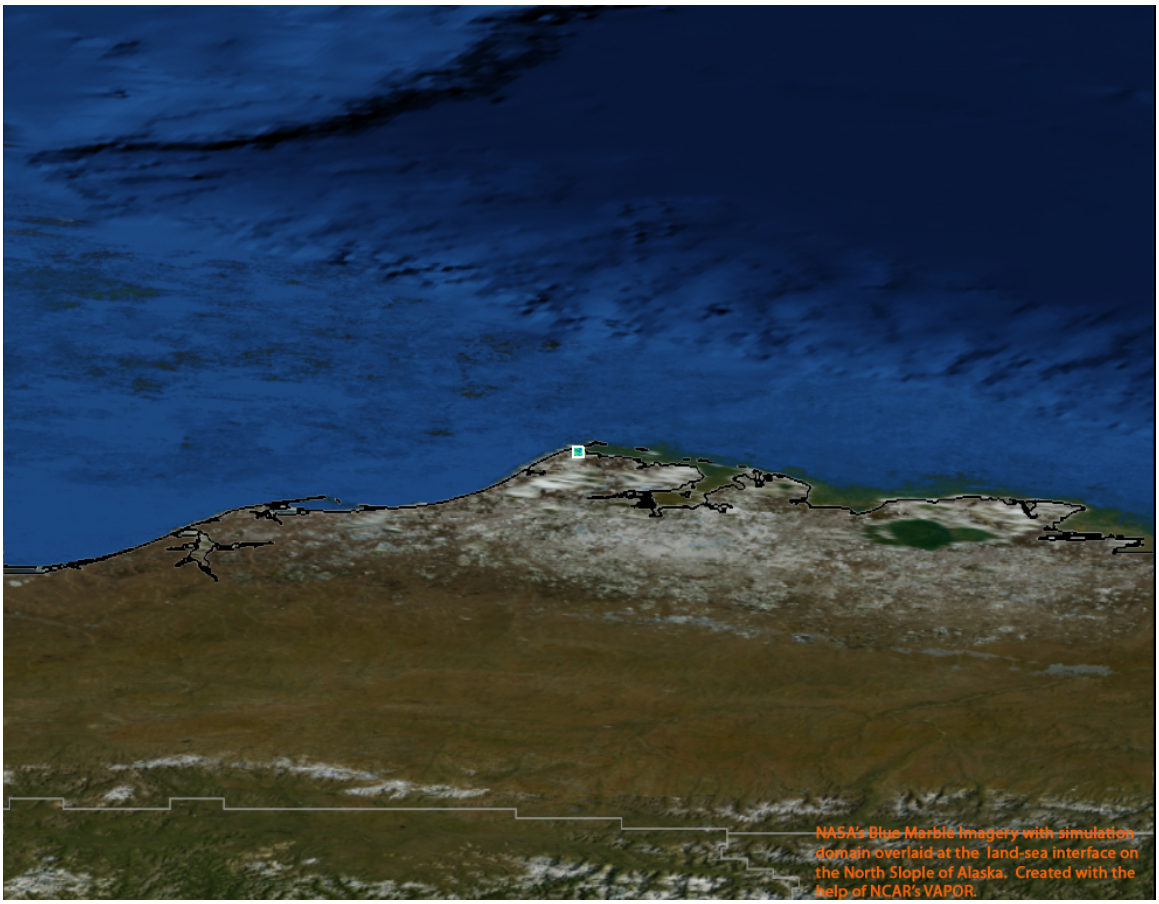


Somewhere, something incredible is waiting to be known.

–Carl Sagan

To Everett and Eric

# ACKNOWLEDGEMENTS

Many people and institutions deserve acknowledgement and recognition for their help, whether willing or unknowingly, in compiling this dissertation. Starting from where the paper hits the pad, I would like to thank other graduate students at the University of Michigan who put together a nice LaTeX template for me to use. I would like to acknowledge my experience at Eastern Michigan University, which was humbling. I now know to never use Microsoft Word to produce large, complex documents. I would like to thank Prof. James Sheerin of Eastern Michigan University for encouraging me to go further in my education, apply to Ph.D. programs, and for being so supportive. I would like to thank Dr. Ed Nam of the National Vehicle and Fuel Emissions Laboratory of the Environmental Protection Agency for his encouragement and help when I was working with models and large data sets for the first time.

At the University of Michigan, I would like to recognize the staff at the Center for Advanced Computing for their hard work in helping me get new software running, parallel simulations started, and for answering the heap seemingly unintelligent questions I threw at them. I would like to thank Professors Richard B. Rood, Joyce E. Penner, and R. Paul Drake for being excellent mentors from the start of graduate school. Thank you for challenging me and for your patience. I would like to thank Dr. Natalia Andronova for her encouragement, friendship, guidance, and for never giving up on students. I smile thinking of our egg breakfasts with coffee and lemons while talking about engineering climate change. Thank you Melissa Terwilliger, Bryan White, and Faye Ogasawara for tech support, starting my palate for raw fish, and sharing many things on the internet. Thank

you to Professor Derek Posselt for teaching me about 'grep' and other computing goodies, libraries, linking, including, and atmospheric science. Thank you for looking at the code, taking an interest in this work from the beginning, and for allowing me to be in Albuquerque to finish this degree. Thanks for your sharing your enthusiasm in science and for being a great role model. I would also like to thank the thesis committee for their time and valuable help with the dissertation document and defense.

At Pacific Northwest National Laboratory, I would like to thank Dr. Mikhail Ovchinnikov for his help in getting the model started which included initial data files and most of the parameterizations in the model. Thank you for letting me emulate your work as I became more familiar with numerical modeling. Thank you, Dr. Steve Ghan, for your hospitality in Richland, for helping me in this research by providing direction, ideas, and encouragement.

At Sandia National Laboratories in Albuquerque, New Mexico, I would like to thank Dr. Mark Taylor for giving me a glimpse into the world of high resolution climate models and for your support in my research. I appreciate the "climate group" meetings and how nice it was to talk about the climate at Sandia. I would also like to thank Dr. Michael Levy and Dr. Keith Dalbey for their help in navigating the computing world at the lab, specifically getting started on Redsky and with Design Analysis Kit for Optimization and Terascale Applications (DAKOTA). I value the conversations I've been able to have with my office mate. They have been a social breath of fresh air during the working day. I would like to thank the IT department for being so flexible with my long-term hardware and software set-up.

I would also like to thank the Global Change Education Program within the Department of Energy for providing me with support through the Graduate Research for the Environment Fellowship. I would also like to acknowledge the Atmospheric Radiation Measurement (ARM) and European Center for Medium-Range Weather Forecasts (ECMWF) program for providing data to the ARM program which was used in this research. I would

like to thank the folks at GINA for their fast, friendly service on compiling the MODIS taken images over Barrow, Alaska.

I would also like to thank my family and friends for their support, patience, and sideline encouragement. Thank you, Dr. Raluca Ilie, for your friendship, your respect, and telling me how it is. Thank you Veena Auntie, Sureesh Uncle, and Ba Patel for loving Everett and taking incredible care of him so I can go to work. Thanks goes to my parents and parents-in-law who give so much unconditional love and support in this life. Thank you, Eric, for being a super dad, super husband, and super friend.

– Erika L. Roesler

August 9, 2012

Albuquerque, New Mexico

# TABLE OF CONTENTS

# LIST OF FIGURES

**Figure**

# LIST OF TABLES

**Table**

# LIST OF APPENDICES

**Appendix**

# LIST OF ABBREVIATIONS

**2D** Two-Dimensions

**3D** Three-Dimensions

**AMPS** Arctic Mixed-Phase Stratocumulus

**AO** Arctic Oscillation

**ARM** Atmospheric Radiation Measurement

**CLUBB** Cloud Layers Unified By Binormals

**CCN** cloud condensation nuclei

**CRM** Cloud Resolving Model

**DAKOTA** Design Analysis Kit for Optimization and Terascale Applications

**DEW** Distant Early Warning

**DOE** Department of Energy

**ECMWF** European Center for Medium-Range Weather Forecasts

**FIRE-ACE** First International Satellite Cloud Climatology Project Regional Experiment - Arctic Clouds Experiment

**GCE** Goddard Cumulus Ensemble

**GCM** global climate model

**HUJI** Hebrew University in Jerusalem, Israel

**$HNO_{3(g)}$** nitric acid gas

**$H_2SO_4$** sulfuric acid

**IN** ice nuclei

**ISDAC** Indirect and Semi-Direct Aerosol Campaign

**LES** Large Eddy Simulation

**LHS** Latin-Hypercube Sample

**MILAGRO** Megacity Initiative: Local and Global Research Observations

**MM5** Mesoscale Model

**MPACE** Mixed-Phase Arctic Clouds Experiment

$N_A$ aerosol concentration

**NAO** North Atlantic Oscillation

$N_D$ droplet concentration

**NSA** North Slope of Alaska

**PDF** Probability Distribution Function

**PUTT** Parcel Undergoing Thermodynamic Transitions

**RAMS** Regional Atmospheric Modeling System

**RANS** Reynolds-averaged Navier-Stokes

**SA** sensitivity analysis

**SAM** System for Atmospheric Modeling, v6.8.2

**SBM** Spectral Bin Microphysics

**SEARCH** Study of Environmental Arctic Change

**SHEBA** Surface Heat Budget of the Arctic

**TEM** Transmission Electron Microscope

**TKE** Turbulent Kinetic Energy

**WRF** Weather Research and Forecasting model

# ABSTRACT

Representing the Fate of Springtime Arctic Clouds

by

Erika L. Roesler

Chair: Derek J. Posselt

Observations and modeling results have shown the high latitudes' environment changing in a warmer climate. The research presented focuses on the parameterizations used to simulate Arctic Mixed-Phase Stratocumulus (AMPS) clouds and the sensitivity of the AMPS to changing environmental conditions. A Large Eddy Simulation (LES) is used to reproduce an idealized AMPS during the intensive observation period, Indirect and Semi-Direct Aerosol Campaign (ISDAC). The level of complexity needed to simulate this cloud is investigated with two microphysics routines and two subgrid scale turbulent closure models. It was found that both the microphysics routines accurately produced macrophysical properties of the observed cloud, and that the less computationally expensive microphysics parameterization could be used to reproduce the AMPS. When the subgrid scale turbulent closure models were evaluated with the microphysics routines, it was found the choice of turbulent closure model had more of an effect on the cloud properties than the choice of microphysics.

Knowledge of the parameterizations needed for representing the AMPS were applied to a parameter-space-filling uncertainty quantification technique to understand the sensitivity

of the mixed-phase cloud to changes in its environment. The LES model was connected to the uncertainty quantification toolkit, Design Analysis Kit for Optimization and Terascale Applications (DAKOTA), which produced parameter ranges from which the LES model tried to produce a boundary layer mixed-phase cloud. The environmental variables that were changed were the cloud ice and aerosol concentration, surface sensible and latent heat fluxes, and large scale temperature, water vapor, and vertical motion. Four characteristic behaviors were used to classify the fates of the AMPS: stability, growth, decay, and dissipation. It was found the longevity and spatial extent of the AMPS were most sensitive to changes in large-scale temperature, water vapor, and vertical motion in the variable ranges that were investigated. It was also found the AMPS did not form unconditionally, and that environmental thresholds existed which made mixed-phase cloud formation conducive.

# CHAPTER I

# Introduction

The heating imbalance from the equator to the poles creates a temperature gradient that drives circulation in the atmosphere, bringing heat from the lower latitudes to the poles (*Trenberth et al.*, 2009). Seasonal changes at the North pole regulates how this energy is distributed in the Arctic through net surface fluxes. In the summer, the increased shortwave, or solar, radiation heats the dark ocean surface. Atmospheric heat, also known as longwave or infrared radiation, and moisture is transported from the lower latitudes. This is shown in Figure 1.1(a). In the winter, small amounts of sensible heat flux[1] from the warm ocean are released into the cold, dark atmosphere, and the transported atmospheric energy from lower latitudes radiates mostly into space (*Serreze et al.*, 2007). In the Arctic winter, a strong temperature inversion extending 1000 to 1200 m high is maintained as a radiative equilibrium from the low emissions from the extremely cold snow surface, which is nearly a black body in the infrared, and a warmer air layer above the inversion originating from poleward heat transport (*Curry and Ebert*, 1992). The occurrence of boundary layer clouds are very unlikely during the polar winter because of the inversion and low humidity. The increased sea ice coverage in the winter also prevents heat from escaping from the ocean to the atmosphere and keeps the atmosphere cooler. In the spring when the sun returns, the high albedo from the sea ice reflects much of the short wave radiation. In the summer,

[1] Sensible heat is heat exchange with the only effect being a change of temperature. That is, $Q_{sensible} = mc_p\Delta T$ where $Q_{sensible}$ is the sensible heat flux, $m$ is the body's mass, $c_p$ is its specific heat capacity, and $\Delta T$ is the change in temperature (*AMSGlossary*, 2012).

sea ice melts and radiation further warms the ocean while air temperatures remain near freezing when clouds are not present to reflect the sunlight. This is shown pictorially in Figure 1.1(b).

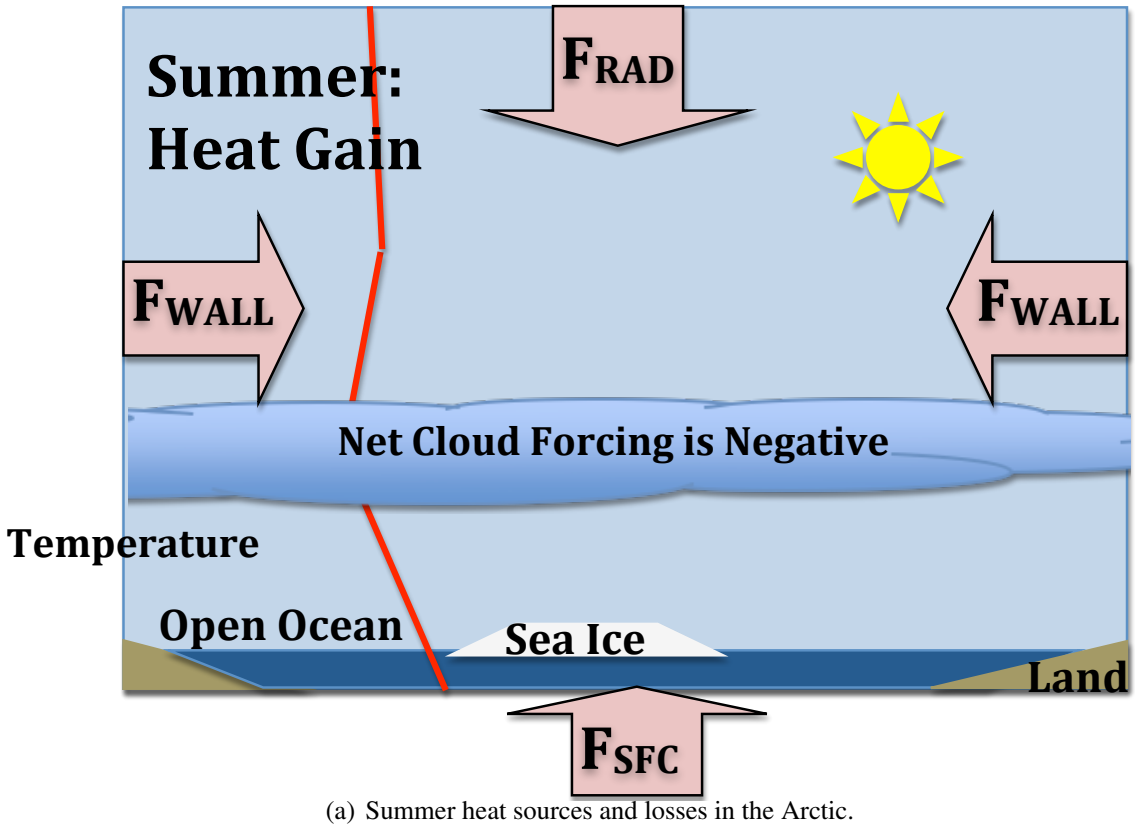


(a) Summer heat sources and losses in the Arctic.

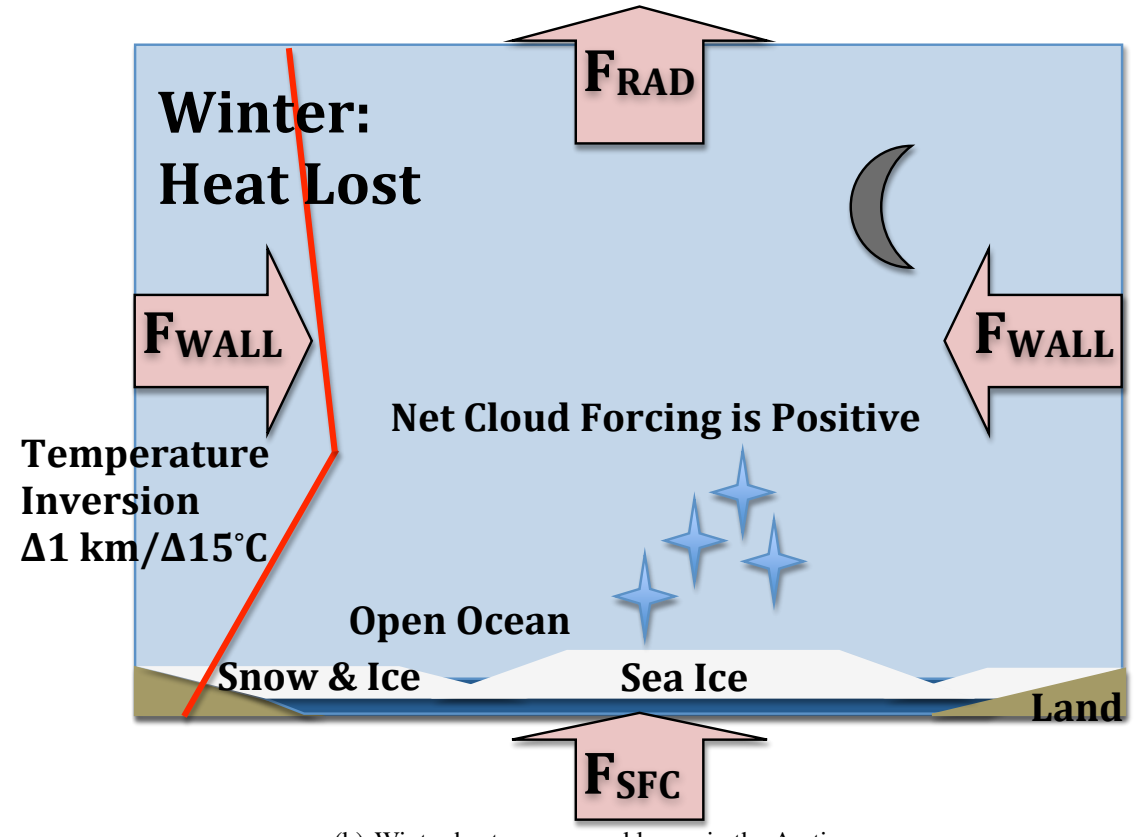


(b) Winter heat sources and losses in the Arctic.

Figure 1.1: A picture of (a) summertime and (b) wintertime heat sources and losses in the Arctic. In both (a) and (b), $F_{wall}$ is the heat, moisture, and momentum flux that is advected from the lower latitudes to the Arctic. $F_{sfc}$ is the heat, moisture, and momentum flux from the surface which can be mostly open ocean in the summer or mostly ice and snow in the winter. $F_{rad}$ is the radiative heat loss (winter) or gain (summer) out of the top of the atmosphere due to the sun (summer) or lack-of-sun (winter). The more common occurrence of boundary-layer clouds in the summer is shown by a cloud deck, and in the wintertime low-level moisture freezes into ice crystals. The vertical red line in the summer and winter pictures represents a common temperature profile. In the summer, the surface is warmer than the atmosphere above creating an unstable boundary layer. Above the cloud the temperature increases with height due to the cloud's reflection of sunlight and heat emission. The temperature begins to decrease above the cloud-top inversion. In the winter, the surface is much colder than the atmospheric layer above. This creates a stable atmospheric layer up to 1 km above the surface. The $F_{wall}$ flux from the lower latitudes warms the atmospheric layer above the inversion, and then the temperature begins to decrease with height as heat is lost to space. The net top-of-atmosphere forcing is positive only from mid-September through mid-October, is essentially zero during winter, and is negative in midsummer due to high albedo of clouds. Changes in the winter surface air temperature are closely related to changes in longwave radiation budget (*Curry and Ebert*, 1992).

Earth's climate is formed from the integrated relationship of solar radiation heating the Earth and creating the energy surplus at the equator and the energy deficit at the poles. Changes to this pattern will perturb the established climate. Observations and calculations by global models have shown the Arctic to be experiencing greater-than-average warming (*Forster et al.*, 2007; *Lemke et al.*, 2007; *Trenberth et al.*, 2007; *Walsh et al.*, 2008). The Arctic was recently found to be 1.4°C higher than projected from a two millennia trend, and high latitudes have positive feedbacks that amplify forcing more than at the low latitudes (*Kaufman et al.*, 2009). The higher increase of air temperatures in the Arctic relative to the rest of the globe is known as polar or arctic amplification. This is a process where the sea ice extent decreases in summer and warms the top of the ocean because the open ocean has low albedo and absorbs much solar energy when the sun angle is high. When the sea ice extent is large, the high albedo of the sea ice can reflect much of the solar radiation in the spring, summer, and fall. Changes in albedo are most important in Arctic summer and less in winter when there is little to no insolation. A decreasing sea ice extent then hinders ice

formation in the autumn and winter. This same process is intensified each season and acts as a positive feedback loop that has been observed in reanalysis datasets (*Serreze et al.*, 2009a,b; *Serreze and Francis*, 2006). Models show inverse correlated relationship between latitude of maximum warming and sea-ice extent (*Holland and Bitz*, 2003). Thus the Arctic region has a high vulnerability to change in a warmer climate.

Time and area changes to snow and ice will influence planetary energy balance (*Peixoto and Oort*, 1992), so changes to the Arctic sea ice cover will modify the temperature gradient from the equator to the poles and alter the circulation patterns of the atmosphere (*Francis et al.*, 2009; *Serreze et al.*, 2009b). A warmer Arctic implies the atmospheric thickness will increase and the temperature gradient between the equator and poles will decrease. Decreasing the temperature gradient can cause a weakened wind shear, which affects the development, direction, and magnitude of weather systems (*Francis et al.*, 2009; *Serreze et al.*, 2009b). In addition to the decreasing temperature gradient, shrinking sea ice could contribute to the alteration of the strength of winter weather systems (*Serreze et al.*, 2007). This is may be possible through the climatic atmospheric phenomena known as the North Atlantic Oscillation (NAO) and Arctic Oscillation (AO). The NAO is the relationship of the difference in sea surface pressure between the Icelandic Low and the Azores High. The magnitude of this difference drives the strength and direction of westerly winds into the Europe. The AO is the difference of the pressure anomalies between the Arctic and mid-latitudes. Although the relationship between sea ice and the phase of the NAO and AO remains uncertain, it has been observed that decreased sea ice extent is attributed to a wet central and southern Europe and Mediterranean with dry conditions in Northern Europe. Additionally, less rainfall may occur in the American West with increased snow depths over Siberia and northern Canada. This pattern is associated with a negative phase of the AO. In a negative phase of the NAO, temperatures would be lower than normal in Eurasia and higher than normal in North America (*Deser et al.*, 2000). In a positive phase of the AO, low sea ice levels could provide larger moisture fluxes to the atmosphere which could

blanket the lower latitudes with snow, causing widespread boreal winter cooling (*Judah et al.*).

In knowing that the Arctic sea ice extent and midlatitude weather patterns are linked, knowledge is sought in regards to what environmental mechanisms can cause further sea ice depletion. The largest driving force in sea ice extent change is the atmospheric state. Heat, moisture, and pollution are brought from the lower latitudes into the Arctic. Clouds are formed in the Arctic atmosphere from the heat, moisture, and pollutions sources. It has been found that low-level clouds, i.e., clouds with tops less than two kilometers, warm the Arctic surface. These low-level boundary layer clouds are environmental mechanisms that can contribute to the further melting of the sea ice. These clouds are the focus of this research.

## 1.1 Arctic Mixed-Phase Clouds

The reason why the Arctic boundary layer clouds warm the surface can be understood in terms of net cloud radiative forcing. The net cloud radiative forcing is the sum of the cloud short wave forcing and cloud long wave forcing. Cloud long wave forcing and short wave forcing are calculated from the difference of the amount of long or short wave radiation reaching the surface under cloudy conditions to the amount of long or short wave radiation reaching the surface under clear conditions. Arctic clouds have a net warming effect, which means more radiation is absorbed by the Arctic's surface than is reflected by the clouds' top. This is unique to Arctic boundary layer clouds because boundary layer clouds in lower latitudes have a net cooling effect, meaning they reflect more radiation at the cloud top than is released at the cloud base to heat the surface.

The low-level clouds will warm the surface and melt the sea ice throughout most of the year. At the surface, the net warming effect of the clouds throughout the year in the Arctic is due to the absence of solar radiation during the polar night and high albedo of the sea ice surface. *Curry and Ebert* (1992) developed a single-column radiative transfer

model for 80°North latitude and found that the net surface cloud forcing is positive year-long except 2 weeks in summer during maximum insolation. *Curry and Ebert* (1992) showed that a long wave, short wave competition exists in the net cloud forcing with the low sunlight amount being reflected and the persistence of the low clouds which release long wave radiation. *Intrieri et al.* (2002) measured Arctic clouds during the field campaign Surface Heat Budget of the Arctic (SHEBA) and also found that clouds warm the surface except briefly in summer. Although an increase in boundary-layer liquid clouds would warm the surface, *Curry et al.* (1996) proposed that increasing low clouds in the spring and summer could have a cooling effect because the short wave and long wave radiation budget at the surface is approximately equal. This means that small changes in the cloud and environment could cause a net positive or net negative warming at the surface.

The temperatures in which the Arctic stratocumulus clouds more frequently occur have a temperature range that is conducive to having both liquid and ice species in the cloud. When the Arctic low-level clouds contain both ice and liquid, they are called mixed-phase clouds. The low-level, boundary-layer mixed-phase clouds have a large spatial and temporal extent, just as the boundary layer stratocumulus clouds have at lower latitudes. They can be hundreds of kilometers in spatial extent and exist for days. Mixed-phase clouds have different microphysical structure and radiative properties than liquid-only clouds. Mixed-phase clouds are more transmissive than clouds in mid-latitudes because they are thinner, have lower water content, less turbulent energy, and have lower amounts of water vapor per unit mass of moist air, i.e., specific humidity.

With the mixed-phase stratocumulus clouds' warming effect on the sea ice, the changing sea ice's effect on weather patterns, and the uncertainty of knowing the extent of the Arctic warming, more information is needed about Arctic processes and the environment to make forecasts for the future. Field campaigns have collected more information about the Arctic clouds and surface, but decades of observations are needed to see qualitative trends. Large global models can be used to make forecasts, but they have difficultly replicating

the observed structure of the clouds, and thus cannot determine what the boundary layer cloud's role is with contributing to sea ice loss.

## 1.2 Dissertation Motivation

A number of fundamental outstanding questions remain regarding the behavior and characteristics of the Arctic Mixed-Phase Stratocumulus (AMPS). The model complexity and resolution required to realistically simulate the clouds are not precisely known. The interactions between aspects of the boundary layer and cloud microphysical schemes are potentially important and not well known. Nonlinearity in cloud processes makes it difficult to understand the functional relationship between changes to the Arctic environment and changes to the physical and radiative properties of AMPSs.

This research seeks reduce the uncertainty in knowing the level of model complexity needed to simulate single-layer AMPS. Two microphysics and two turbulence packages are compared to assess the necessary level of model complexity. These analyses and results are presented in Chapters III and IV. Upon establishing the level of model complexity, the initial environmental conditions in which the AMPS has been formed is perturbed to understand its sensitivity to changes in its surroundings. The simulated cloud environment is perturbed by using a parameter estimation in a separate software package called Design Analysis Kit for Optimization and Terascale Applications (DAKOTA). Uncertainty quantification algorithms have never before been applied to a study of AMPS clouds and represent the application of a set of powerful analytic tools to a new set of challenging and important problem. This procedure and the subsequent results are described in Chapter VI.

# CHAPTER II

# Experiment Set-Up

## 2.1 Observations of the Arctic Environment

### 2.1.1 Relationship between Sea Ice and Clouds

Arctic boundary-layer clouds are the focus of this research because of their potential to warm the surface and contribute to melting sea ice. The formation of low clouds in the Arctic spring has been attributed to the general circulation when moist continental air masses are pushed over icy surfaces and cooled (*Herman and Goody*, 1976). With the minimum sea ice extent in the Arctic decreasing, the relationship between sea ice and boundary layer clouds is questioned. Open water provides a moisture and heat source for low cloud formation. A correlation between open water and increased clouds has been observed (*Huschke*, 1969), but a 16% decrease in summer cloudiness from 2006 to 2007 coincided with the 2007 Arctic sea ice minimum (*Kay et al.*, 2008; *Xiquan et al.*, 2009). With increasing low cloud cover, the long wave radiation increases to the surface. *Francis and Hunter* (2006) found that the sea ice extent in the past decade is influenced by the surface energy balance instead of wind anomalies. The increasing surface energy in the spring and summer is from the increased downward longwave flux due to increasing clouds and water vapor from exposed ocean and insolation. In the autumn, *Schweiger et al.* (2008) also found cloud cover and sea ice are linked. Unlike in the spring, a decrease in low-level

cloud and increase in midlevel cloud was found to coincide with decreasing sea ice. This is believed to be caused by a decrease in static stability and deepening of the atmospheric boundary layer that breaks the surface and cloud-top inversion normally present in the spring.

### 2.1.2 Seasonal Properties of Arctic Clouds

Many decades of observations have shown evidence that Arctic boundary layer clouds have an annual cycle. Observations of the prevalence and types of clouds began when the circumpolar land masses surrounding the Arctic Ocean were dotted with Distant Early Warning (DEW) stations during the cold war (*Dyson*, 1979; *Wohlforth*, 2004). *Huschke* (1969) produced one of the first records of cloud height and occurrence from surface-based and aircraft observations for weather applications at that time. *Huschke* (1969) found a very abrupt spring transition in low cloud amount in all regions of the Arctic. The low-level clouds in the Arctic more frequently occur in the spring, summer, and fall. It was also observed that the occurrence of midlevel clouds was almost constant year around. The maximum occurrence of middle and high clouds was in October, most likely because there is a high degree of cyclonic activity in the Arctic in October. The number of high-level clouds were lowest in the summer.

Surface-based remote sensors were used for year-long measurements during the Surface Heat Budget of the Arctic (SHEBA) campaign of 1997 - 1998 (*Shupe et al.*, 2005a). It was reported that multi-layered cloud scenes containing multiple cloud types were common, and that mixed-phase clouds (clouds containing both liquid and ice) had higher occurrences during the transition seasons of spring and autumn. The high occurrence of mixed-phase clouds during these seasons was attributed to the atmospheric temperatures at that time. During SHEBA, all-liquid clouds were observed to occur during about 20% of the year, and mixed-phase were observed to occur about 40% of year. No seasonal trend was observed with all-ice clouds (*Shupe et al.*, 2005a).

Some Arctic field campaigns undergone in the last decade have focused on obtaining microphysical data from mixed-phase clouds. During Mixed-Phase Arctic Clouds Experiment (MPACE) (*McFarquhar et al.*, 2007) and Study of Environmental Arctic Change (SEARCH) (*de Boer et al.*, 2009), single-layer stratiform mixed-phase clouds were found to occur under different wind conditions between 4% and 26% of the time. Bulk cloud properties were similar to those observed by *Huschke* (1969) where the mean cloud base was between $\sim 700 - 2100$ m, the mean thickness between $\sim 200 - 700$ m, and the mean in-cloud temperatures were between $\sim 242 - 271°$K. The clouds' liquid-to-ice ratio decreased as cloud temperature decreased.

### 2.1.3 Indirect and Semi-Direct Aerosol Campaign

A recent field campaign, Indirect and Semi-Direct Aerosol Campaign (ISDAC), sought to make simultaneous measurements of clouds and aerosols during a time of the year before the sea ice began to significantly melt but boundary layer clouds were likely. Measurements of mixed-phase clouds and aerosols were made during the Department of Energy (DOE) Atmospheric Radiation Measurement (ARM) program's ISDAC conducted in April 2008. Aerosols measurements were a focus of this field campaign because changes in aerosol concentrations and composition can alter cloud cover (*Forster et al.*, 2007). The direct aerosol effect, the semi-direct effect, the cloud albedo effect, and the cloud lifetime effect have been identified as unique processes by which aerosols can affect clouds globally. The direct aerosol effect is the aerosols' ability to directly absorb and reflect radiation. The semi-direct effect is the aerosols' ability to heat and evaporate the cloud they surround. The cloud albedo effect is the ability of aerosols to become cloud droplets which decreases cloud effective radius and increases cloud-top reflectivity. The cloud lifetime effect is the ability of aerosols to act as cloud particles and increase the cloud lifetime by enhancing cloud-top stability and weakening entrainment of dry air into the cloud (*Forster et al.*, 2007; *Koch and Del Genio*, 2010).

High aerosol concentrations in the Arctic have been observed. In the spring a recurring pollution event called the Arctic Haze brings elevated concentrations of nitrates, sulfates, and carbonaceous material to the region (*Barrie*, 1986; *Przybylak*, 2003; *Quinn et al.*, 2007). The industrialized areas in the lower latitudes are the source of the Arctic Haze, and the transport from the mid-latitudes to the Arctic takes between $5 - 10$ days. This event has been observed in the spring for over 50 years. As pollution sources change, the haze concentrations and compositions have also changed. The Arctic Haze properties have been observed to be tens of meters to one kilometer thick and $\sim 20 - 200$ kilometers wide. The Arctic Haze also heats the atmosphere and cools the surface during the day, but infrared emissions would heat the surface at night. Figure 2.1 shows this phenomenon pictorially. In the spring, the haze begins to descend and vertically mix below 3 kilometers. The haze particles become aged, scavenged, and mixed as they reach the Arctic (*Quinn et al.*, 2007). Appendix C explores two ways to model how a freshly emitted soot particle ages. It was predicted in the soot particle model and observed in laboratory measurements that the soot particles will be aged before reaching the Arctic.

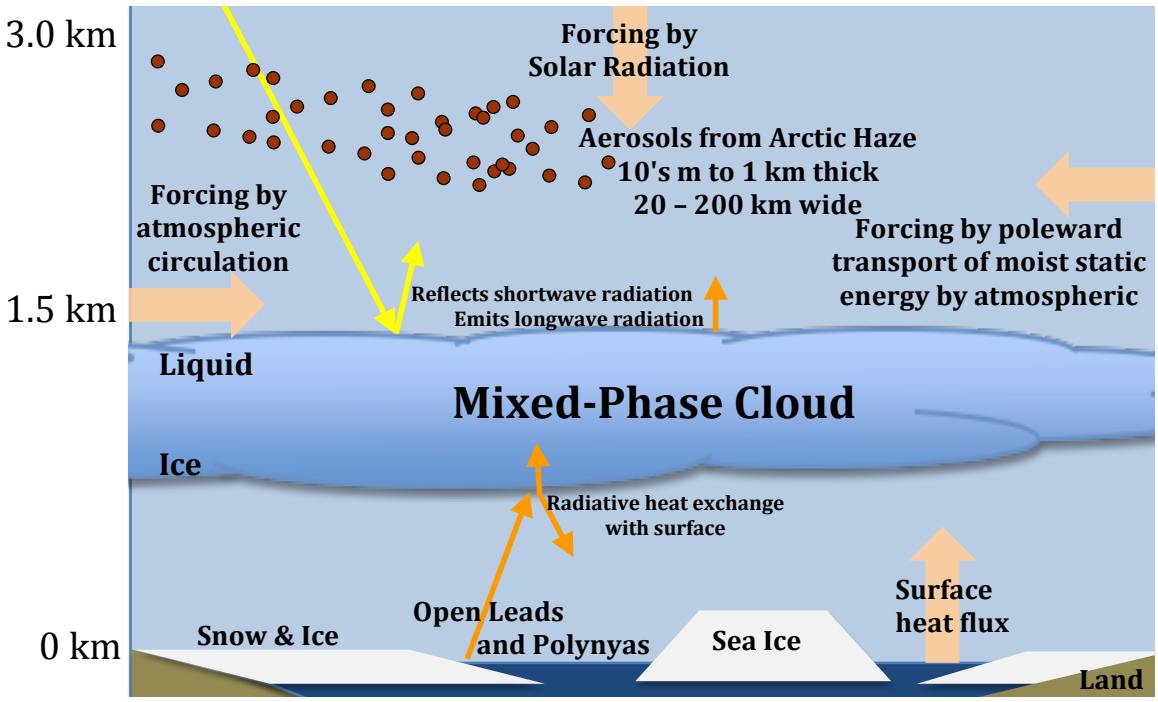


Figure 2.1: Arctic Haze Layer occurs in lowest 5 kilometers and peaks at about 2 kilometers. It can be tens of meters to 1 kilometer thick and $20 - 200$ kilometer wide.

The ISDAC mission was based out of the permanent ARM field site located near Barrow, Alaska on the North Slope of Alaska (NSA). Measurements were made of the composition and abundance of anthropogenic haze particles during ISDAC. Mixed-phase clouds have been previously observed at this location during other similar campaigns such as SHEBA, MPACE, and First International Satellite Cloud Climatology Project Regional Experiment - Arctic Clouds Experiment (FIRE-ACE) (*Barrie*, 1986; *Ghan et al.*, 2007; *Shupe et al.*, 2005b, 2006). ISDAC research teams utilized aircraft and ground-based instruments for measurements of aerosols, hydrometeors, temperature, wind speeds, pressure, and water content of clouds. During ISDAC, the observed atmospheric conditions included days of multiple cloud layers in a stratified atmosphere, days of Arctic Haze, days of clear sky, and days of single-layer clouds. Single structure, one layer clouds were observed on April 8 and April 26. These days are called "golden days" because they are useful in numerical simulations to understand the microphysical structure and longevity of mixed-phase clouds. They occurred without any interaction with multiple cloud layers or high aerosol

concentrations (*McFarquhar et al.*, 2011). This research will focus on the springtime Arctic cloud cover during the April 26, 2008 "golden day". A "golden day" was selected for study because we wish to understand the needed complexity in simulating a Arctic Mixed-Phase Stratocumulus (AMPS) without additional aerosols or cloud layers. Understanding the impact of a single AMPS on the warming of the sea ice is the goal of this research.

On April 26, 2008 near Barrow, Alaska, the meteorological conditions were such that a high pressure system was set over the Arctic Ocean which produced this single-layered mixed-phase cloud system. There was a weak easterly wind flow off the ocean (*McFarquhar et al.*, 2011). Figure 2.2 shows visible satellite images taken over the state of Alaska during 26 April 2008. (Credit to University of Alaska - GINA www.gina.alaska.edu for aligning, labeling, and publishing the images online). The year, month, day, and local time is printed on the bottom of each of the photos. The view of Alaska on 26 April 2008 shows there is much cloud cover. Beneath the clouds is sea ice and snow on the land. The populated town and cites are labeled. The grey shaded region of the image is outside the field-of-view of the camera. In this picture, it is not possible to distinguish between the surface ice and the clouds. A different instrument aboard the satellite would be used to measure differences in emitted wavelengths.

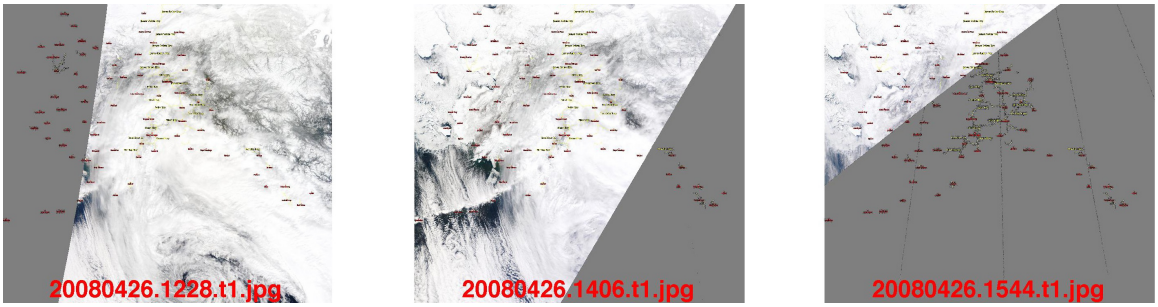


Figure 2.2: Visible satellite images from MODIS taken over the state of Alaska during April 2008. Credit to University of Alaska - GINA www.gina.alaska.edu for aligning, labeling, and publishing the images online.

The satellite images in Figure 2.2 provide a qualitative picture of the Arctic conditions on April 26, 2008. Data regarding the atmospheric properties of the cloud was obtained

from aircraft with 100 km path within the cloud and four hours of flying. Figure 2.3 shows the flight leg that sampled the AMPS. During this time, it was found the average cloud top height was at about 850 m, and the average cloud base was at about 650 m. The cloud-top temperature was also between -13°and -15°C, and the cloud-top temperature inversion was between 1°and 3°C over a few tens of meters. The liquid and ice water content of the cloud varied between 0.1 - 0.15 g $m^{-3}$ and $\sim$ 0.01 - 0.04 g $m^{-3}$, respectively. The number of cloud droplets varied between $\sim$ 150 - 200 $cm^{-3}$, and the number of ice crystals with diameters greater than 200 $\mu$m varied between $\sim$ 0.3 - 0.7 $L^{-1}$.

For comparison, measurements of the cloud on April 8, 2008 were taken by aircraft over a 180 km path and three hours of flying. It was found the cloud top varied between 700 - 1100 m, and the cloud base varied between 550 - 1000 m. The cloud-top temperature was between -13°and -15°C, and the cloud-top temperature inversion was between 3°and 4°C. The liquid and ice water content of the cloud varied between 0.05 - 0.4 g $m^{-3}$ and $\sim$ 0.02 - 0.05 g $m^{-3}$, respectively. The number of cloud droplets varied between $\sim$ 100 - 200 $cm^{-3}$, and the number of ice crystals with diameters greater than 200 $\mu$m varied between $\sim$ 0.5 - 1 $L^{-1}$.

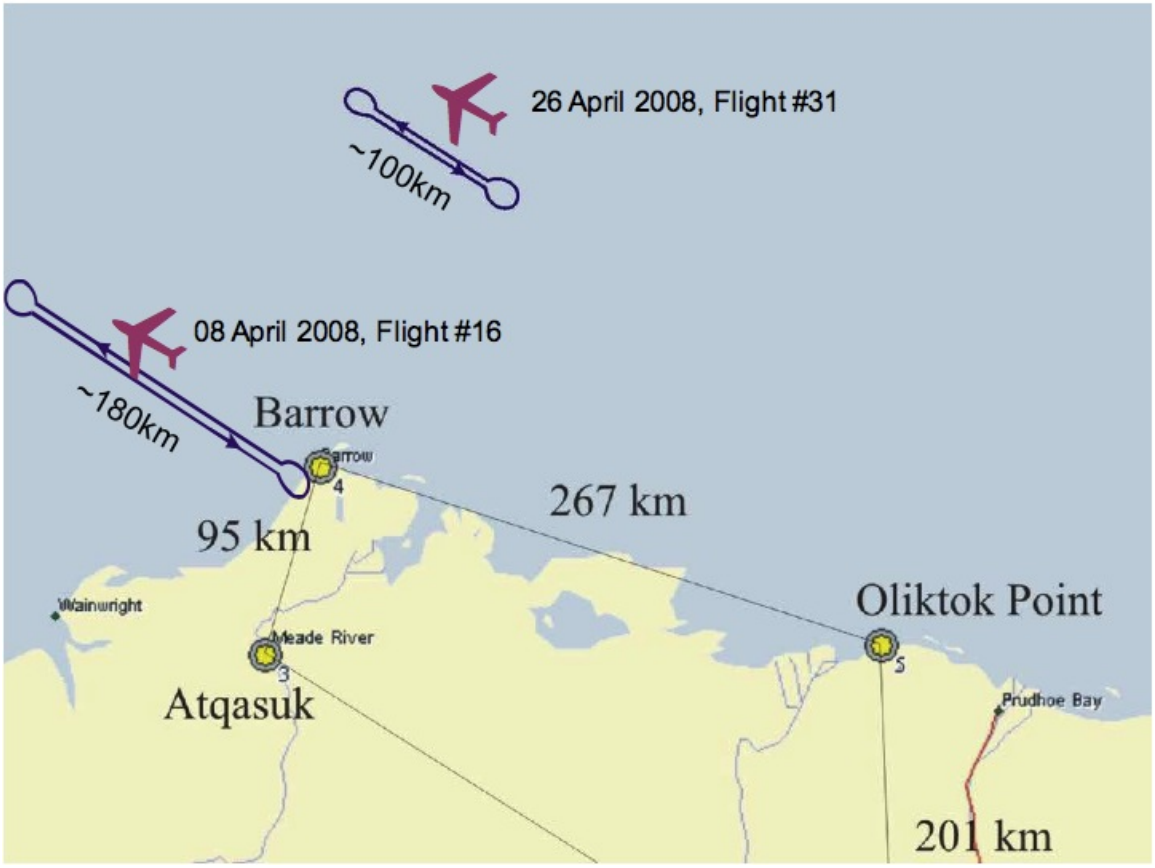


Figure 2.3: Flight paths through single-layer mixed-phase stratocumulus clouds observed on the golden days during ISDAC.

## 2.2 Model Background

To understand how the mixed-phase cloud warms the ice surface, a Cloud Resolving Model (CRM)-type model was chosen for this study over a regional model or global model because of its ability to resolve cloud hydrometer processes and the ability to capture the cloud particle's response to changes in a cloudy environment. The grid spacings in a CRM are usually on the order of tens to hundreds of meters. The AMPS clouds have been observed to contain both liquid and ice for days at a time in clouds that are several hundred kilometers in size. The global climate models (GCMs), which could predict a saturated grid box as part of this mixed-phase stratocumulus cloud, the entire cloud system, and it's encompassing environment, does not have the ability to simulate the liquid and ice together

in the same cloud over the period of time that the AMPS occur. This is because a parameterization in a GCM predicts ice formation in a cloud as a function of temperature. At the sub-freezing temperatures in which AMPS occur, the cloud liquid water content will be converted to ice because the ice supersaturation is less than that for liquid. The ice particles will continue to grow at the expense of the liquid particles, and the cloud would quickly glaciate. A regional or nested model can have the same parameterizations as a GCM, depending on its grid size and time step. A regional model could be used to replicate the observed cloud on a specific day and its larger dynamic system, but the purpose of this research is to resolve the mixed-phase cloud liquid, ice, and energy budgets as specifically as possible. To do this, the CRM called System for Atmospheric Modeling, v6.8.2 (SAM) was chosen.

CRMs have been used to investigate many types of clouds in the Earth system. These types of models are useful for deep convection, marine stratocumulus, continental stratus, orographic clouds, squall lines, aerosol effects on clouds, and recently as a tool for diagnosing some cloud properties in a GCM grid box. The benefit of using a CRM would be to resolve boundary layer processes, to investigate cloud mass and energy budgets in large turbulent eddies, and understand precipitation processes such as the types and amounts of precipitation. The disadvantages of using CRMs are related to the computational cost and time required to simulate those processes explicitly over a large area for a significant amount of time. However, the ability to resolve cloud features, convective processes, and to integrate models for a longer duration has been made possible by the advancements in computing resources and availability. The CRM is set-up in a way to be used for a single type of cloud over one location in time. The CRM, SAM, is based on the theory of Large Eddy Simulation (LES), which is further described in Chapter IV.

To highlight how simulated AMPS cloud properties can change under changing numerical parameterizations or small changes in the environmental conditions, only a portion of the cloud is simulated. The sensitivity of this portion of the cloud to changes in its physical

representation or the environment serves as a proxy to the cloud as a whole. This can be assumed from the spatially homogeneous quality of the AMPS observed on 26 April 2008, and by applying periodic boundary conditions to the CRM. Thus changes made within the simulation domain are effectively made to the cloud as a whole. The initial conditions are also idealized by smoothing small fluctuations in the atmospheric profiles. This was done to emphasize the magnitudes of the temperature, water vapor, and wind as functions of altitude that are generally common to stratocumulus.

## 2.3 Experiment Design

### 2.3.1 Model Description

Simulations are performed with SAM, a LES. *Khairoutdinov and Randall* (2003) contains a thorough description of SAM, and some features of SAM will be highlighted here. The advection and diffusion of momentum are second-order accurate, with kinetic energy conservation under advection.

The time integration of the momentum equations was performed with a third-order Adams-Bashforth scheme. As described in *Durran* (1991), for a dependent variable, $\psi$, the ordinary differential equation in time, $d\psi/dt = F(\psi)$, can be approximated by the $N$th-order finite difference equation,

$$\frac{\phi^{n+1} - \phi^n}{\Delta t} = \sum_{j=0}^{N-1} a_j F(\phi^{n-j}), \tag{2.1}$$

where $\phi^n$ is a numerical approximation to $\psi(n\Delta t)$. The coefficients, $a_j$, can either be determined from the Taylor series expansions for $\psi$ and $F(\psi)$, or by writing the equivalent integral equation

$$\psi((n+1)\Delta t)) = \psi(n\Delta t) + \int_{n\Delta t}^{(n+1)\Delta t} F(\psi(t))dt, \tag{2.2}$$

by which the Adams-Bashforth scheme approximates as

$$\int_{n\Delta t}^{(n+1)\Delta t} F(\psi(t))dt = \Delta t \sum_{j=0}^{N-1} a_j F(\phi^{n-j}). \tag{2.3}$$

Following the steps to compute the coefficients described in *Durran* (1991), the third-order Adams-Bashforth scheme is given by

$$\phi^{n+1} - \phi^n = \frac{\Delta t}{12}\left(23F(\phi^n) - 16F(\phi^{n-1}) + 5F(\phi^{n-2})\right). \tag{2.4}$$

The benefits of using the third-order Adams-Bashforth scheme is that it is explicit, not subject to time splitting instability, is more accurate than a leapfrog scheme, and is not much more computationally expensive compared to similar-ordered schemes (*Durran*, 1991).

### 2.3.2 Experiment Set-up

The center of the domain is 71.32°North, -156.61°West. SAM simulated the Arctic Mixed-Phase cloud for 24 hours in a Three-Dimensions (3D) domain of 96×96×96 grid points. A uniform vertical grid was used with grid spacings of $\Delta$z = 40 m starting from 20 m above the surface. The horizontal grid spacings were $\Delta$x = $\Delta$y = 100 m. The time step was 2 seconds. The grid spacing and time step were chosen so that the evolution of the areas of liquid and ice within the cloud could be properly resolved. The time step and grid spacing satisfied numerical stability conditions as well. The domain size is similar to

other AMPS modeling studies such as *Ovchinnikov et al.* (2011) and *Fan et al.* (2009a). This domain size was tested by increasing the number of points and the grid spacing, and it was found the simulated AMPS cloud structure did not change in a significant way.

The aerosol size distribution mean diameter, $D$, geometric standard deviation, $\sigma$, and number concentration, $N$, were prescribed in SAM with the values for the April 26, 2008 from Table 2.1. The other AMPS golden day during ISDAC was April 8, 2008, and the aerosol size distribution parameters are similar between the two golden days. The aerosol parameters are based on measurements and compiled by Peter Liu and Mike Earle. The primary aerosol composition was sulfate mixed with organics, biomass burning, and sea salt on these golden day (*McFarquhar et al.*, 2011). It was found that most of the larger particles over $0.1\mu$m were activated in the cloud, and that particle size was the most important parameter for aerosol activation with sulfate content being of secondary importance (*Zelenyuk et al.*, 2010). The aerosol composition was approximated by using ammonium sulfate, $(NH_4)_2SO_4$, with no insoluble, organic, or sea salt components. This composition was also used so that this study will be comparable to other cloud-aerosol studies from ISDAC. A comprehensive study of how aerosol variables including concentration, composition, and size affect cloud droplet number was performed by *Roesler and Penner* (2010) and is shown in Appendix D. Based on the aerosol measurements taken during the golden days and the conclusions in *Roesler and Penner* (2010), approximating the aerosol composition as the three-ion ammonium sulfate instead of more complicated molecule is not expected to change the droplet number within the modeled cloud significantly.

Table 2.1: Average aerosol size distributions measured during ISDAC golden days.

| Date | ISDAC flights | D ($\mu$) | $\sigma$ | N ($cm^{-3}$) |
|---|---|---|---|---|
| 08 April 2008 | 16 | 0.188 | 1.40 | 165 |
| 26 April 2008 | 30, 31 | 0.194 | 1.48 | 199 |

SAM was initialized with similar conditions observed from the DOE ARM site's radar and atmospheric sounding measurements and from the aircraft flight taken on 26 April

2008. The atmospheric profiles were derived using constrained variational analysis based on European Center for Medium-Range Weather Forecasts (ECMWF) analysis as developed by *Zhang and Lin* (1997); *Zhang et al.* (2001) and implemented, for example, by *Xie et al.* (2006). This technique uses sounding measurements of winds, temperature, and water vapor mixing ratio to interpolate GCM grid-scale vertical velocity and advective tendencies. As the domain of the simulated AMPS in SAM is the size of one high-resolution GCM grid box, the atmospheric profiles derived from this procedure are used in this experiment. Figure 2.4 shows the derived atmospheric profiles from the ECMWF analysis for a a day-and-a-half before and after the simulated time of day 117.5 0:00:00 UTC to day 118.5 0:00:00 UTC. The atmospheric profiles have values for pressure heights up to 25 mbar, which is exceeds the boundary layer and lower-atmosphere height in the Arctic. Figure 2.5 shows just the lower portion of the atmospheric profiles from 1000 mbar to 775 mbar. For reference, Figure 2.6 shows the height in meters of the pressure levels as interpolated by SAM assuming a standard reference atmosphere.

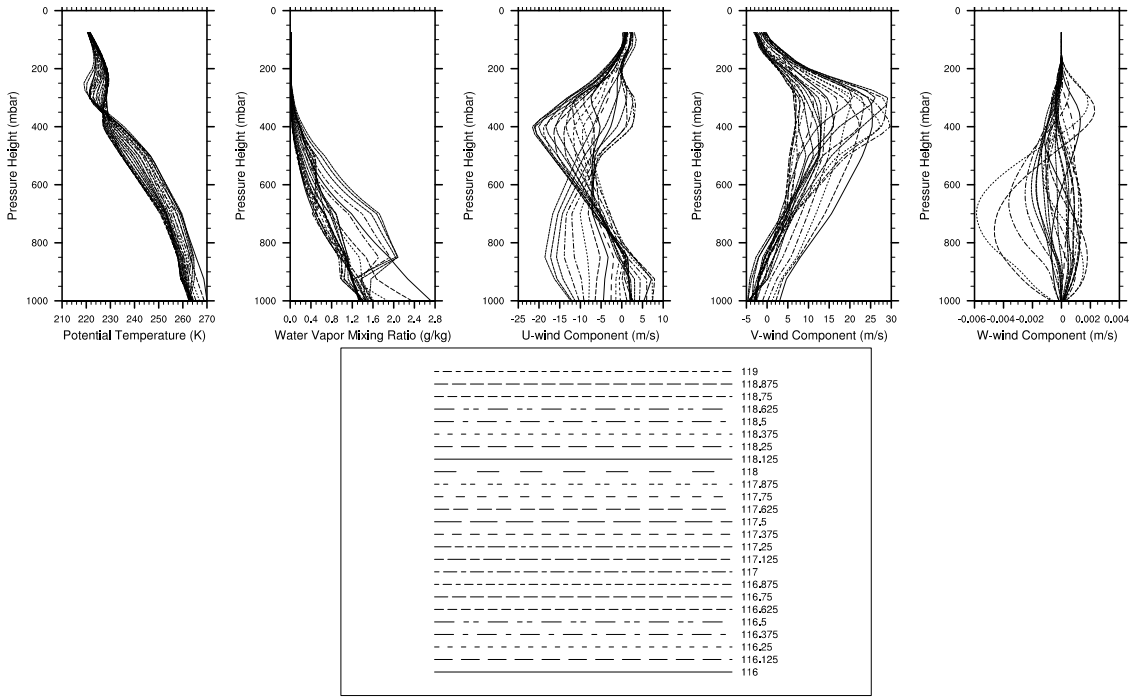


Figure 2.4: Vertical atmospheric profiles from ARM's database for ISDAC. The profiles were derived from ECMWF analysis using constrained variational analysis. Shown are profiles every eighth-of-a-day from day 116 0:00:00 to day 119 0:00:00 UTC of 2008. From left to right, potential temperature ($\theta_p$), water vapor mixing ratio ($q_v$), meridional (u), longitudinal (v), and large-scale vertical ($w_{ls}$) wind speeds.

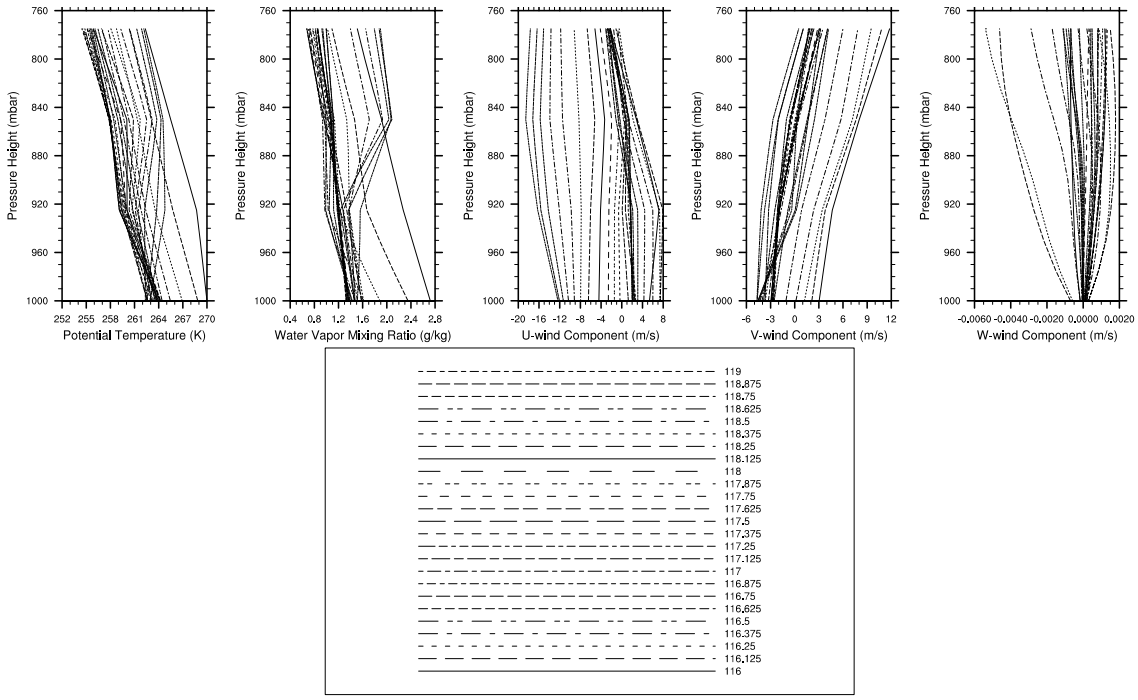


Figure 2.5: Vertical atmospheric profiles pressure-height 1000 mbar to 775 mbar from ARM's database for ISDAC. The profiles were derived from ECMWF analysis using constrained variational analysis. As in Figure 2.4, the profiles are every eighth-of-a-day from day 116 0:00:00 to day 119 0:00:00 UTC of 2008. From left to right, potential temperature ($\theta_p$), water vapor mixing ratio ($q_v$), meridional (u), longitudinal (v), and large-scale vertical ($w_{ls}$) wind speeds.

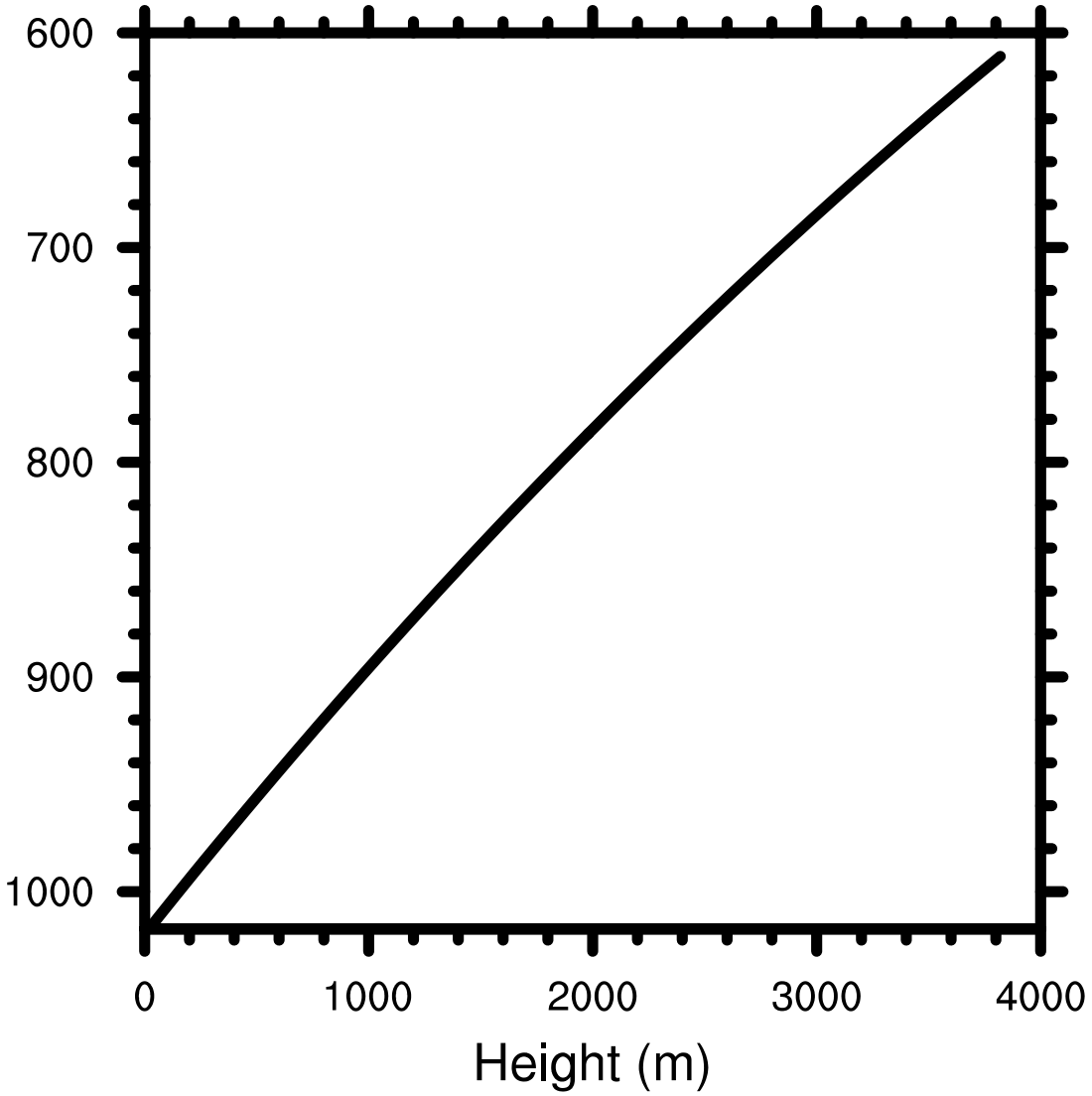


Figure 2.6: The geometric height in meters of the pressure-heights as calculated by SAM using a standard reference atmosphere.

The profiles used for this research are based on the properties shown in Figure 2.4 and are shown in Figure 2.7. The profiles are idealized compared to the profiles shown in 2.4. The temperature and moisture profiles in the lower troposphere were modified to more closely match the structure of the boundary layer at the time and location of the flight that was making in situ measurements in the cloud (*M. Ovchinnikov, personal communication*). Figure 2.7 shows a well-mixed boundary layer in potential temperature and water vapor from the surface to about 900 millibars, or about 950 m. At 900 millibars (950

m), the potential temperature begins to increase with height. When the cloud is initially formed in SAM, the increasing potential temperature with height creates a vertically stable atmospheric and will prevent the cloud top from increasing in height. Figure 2.5 shows a presence of a subsidence during the time of day 118.125 - 119 as calculated from the ECMWF analysis. During the time period of day 116.5 - 116.875 the vertical motion was negative for pressure-heights greater than 950 mbar and positive or near-zero for heights lower than 950 mbar. A large-scale subsidence was used in the simulation to reflect the subsidence produced by the ECMWF analysis.

As seen in Equation 2.4, the third-order Adams-Bashforth scheme requires two time steps, $(n-1)$ and $(n-2)$, prior to the current time step, $n$, to predict the variable value at a future time, $(n+1)$. Thus SAM requires two points in time in the profiles in order to initialize the model run. Figure 2.7 shows the idealized initial soundings that were used to initialize the cloud at day 117.5 0:00:00 UTC, abbreviated 117.5 UTC hereafter. The second point in time was 24 hours later at day 118.5 0:00:00 UTC, abbreviated 118.5 UTC hereafter. The profile values for $u$, $v$, $\theta_p$, and $q_v$ were set to be equal at 117.5 UTC and 118.5 UTC. SAM uses linear interpolation from these equivalent points in time to fill-in flow field information at the $(n-2)$, $(n-1)$, and $n$ time steps to predict the flow one time step (2 seconds) later at $(n+1)$.

The time tendencies of the zonal and meridional wind, $\frac{d}{dt}(u(x,y,z,t))$ and $\frac{d}{dt}(v(x,y,z,t))$, were nudged every $\tau_{ls}$ = 7200 seconds to the profiles of the $u$ and $v$ large-scale wind components, $u_0(z)$ and $v_0(z)$. Equations 2.5and 2.6 shows the method within SAM, for the $u$ and $v$ tendencies,

$$\frac{d}{dt}(u(x,y,z,t)) = \frac{u_0(z)}{\tau_{ls}} \tag{2.5}$$

$$\frac{d}{dt}(v(x,y,z,t)) = \frac{v_0(z)}{\tau_{ls}}. \tag{2.6}$$

The atmospheric winds within SAM's domain pushed cloud material out of the simulation domain at one end, but due to the periodic boundary conditions, that mass re-entered on the opposite side of the domain. The potential temperature and water vapor mixing ratio were not forced within the simulation time period. Because the initial sounding conditions of the model and the large-scale wind forcing were the equivalent throughout the simulation time period, a laminar advective flow was developed under the periodic boundary conditions with the ability to develop a steady-state flow over time.

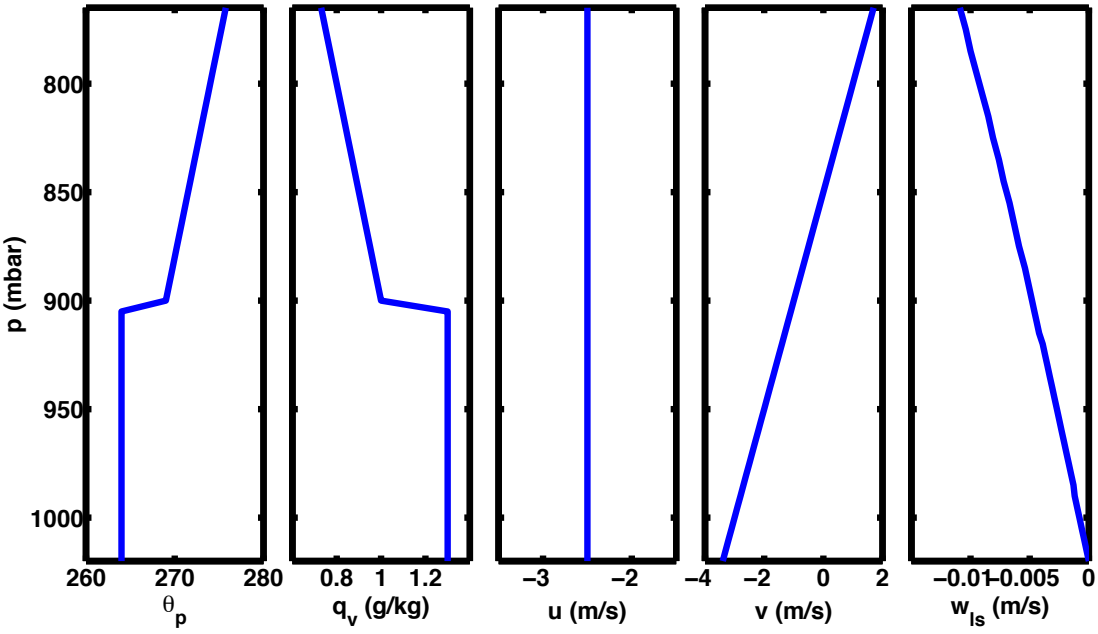


Figure 2.7: Idealized vertical profiles used for model initialization and large-scale forcing. From left to right, potential temperature ($\theta_p$), water vapor mixing ratio ($q_v$), meridional (u), longitudinal (v), and large-scale vertical ($w_{ls}$) wind speeds. The $\theta_p$, $q_v$, $u$, and $v$ were used for the sounding initial conditions. The $u$, $v$, and $w$ were used for the forcing.

# CHAPTER III

# Comparison of Microphysics Parameterizations

## 3.1 Introduction

Microphysical schemes are the portion of a Cloud Resolving Model (CRM) that solves for the cloud hydrometeors. In the environment, the interactions between the cloud particles happen on the micro- to centimeter scales. However, the grid spacings in a CRM are usually on the order of tens to hundred of meters. Consequentially, the condensation, evaporation, collision, freezing, and other processes are approximated within the CRM. Microphysical schemes began as single-moment bulk schemes where the mass of a cloud hydrometer species would be prognosed throughout the simulation. Currently, a majority of CRMs use a double-moment bulk microphysical scheme. The mass and number of selected cloud hydrometer species is predicted where the size of the particles would be prescribed.

Knowledge of the size distribution of the cloud hydrometers becomes necessary as questions regarding aerosol-cloud interactions are presented. Bin models, compute the evolution of the size distribution of the cloud particles in time. These models are capable of directly simulating the aerosol impact on clouds. Bin models often have higher fidelity than bulk models when compared to observations (*Lynn et al.*, 2005a,b; *Lynn and Khain*, 2007; *Li et al.*, 2009a,b; *Khain et al.*, 2009). However, the bin models have a significantly higher computational expense than the bulk models.[1]

[1]It took a month of continuous super-compute time to obtain Spectral Bin Microphysics in Three-

Bin and bulk model comparisons have been performed for a variety of model configurations and cloud types (see references in Table 3.1). Ideally, the bulk scheme should produce very similar results with the bin scheme with little or no modifications to the specific cloud system being studied. Because of the significantly higher computational expense of bin models, they are often not possible to use in many 3D models, and not in global climate models (GCMs). The motivation for this study is to identify differences in the bin and bulk scheme and to replicate Spectral Bin Microphysics (SBM) results using a bulk scheme inside the CRM, System for Atmospheric Modeling, v6.8.2 (SAM), in an "out of the box" way without making case-specific modifications to either scheme when simulating Arctic Mixed-Phase Stratocumulus (AMPS). We also wish to evaluate the ability of these two microphysical parameterizations to simulate a single-layer AMPS. Versions of these bulk and bin schemes are used in popular models such as Weather Research and Forecasting model (WRF), Regional Atmospheric Modeling System (RAMS), Goddard Cumulus Ensemble (GCE), and Mesoscale Model (MM5).

The first microphysics package is the two-moment Morrison microphysics (see *Morrison et al.* (2005)) that predicts mass and concentration of drops, ice, rain, snow, and graupel.[2,3] All hydrometeor sizes can be represented by gamma functions. *Morrison et al.* (2005) derived an analytic approximation of the supersaturation equation that is used to calculate supersaturation and droplet activation.

The second microphysics package is the Hebrew University in Jerusalem, Israel (HUJI)-SBM (see *Fan et al.* (2007); *Khain and Pokrovsky* (2004) for thorough descriptions of the SBM). Thirty-three mass-doubling bins predict mass, concentration and size distribution of rain, snow, graupel, hail, columns, plates, dendrites, cloud condensation nuclei (CCN), and ice nuclei (IN). Droplet nucleation, primary and secondary ice generation, conden-

Dimensions (3D). The bulk scheme took a few days with the same configuration.

[2]Graupel are "heavily rimed snow particles, often called snow pellets; often indistinguishable from very small soft hail except for the size convention that hail must have a diameter greater than 5 mm. Sometimes [they are] distinguished by shape into conical, hexagonal, and lump (irregular) graupel." (*AMSGlossary*, 2012)

[3]rime – (frost) an accumulation of granular ice tufts formed from supercooled fog or cloud (*Inc.*, 2005)

sation/evaporation of drops, deposition/sublimation of ice particles, freezing/melting, and mutual collisions between various hydrometeors is also predicted. Recent improvements in the SBM microphysics include CCN recycling, where evaporated droplets are redistributed back to the initial CCN size distribution (*Fan et al.*, 2009a), and a parameterization that maintains a constant prescribed in-cloud ice particle number mixing ratio (see *Ovchinnikov et al.* (2011)).

The HUJI-SBM (SBM hereafter) microphysics parameterization has been used to simulate many types of clouds in a variety of model configurations. Table 3.1 shows a selection of studies that have used the SBM in atmospheric simulations. The primary purpose of this table is to show that the SBM has been used in warm cloud, deep and shallow convective cases, and over a magnitude's span of grid spacings.

## 3.2 Results and Discussion

### 3.2.1 Overall Results of Bin and Bulk Microphysics

Figure 3.1 shows the domain-averaged evolution of the mixed phase cloud profile during the 24-hour simulated period. Both the bulk and the SBM clouds contain liquid and ice, and both microphysics routines produced clouds that contained liquid water at the top with a transition to ice in and below the liquid layer. Both mixed phase clouds are precipitating ice. The bulk microphysics predicts a larger liquid mass and number concentration than the SBM. The SBM predates a larger ice mass and number concentration compared to the bulk.

A nearly constant cloud top height was produced in both the SBM and the bulk simulations. The cloud top boundary is defined to be where the total water mixing ratio, $q_T$, the sum of all liquid and ice hydrometers, is greater than or equal to $10^{-5}$ kg/kg. The bulk microphysics had a nearly constant cloud top height starting at 900 m and increasing to 980 m with an average height of 942 m. The SBM microphysics had a constant cloud top height

Table 3.1: A selection from published literature of the variety of grid sizes, models, and type of clouds which had the microphysics simulated by the HUJI SBM.

| Cloud Type | Domain Size | Grid Sizes | Reference | Notes |
|---|---|---|---|---|
| Multicell hail storm | 179.2 km × 16 km | $\Delta$x = 350 m, $\Delta$z = 125 m | *Khain et al.* (2011) | "A grid spacing of a few hundred meters resolves accurately[the] dynamical and microphysical processes which determine size distribution of hail and other hydrometeors." |
| Convective | 179.2 km × 16 km | $\Delta$x = 350 m, $\Delta$z = 125 m | *Noppel et al.* (2010) | Cloud seed with small aerosols |
| AMPS | 7.2 km × 7.2 km × 2.52 km | $\Delta$x = $\Delta$y = 100 m, $\Delta$z = 20 m | *Fan et al.* (2009a) | |
| Midlatitude squall line | 1024 horizontal points,<br>33 stretched vertical levels | $\Delta$x = 1 km for the center 872 points;<br>outer grids stretched,<br>$\Delta$z ranged from 240 m to 1250 m. | *Li et al.* (2009a,b) | Bin, bulk microphysics comparison<br>Bin scheme produces more homogeneous and realistic stratiform region |
| Convective (Marine, Continental, Pyro) | 178 km × 16 km | $\Delta$x = 250 m, $\Delta$z = 125 m | *Khain et al.* (2008b) | |
| Convective | 1024 horizontal points,<br>33 stretched vertical levels | $\Delta$x = 1 km for the center 872 points;<br>outer grids stretched,<br>$\Delta$z ranged from 240 m to 1250 m. | *Tao et al.* (2007) | Contains summary of CRM studies:<br>Disagreement between studies in precip. with changes to CCN |
| Sea breeze convection to squall line | Nested domain with 270 km north-south<br>300 km east-west direction | $\Delta$x = 3 (9) km in inner (outer) nested | *Lynn and Khain* (2007) | Bin, bulk microphysics comparison<br>Bulk has too much precip. too quickly |
| Evolution to Hurricane | Nested WRF, 400 km × 400 km in<br>inner nested domain, 31 stretched levels | $\Delta$x = 3 (9) km in inner (outer) nested | *Khain et al.* (2010) | |
| Squall line | 512 km,<br>81 stretched levels | $\Delta$x = 1 km<br>$\Delta$z ranged from few meters to several hundred at 20 km | *Khain et al.* (2009) | Bin, bulk microphysics comparison,<br>WRF-SBMfast, .<br>SBM closer to observations |
| Deep Convective | 768 × 72 grid points | $\Delta$x = 300 m horz,<br>$\Delta$z ranged from 100 m to 400 m | *Fan et al.* (2009b) | |
| Boundary Layer with intermittent drizzle | 30 km × 5 km | $\Delta$x = 500 m, $\Delta$z = 50 m | *Suzuki et al.* (2010) | |
| Deep convective | 128 km × 16 km | $\Delta$x = 250 m, $\Delta$z =125 m | *Khain et al.* (2005) | Quotes *Khain et al.* (2004)<br>"Increase of the model resolution does not influence results significantly." |
| Hurricane Structure and lightning | Nested WRF model | 250m HUCM in 2D | *Khain et al.* (2008a) | |
| Stratocumulus | 1340 Lagrangian parcels | Parcels on grid of $\Delta$x = 5 m | *Magaritz et al.* (2009) | Parcels were each about 40 m long |
| Convective | 1400 km × 1400 km,<br>40 stretched levels | $\Delta$x = $\Delta$y = 7 km<br>$\Delta$z ranged from 40 m to 1140 m. | *Iguchi et al.* (2008) | Bin, bulk microphysics comparison<br>Scheme matters with high CCN |
| Deep convective and squall line | 64 km × 15 km | $\Delta$x = 250 m, $\Delta$z = 125 m | *Seifert et al.* (2006) | Bin, bulk microphysics comparison<br>Results show more sensitivity to CCN number changes than to bin or bulk. |
| Orographic clouds | 494 km × | $\Delta$x = 1 km, $\Delta$z = 200 m | *Lynn et al.* (2007) | WRF-SBMwith clean/dirty CCN |
| Cloud formation and squall line | 3-layer nested domain of (small to large)<br>(900, 552, 400) km west-east ×<br>(765, 480, 199) km north-south | $\Delta$x = 1, 3, 9 km in nested domains<br>35 stretched vertical levels | *Lynn et al.* (2005a,b) | Bin, bulk microphysics comparison<br>SBMfast had longer-lasting clouds with development of stratiform clouds |
| Deep convective | 64 km × 16 km | $\Delta$x = 250 m, $\Delta$z = 125 m | *Khain and Pokrovsky* (2004)<br>*Khain et al.* (2004) | Description of SBM,<br>test of grid resolution in SBM,<br>test of spectral broadening in Euler models |

of 900 m throughout the entire simulation. The value of $q_T = 10^{-5}$ kg/kg is often used to define the boundaries of a cloud in observations, but the value of $q_T = 10^{-6}$ kg/kg has also been used. Redefining to $q_T = 10^{-6}$ kg/kg, then the bulk's average cloud top height is 946 m. With $q_T = 10^{-6}$ kg/kg, the SBM's redefined cloud top height varied between 900 m and 940 m for an average of 932 m. This was caused by including the ice particle number concentration values of $\sim$ 0.001 cm$^{-3}$ between 117.6 and 118.0 UTC. The bottom of the cloud in both the SBM and bulk is the bottom of the domain. The vertical model levels are $\Delta$ z = 40 m, so the differences between the average cloud top height of the bulk and the SBM within the model's resolution.

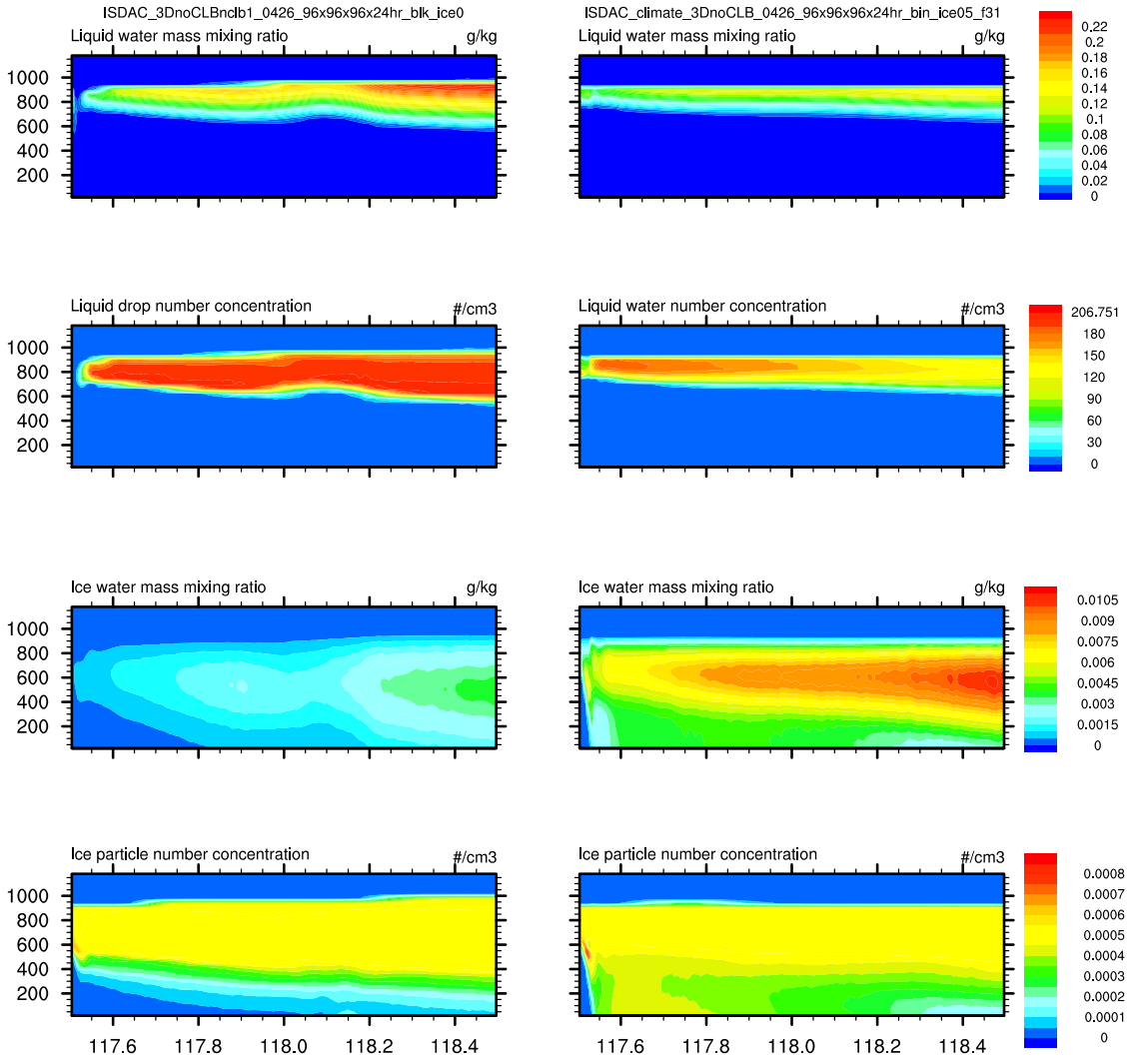


Figure 3.1: Time evolution of the 3D domain averaged cloud profiles for the bulk (left) and SBM (right) microphysics. The cloud liquid, cloud droplet number, cloud ice, and cloud ice number are shown from top to bottom for both microphysics routines.

### 3.2.2 Two-Dimensional Simulations of Bin and Bulk

Simulations in Two-Dimensions (2D) with the SBM have been tested and frequently used to analyze cloud systems. (See, for example *Khain et al.* (2004), *Khain et al.* (2005) and other references in Table 3.1.) 2D simulations were performed here for the SBM and bulk comparison and shown in Figure 3.2. The computational expense of the 3D SBM simulation made it difficult to obtain multiple simulations of the 3D SAM-SBM to test theories

and perform parameter sensitivities. A difference between the 2D and 3D simulated clouds includes a slightly higher cloud top height in the 2D simulation. Another difference is that the 3D clouds are averaged over another horizontal dimension containing 96 grid points in these time-height profile contour plots. This gives the appearance of the 3D simulations being more smooth and having fewer fine-scale features compared to the 2D. Similarities between the 2D and 3D simulations include the maximum values of the cloud liquid and ice mass mixing ratios and concentrations being almost equivalent. The 2D AMPS cloud simulations show the liquid mass and droplet number concentration is at the cloud-top, and the ice mass and number concentration exists throughout the cloud with precipitation towards the surface as seen in the 3D simulations. The 2D mixed-phase clouds are similar to the 3D mixed-phase clouds and will be used in this research to test theories and perform parameter sensitivities.

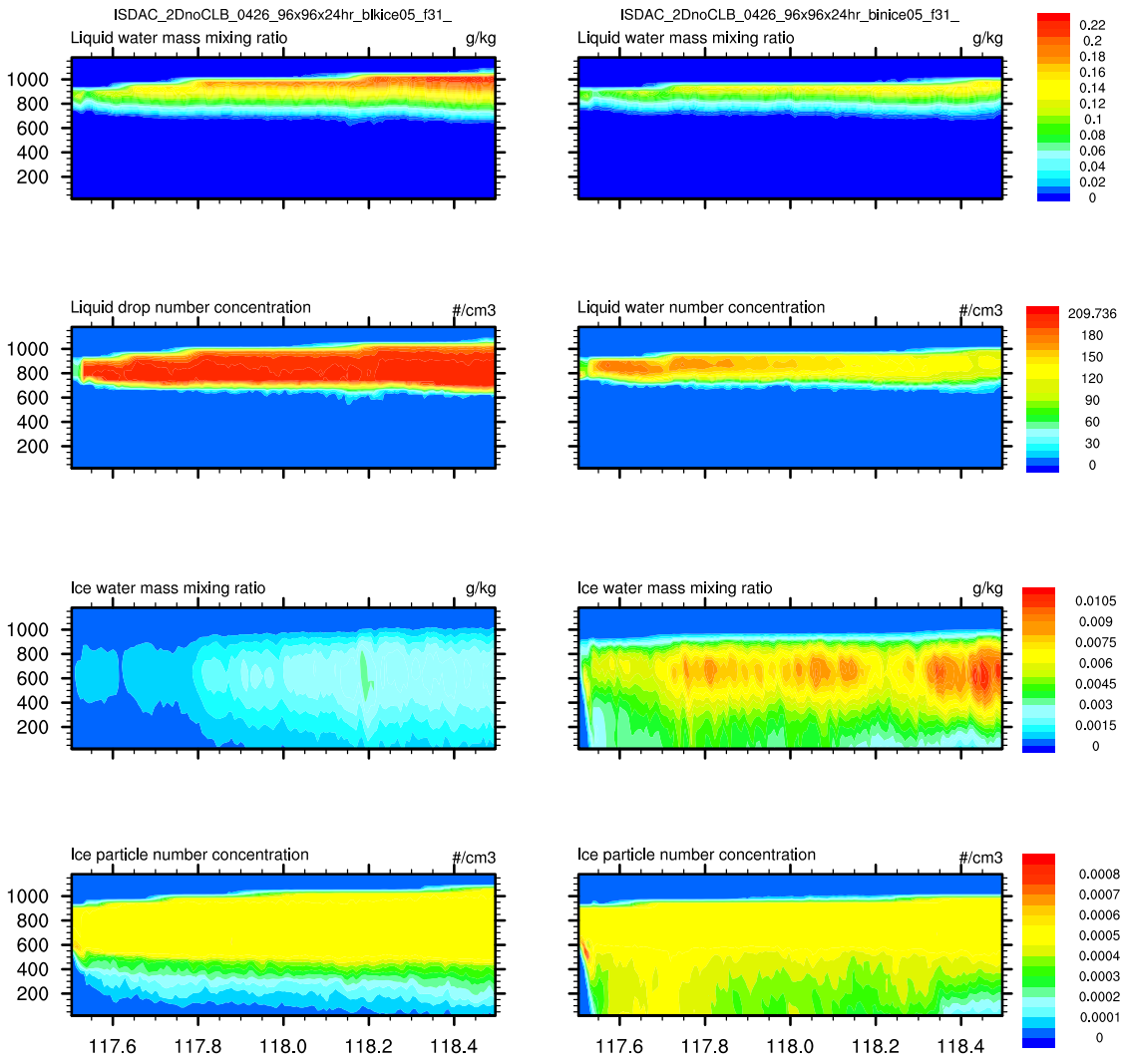


Figure 3.2: Time evolution of the 2D domain averaged cloud profiles for the bulk (left) and SBM (right) microphysics. The cloud liquid, cloud droplet number, cloud ice, and cloud ice number are shown from top to bottom for both microphysics routines.

### 3.2.3 Comparison with Observations

Profiles of the averaged liquid and frozen mass concentrations and number concentrations from simulations are compared with averaged ISDAC flight 31 measurements in Figure 3.3. The data from the aircraft was reported at 1 second intervals from instruments aboard aircraft described in *McFarquhar et al.* (2011). The flight data in Figure 3.3 represent several different flight patterns including two horizontal in-cloud legs and two

segments with the up-and-down, "porpoising", flight pattern. The ice water content and ice particle concentration are taken from probes which reflect particles larger than 100 $\mu m$ in diameter. Even though the smaller particles are not expected to contribute significantly to the ice mass, they are counted in the ice number concentration. Ice shattering effects would cause an artificial increase in ice number. Though the data has been adjusted to include this effect, remnants of small crystals from shattering might cause an overestimation in the ice number concentration (*M. Ovchinnikov, personal communication*).

In general, the profiles of the liquid mass and number concentrations have better agreement with the observations than the frozen mass and number concentrations. The variance of the in-flight data was considered when comparing to the simulation results. The one and two standard deviations, $\sigma$ and $2\sigma$, from the mean are shown as the shaded regions in Figure 3.3. The predicted peak in the mass mixing ratio is a few meters higher than what was measured. The cloud droplet number concentration in the bulk falls within the range of variability of the observations while the SBM slightly under predicted the magnitude of the droplets and their depth within the cloud. The maximum bulk droplet value is $\sim 20\%$ greater than the maximum droplet number predicted by the SBM and occurs 40 m lower in the cloud.

The predicted frozen mass and number concentrations did not fall within the observation range. The frozen mass concentration was under predicted in both the SBM and the bulk by an order of magnitude. The ice number concentration from the simulations was greater than the observations by a factor of 2 or more. There is also multiple peaks within the measured ice profiles. It is not directly known if this a commonly occurring feature in slightly precipitating AMPS such as these, or if the variability of the frozen species is related to ice shattering effects and the sampling techniques of the aircraft. A distinct feature of the both the SBM and bulk ice number concentration profiles is a sharp decrease in number concentration at 1000 m with a well-mixed layer beneath from about 950 m to 580 m. The number concentration gradually decreases to the surface. The ice condensate

is probably sublimating in the model because the mass of the frozen hydrometeors also decreases from about 580 m downwards while the water vapor mixing ratio increases by 10%. The SBM and bulk had the same frozen number concentration, and the SBM's frozen mass mixing ratio had values closer to observations at the top of the cloud compared to the bulk. This implies the SBM predicted larger frozen particles than the bulk. The observations show the presence of a small amount of liquid and ice from 1000 m to about 1100 m. The simulations, on the other hand, show a sharp transition from no liquid to liquid at the cloud top. The bulk simulations did produce a small amount of frozen condensate above 1000 m.

The averaged 2D results are compared to the inflight measurements and are shown in Figure 3.4. Compared to the 3D simulations in Figure 3.3, the 2D cloud top height increased by about $\sim$100 m. The maximum number of droplets in the cloud layer decreased by about 10 drops cm$^{-3}$ in the SBM while the maximum number of droplets increased by about 10 drops cm$^{-3}$ in the bulk. These maxima occurred 40 m in the 2D compared to the 3D. The frozen species for both the SBM and bulk show fewer differences when the dimensionality of the model was changed.

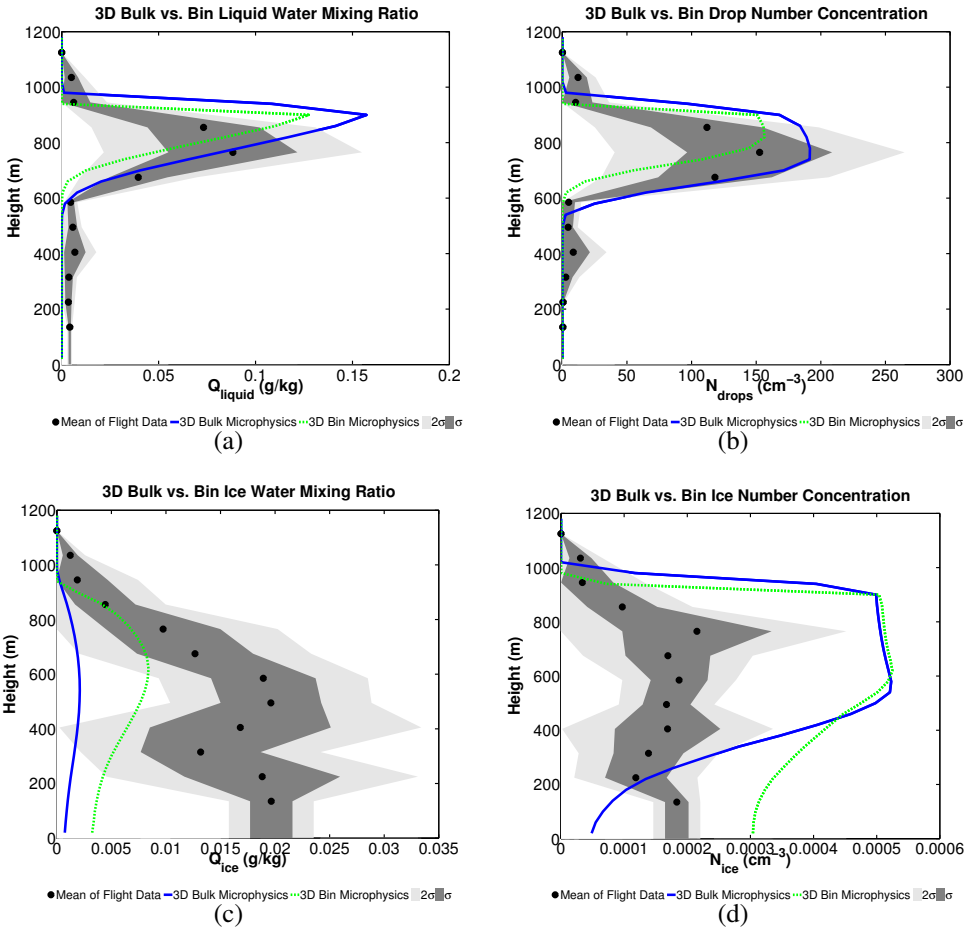


Figure 3.3: Cloud profiles from the bulk (blue lines) and SBM (green lines) microphysics. These plots are the average from the 3D-domain and 24-hour simulation period. The black dots are mean values from the measurements taken by the aircraft in the cloud on 26 April 2008. The light grey shading is two-times the standard deviation from the mean, and the darker grey shading is the standard deviation from the mean of the in situ measurements. Shown are total masses and number concentrations of the liquid and frozen hydrometeors. (a) Total liquid mass mixing ratio (g/kg), (b) Total liquid number concentration ($cm^{-3}$), (c) Total frozen mass mixing ratio (g/kg), and (d) total ice number concentration ($cm^{-3}$).

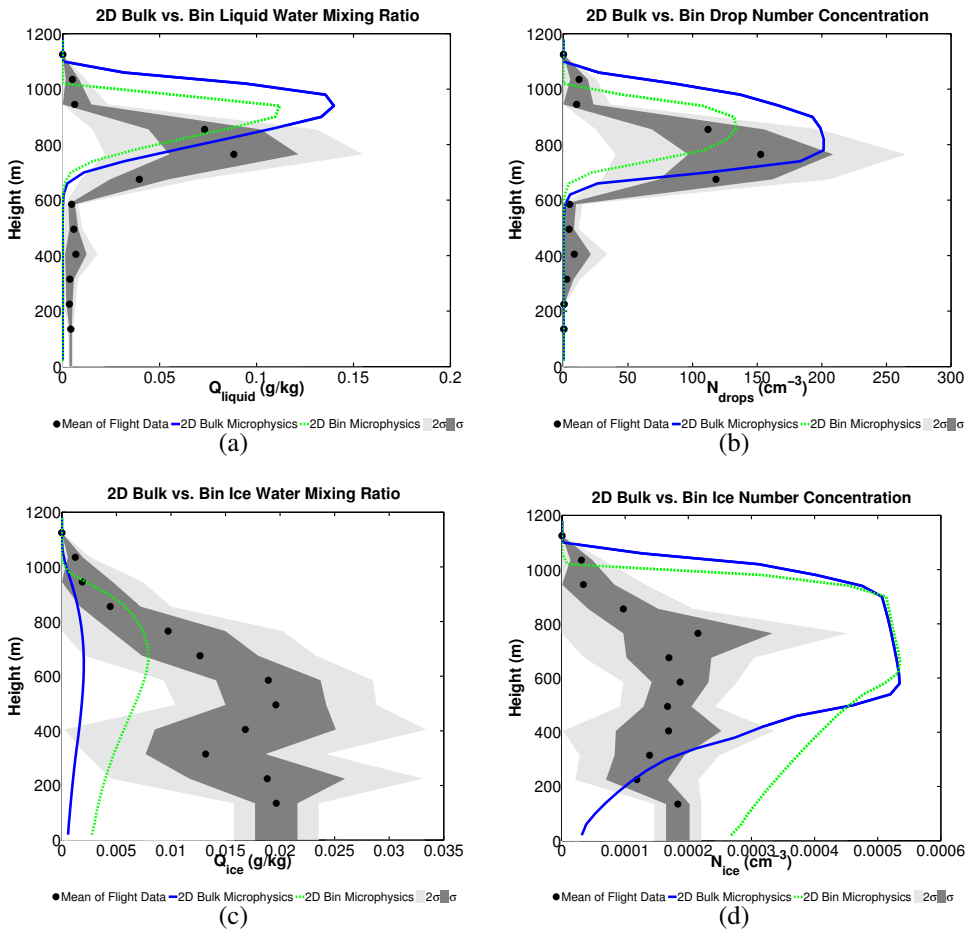


Figure 3.4: Cloud profiles from the bulk (blue lines) and SBM (green lines) microphysics. These plots are the average from the 2D-domain and 24-hour simulation period. The black dots are mean values from the measurements taken by the aircraft in the cloud on 26 April 2008. The light grey shading is two-times the standard deviation from the mean, and the darker grey shading is the standard deviation from the mean of the in situ measurements. Shown are total masses and number concentrations of the liquid and frozen hydrometeors. (a) Total liquid mass mixing ratio (g/kg), (b) Total liquid number concentration ($cm^{-3}$), (c) Total frozen mass mixing ratio (g/kg), and (d) total ice number concentration ($cm^{-3}$).

## 3.3 Discussion and Summary

It was found in the comparison of the microphysics schemes that both schemes are capable of producing the mixed-phase cloud for a 24 hour period. Both schemes produced a boundary-layer cloud with a liquid layer near the cloud top with ice precipitating from the cloud. When the simulated clouds were compared with observations, it was found that

they both did reasonably well in producing the magnitude and location of the liquid layer. Both schemes under predicted ice mass, but over predicted the ice number concentration compared with the observations. The bulk microphysics produced a liquid layer that was slightly larger and ice mass and number concentrations that were slightly smaller than the SBM. The cloud top height in the bulk scheme increases slightly in time compared to the SBM scheme where the cloud top height is constant for the 24 hour simulation.

The purpose of this comparison was to to assess the level of complexity needed to numerical reproduce an AMPS. The state-of-the-art SBM has well-documented cases showing its ability to realistically reproduce many cloud types including AMPS. It was found that the bulk microphysics produced a mixed phase clouds that was very similar to the SBM cloud, and that the bulk microphysics is capable to be used to simulate the mixed-phase.

# CHAPTER IV

# Comparison of Subgrid-Scale Turbulence Parameterizations

## 4.1 Introduction of Turbulence Parameterizations

Atmospheric processes span orders of magnitude in time and space. Chemical reactions and radiative processes occur in less than a second in a space smaller than a micron. Cloud systems, on the other hand, can take days to evolve and be hundreds of kilometers in size. A commonality between these two atmospheric processes is that there is movement in the atmospheric flow that mixes and moves the molecules and cloud mass. The mixing within the atmospheric processes is important to understand and model. The molecular mixing is important to understand because it determines the rate of formation of a product in a chemical reaction and how much of the new product exists. The mixing within the cloud system is important to understand because it determines the longevity, spatial extent, and microphysical characteristics of the clouds. The small-scale molecular processes and the large-scale cloud processes affect the fate and evolution of each other. In order to understand how these processes work and interact in the atmosphere, computational fluid dynamics and chemistry can model the reactions and the cloud mass. However it is not possible to directly model every reaction or cloudy parcel in time, so approximations in the form of turbulence parameterizations can be made of the smaller mixing processes so that

the larger motion of the atmospheric system is resolved.

In the research question here of understanding the fate of the Arctic Mixed-Phase Stratocumulus (AMPS) in a changing Arctic environment, the size and timescale of processes that are less than tens of meters will be parameterized so that a few-kilometer-sized portion of the cloud can be modeled for several hours. This choice of what to resolve (grid-scale) and what not to resolve (subgrid-scale) was made so that the numerical requirements of the cloud model, System for Atmospheric Modeling, v6.8.2 (SAM), as explained in Chapter II, would be met. This means that the smaller scales that will be parameterized are the concentrations of the ice and liquid cloud particles and motion that is less than the size of the grid box. The cloud particle parameterization is performed with microphysics schemes by predicting the bulk evolution of cloud particles instead of keeping track of every particle itself. As shown in Chapter III, the bulk and Spectral Bin Microphysics (SBM) microphysics have been used in many different scales of resolution for a wide variety of cloud systems, showing their ability to parameterize microphysical processes. The larger-scale motion that is resolved would be fluid movement that is greater than the grid box. Note that the nomenclature grid spacing and grid resolution are not synonymous, and that higher resolution implies smaller grid spacings.

Turbulence is generated by fluid motion and the development of buoyancy within an element of the fluid. The need for a parameterization for the mixing arises from terms in the equations of fluid motion that describe subgrid-scale energy due to the choice of the size of the physical system to be modeled. Historically, many techniques have been used to model the subgrid-scale fluid motion. In this research, two techniques will be compared for their ability to be used to model the fate of an AMPS. In this chapter, the governing fluid equations will be introduced followed by approximations made to the fluid equations so that they are more adaptable to numerical simulations. The subgrid-scale turbulent modeling techniques will then be introduced. Proceeding the theoretical background, results of these turbulent models when they are used in SAM to simulate an AMPS will be shown. Lastly,

the results are discussed.

## 4.2 Navier-Stokes Equations in Vector Form

In order to properly describe fluid motion, a system of equations needs to be defined to describe the fluid's mass transport, momentum, and energy. For a cloud system, additional equations are needed for radiation, phase changes of water, and heat, which be introduced after the equations for mass, momentum, and energy are presented.

Following the work of *Tannehill et al.* (1997), first consider the principle of conservation of mass for fluid passing through infinitesimal fixed control volume. Let $\partial\rho/\partial t$ be the rate of increase in density in the control volume, and $\nabla\cdot(\rho\mathbf{V})$ is the flux of mass leaving the control volume. Equation 4.1 shows the the conservation of mass for the control volume. Taking this view-point of the fluid is an Eulerian approach in the conservation law where the flux is written in divergence form. An incompressibility assumption will also be made, and is consider a good assumption for wind speeds less than 100 m/s.

$$\frac{\partial\rho}{\partial t} + \nabla\cdot(\rho\mathbf{V}) = 0 \tag{4.1}$$

The momentum equation is derived when Newton's Second Law is applied to a fluid passing through an infinitesimal control volume. The $\partial\rho/\partial t$ term in Equation 4.2 is the rate of increase of momentum in the control volume, the $\nabla\cdot\mathbf{VV}$ term is the rate of momentum lost of convection, $\rho\mathbf{f}$ is a body force acting on a unit volume (like a force at a distance that is applied to whole fluid, $\rho\mathbf{f} = \rho\mathbf{g}$), and $\nabla\cdot\mathbf{\Pi}_{ij}$ are the surface forces per unit volume. The momentum equation is applicable to continuum and non-continuum flows.

$$\frac{\partial\mathbf{V}}{\partial t} + \nabla\cdot\mathbf{VV} = \rho\mathbf{f} + \nabla\cdot\mathbf{\Pi}_{ij} \tag{4.2}$$

When $\Pi$ is approximated the equation looses generality to the type of flow. The definition of a Newtonian fluid is a fluid where the stress at a point is linearly dependent on the rates of strain (deformation) of the fluid. *Schlichting* (1968) derived a general deformation law relating the stress tensor to the pressure, $p$, and velocity,

$$\Pi_{ij} = -p\delta_{ij} + \mu\left(\frac{\partial u_i}{\partial x_j} + \frac{\partial u_j}{\partial x_i}\right) + \delta_{ij}\mu'\frac{\partial u_k}{\partial x_k}, \qquad \text{for i,j,k = 1,2,3} \tag{4.3}$$

where $\mu$ is the coefficient of viscosity (the dynamic viscosity), $\mu'$ is he 2nd coefficient of viscosity, and $k = {}^2\!/_3\mu + \mu'$ is the bulk viscosity, which is important in shocked fluids and fluids that attenuate/absorb sound waves. Otherwise, $k = 0$ in other fluids. The stress equation becomes

$$\Pi_{ij} = -p\delta_{ij} + \mu\left[\left(\frac{\partial u_i}{\partial x_j} + \frac{\partial u_j}{\partial x_i}\right) - \frac{2}{3}\delta_{ij}\frac{\partial u_k}{\partial x_k}\right] \qquad \text{for i,j,k = 1,2,3} \tag{4.4}$$

$$= -p\delta_{ij} + \tau_{ij}, \tag{4.5}$$

such that

$$\tau_{ij} = \mu\left[\left(\frac{\partial u_i}{\partial x_j} + \frac{\partial u_j}{\partial x_i}\right) - \frac{2}{3}\delta_{ij}\frac{\partial u_k}{\partial x_k}\right] \qquad \text{for i,j,k = 1,2,3.} \tag{4.6}$$

By relating the stress tensor to the pressure and velocity in the momentum equation, the more commonly-known Navier-Stokes equation is formed. It is also common to include the continuity and the energy equation and then call that set of equations the Navier-Stokes equations. The entire science of viscous flow is based on the Navier-Stokes equations, so if a constant viscosity is assumed, then the Navier-Stokes equations become a poor approximation for nonisothermal flow of a liquid whose viscosity is temperature-dependent. The

viscosity of a gas is only moderately temperature-dependent.

The energy equation is derived by applying the first law of thermodynamics to a fluid in a control volume. The first law of thermodynamics states that the energy of a closed system is constant, and that the change in internal energy in the closed system is equal to the amount of heat given to the system minus the amount of work done by the system on its environment. The total energy of the system, $E_t$, can be written as a sum of the individual sources of energy of the system, or $E_t = \rho(e+V^2/2+\text{potential energy}+...(\textit{other sources})+...)$. The time rate of change of the total energy of the system is given by Equation 4.7, where $e$ is the internal energy per unit mass, $\partial E_t/\partial t$ is the rate of increase of energy in the control volume, $\nabla \cdot E_t\mathbf{V}$ is the rate of total energy lost by convection, $\partial Q/\partial t$ is the rate of heat produced by external sources, $\nabla \cdot \mathbf{q}$ is the rate of heat lost by conduction (which can usually be described by Fourier's law of heat transfer by conduction, or $\mathbf{q} = -k\nabla T$), and $\rho\mathbf{f}$ is the work done on the control volume by surface forces,

$$\frac{\partial E_t}{\partial t} + \nabla \cdot E_t\mathbf{V} = \frac{\partial Q}{\partial t} - \nabla \cdot \mathbf{q} + \rho\mathbf{f} + \nabla \cdot (\mathbf{\Pi}_{ij} \cdot \mathbf{V}). \tag{4.7}$$

The mass continuity, momentum, and energy equations constitute the Navier-Stokes equations that are used by SAM to predict the atmospheric flow in space and time. SAM is a box-model and uses the Three-Dimensions (3D) (Cartesian) coordinate system. Between Equations 4.1, 4.2, and 4.7 in a Cartesian coordinate system, there are five equations and seven unknown variables. The five equations consist of the continuity equation, the three wind components ($u$, $v$, and $w$) in the momentum equation, and the energy equation. The seven unknowns are $\rho, p, u, v, w, e$, and $T$. This system of equations requires two more equations in order to be closed. The method is to establish a relationship between the thermodynamic variables ($p, \rho, T, e$) and relate the transport properties ($\mu, k$) to the thermodynamic variables. The state principle of thermodynamics can be used. The state principle

is where the local thermodynamic state is fixed by any two independent thermodynamic variables, provided there are no chemical reactions, so that the the ideal gas equation can be used,

$$p = \rho R T. \tag{4.8}$$

Also, assume the atmosphere is a calorically perfect gas, which is a gas that has constant specific heats, or constant specific heat at constant volume $e = c_v T$, constant specific heat at constant pressure $h = c_p T$, and the ratio of the specific heats is constant $\gamma = c_p/c_v$. Because $p = p(e, \rho)$, the equations to close the system are

$$p = (\gamma - 1)\rho e, \tag{4.9}$$

$$T = \frac{(\gamma - 1)e}{R}. \tag{4.10}$$

To relate the thermodynamic variables to the transport properties, kinetic theory is used for the transport coefficients. The Prandtl number, `Pr`, is used to determine $k$ once $\mu$ is known so that,

$$\mu = \frac{C_1 T^{3/2}}{T + C_2}, \tag{4.11}$$

$$k = C_3 \frac{T^{3/2}}{T + C_4}, \tag{4.12}$$

$$\mathrm{Pr} = \frac{c_p \mu}{k}. \tag{4.13}$$

## 4.3 Navier-Stokes in Tensor Notation

The system of equations has been introduced, and now a more convenient way to write the equations called tensor notation will be used. The index $i$, $j$, and $k$ have values equal to 1, 2, and 3 representing the $x$, $y$, and $z$ Cartesian coordinate values, respectively. If the index is repeated in a term, then that index's values should be expanded in a sum. If the index is alone in the term, then the choice of one of the values distinguishes the coordinate value the equation represents. The continuity and momentum equations are given in tensor notation below,

$$\frac{\partial \rho}{\partial t} + \frac{\partial (\rho u_i)}{\partial x_i} = 0, \tag{4.14}$$

$$\frac{\partial u_i}{\partial t} + \frac{\partial (u_i u_j)}{\partial x_j} = -\frac{1}{\rho}\frac{\partial p}{\partial x_i} + \frac{\partial}{\partial x_j}\left[\nu\left(\frac{\partial u_i}{\partial x_j} + \frac{\partial u_j}{\partial x_i}\right)\right] + f_i. \tag{4.15}$$

## 4.4 LES modeling of Turbulent Flow

The Navier-Stokes fluid equations have been introduced, and the way in which they are used in a model will now be described. To do that, first consider the motion within an atmosphere containing clouds where nonisotropic, disordered motion exists in the system. *Hinze* (1975) said that, "Turbulent fluid motion is an irregular condition of flow in which the various quantities show a random variation with time and space coordinates so that statistically distinct average values can be discerned." If the larger turbulent structures are assumed to be more irregular and nonisotropic, and the smaller scale structures are assumed to be nearly isotropic, then the theory of Large Eddy Simulation (LES) can be used. The theory behind LES modeling is that the large-scale structures of the turbulent flow in the system are computed directly, but the smaller scale structures of the system are approximated through a parameterization. The SAM model is based on the theory of LES, which assumes the largest turbulent eddies, or circular movements of the fluid, are resolved

in a chosen model grid spacing.

LES theory filters the Navier-Stokes equations to obtain a set of equations that predict the resolved flow. The space-averaging filtering should be over regions the size of the control volume. A different, but commonly known, type of filtering is the Reynolds-averaged Navier-Stokes (RANS) technique, which time-averages the Navier-Stokes equations. A big difference between the two types of filtering methods is the choice of quantities which are resolved. RANS cannot resolve time transients in the fluid flow because the filters equations will only predict a time-averaged wind field. RANS often accurately predicts the mean flow, but cannot predict complex flow with unsteady features, and it needs significantly less computing resources.

The Navier-Stokes equations are filters by assuming the flow, $u_i$, can be written as the sum of the mean and transient, residual flow. *Leonard et al.* (1975) developed this idea by decomposing the flow variables into large, resolved but filtered variables, $\overline{u}_i$, and the subgrid residual scales, $u_i'$,

$$u_i = \overline{u}_i + u_i'. \tag{4.16}$$

The filtered variable is defined by the convolution integral over the entire flow domain,

$$\overline{u}_i(x_1, x_2, x_3) = \iiint_D \left[ \prod_{j=1}^{3} G_j(x_j, x_j') \right] u_i(x_1', x_2', x_3') dx_1' dx_2' dx_3', \tag{4.17}$$

where the general filter function, $G$, is normalized to get back a correct value when $u$ is constant, so

$$\iiint_D \left[\prod_{j=1}^{3} G_j(x_j, x'_j)\right] dx'_1 dx'_2 dx'_3 = 1. \tag{4.18}$$

There are many types of filter functions, but the volume-averaged "box" and "top-hat" filter shown in Equation 4.4 is most frequently used in finite difference and finite volume calculations (*Aldama*, 1990). The explicit filter is interpreted as an implicit filter tied to the numerical resolution of a mesh. This means it becomes the finite-volume discretization of the flow equations and after discretization, the computed velocity field is a filtered velocity. The box filter size, $\Delta$, is equal to the grid resolution. The cutoff length is locally applied as the maximum mesh spacing over three dimensions. The filter function is written as

$$G_j(x_j - x'_j) = \begin{cases} \frac{1}{\Delta_j} & |x_j - x'_j| \leq \Delta_j/2 \\ 0 & \end{cases}$$

The decomposition and filtering of Equation 4.16 is applied to all prognostic variables in the atmospheric equations so that mean variables and residual variables will be predicted by the LES model, SAM.

In developing the predicative equations in SAM, *Khairoutdinov and Randall* (2003) used the anelastic assumption. This is an extension of the incompressible flow assumption, which assumes that the fluid density, $\rho$, is not necessarily or absolutely constant. It states that $\nabla \cdot (\rho_0 \mathbf{V}) = 0$. Inserting the mean and perturbed states into the continuity equation gives

$$\frac{\partial(\overline{\rho} + \rho')}{\partial t} + \frac{\partial((\overline{\rho} + \rho')(\overline{u}_i + u'_i))}{\partial x_i} = 0. \tag{4.19}$$

It is assumed that the gradients of the subgrid-scale density and pressure perturbations go to zero, so the averaged continuity equation becomes

$$\frac{\partial}{\partial x_i}\overline{\rho}u_i = 0. \tag{4.20}$$

The momentum equation is averaged in the same way, where

$$\frac{\partial(\overline{u}_i + u_i')}{\partial t} + \frac{\partial((\overline{u}_i + u_i')(\overline{u}_j + u_j'))}{\partial x_j} = \tag{4.21}$$
$$-\frac{1}{(\overline{\rho} + \rho')}\frac{\partial(\overline{p} + p')}{\partial x_i} + \frac{\partial}{\partial x_j}\left[\nu\left(\frac{\partial(\overline{u}_i + u_i')}{\partial x_j} + \frac{\partial(\overline{u}_j + u_j')}{\partial x_i}\right)\right] + f_i.$$

The product produced in the advective momentum term (the second term on the left), produces an term, $\overline{u_i u_j}$, in which the system of equations cannot solve both $\overline{u_i}$ and $\overline{u_i u_j}$. It can be decomposed into the following equation, where

$$\begin{aligned}\overline{u_i u_j} &= \overline{u}_i\overline{u}_j + (\overline{\overline{u}_i\overline{u}_j} - \overline{u}_i\overline{u}_j) + (\overline{u_i'\overline{u}_j} + \overline{\overline{u}_i u_j'}) + \overline{(u_i' u_j')}, \\ &= \overline{u}_i\overline{u}_j + \tau_{ij}.\end{aligned} \tag{4.22}$$

After the Navier-Stokes equations are filtered to remove small spatial scales, the result is a set of equations that can describe the evolution of large eddies. The averaged equations contain stress terms that can be closed through a parameterization, and this subgrid-scale stress tensor represents the effects of the unresolved small scales. An important difference in the time averaging technique, RANS, and spatial filtering, LES, is that $\overline{u_i u_j} \neq \overline{u}_i\overline{u}_j$. The first term in $\tau_{ij}$ is the Leonard stress, the second term is the cross-term stress, and the third term is the Reynolds stress. Time filtering causes the first two terms to be zero. The Leonard stress can be computed from the resolved flow, but is difficult with most finite difference and volume schemes. Its values is usually on the same order as the truncation error for second-order schemes. It is common for differencing schemes to assume the

subgrid-scale model accounts for all three terms of $\tau_{ij}$.

## 4.5 SAM Model Equations

Following *Khairoutdinov and Randall* (2003), the equations predicting the dynamic and thermodynamic properties of the atmospheric flow in SAM are derived from the spatial filtering technique and anelastic assumption described in the sections above. The mass continuity equation is given by Equation 4.20. The momentum equation and scalar conservation equations are listed in *Khairoutdinov and Randall* (2003) and are given by

$$\frac{\partial u_i}{\partial t} = -\frac{1}{\overline{\rho}}\frac{\partial}{\partial x_j}(\overline{\rho}u_i u_j + \tau_{ij}) - \frac{\partial}{\partial x_i}\frac{p'}{\overline{\rho}} + \delta_{i3}B + \epsilon_{ij3}f(u_j - U_{gj}) + \left(\frac{\partial u_i}{\partial t}\right)_{l.s.}, \quad (4.23)$$

$$\frac{\partial h_L}{\partial t} = -\frac{1}{\overline{\rho}}\frac{\partial}{\partial x_i}(\overline{\rho}u_i h_L + F_{h_L i}) - \frac{1}{\overline{\rho}}\frac{\partial}{\partial z}(L_c P_r + L_s P_s + L_g P_g) + \left(\frac{\partial h_L}{\partial t}\right)_{rad} + \left(\frac{\partial h_L}{\partial t}\right)_{l.s}, \quad (4.24)$$

$$\frac{\partial q_T}{\partial t} = -\frac{1}{\overline{\rho}}\frac{\partial}{\partial x_i}(\overline{\rho}u_i q_T + F_{q_T i}) - \left(\frac{\partial q_p}{\partial t}\right)_{mic} + \left(\frac{\partial q_T}{\partial t}\right)_{l.s}, \quad (4.25)$$

$$\frac{\partial q_p}{\partial t} = -\frac{1}{\overline{\rho}}\frac{\partial}{\partial x_i}(\overline{\rho}u_i q_p + F_{q_p i}) + \frac{1}{\overline{\rho}}\frac{\partial}{\partial z}(P_r + P_s + P_g) + \left(\frac{\partial q_p}{\partial t}\right)_{mic}. \quad (4.26)$$

As stated in *Khairoutdinov and Randall* (2003), "$u_i (i = 1, 2, 3)$ are the resolved wind components along the Cartesian $x$, $y$, and vertical $z$ directions, respectively; $\rho$ is the air density; $p$ is pressure; $h_L$ is the liquid/ice water static energy equal to $c_p T + gz - L_c(q_c +$

$q_r) - L_s(q_i + q_s + q_g)$; $q_T$ is total nonprecipitating water (water vapor + cloud water + cloud ice) mixing ratio ($= q_v + q_c + q_i = q_v + q_n$); $q_p$ is total precipitating water (rain + snow + graupel) mixing ratio ($= q_r + q_s + q_g$); $f$ is Coriolis parameter; $U_g$ is prescribed geostrophic wind; $B$ is buoyancy given by

$$B = -g\frac{\rho'}{\rho} \approx g\left(\frac{T'}{T} + 0.608q_v' - q_n - q_p - \frac{p'}{\overline{p}}\right); \tag{4.27}$$

$g$ is gravitational acceleration; $c_p$ is specific heat at constant pressure; $L_c$ and $L_s$ are latent heat of evaporation and sublimation, respectively; $\tau_{ij}$ is subgrid-scale stress tensor; $F_{h_L}$, $F_{q_T}$, and $F_{q_p}$ are subgrid-scale scalar fluxes; $P_r$, $P_s$, and $P_g$ are rain, snow, and graupel precipitation fluxes, respectively; the subscript "rad" denotes the tendency due to radiative heating; "mic" represents the tendency of precipitating water due to conversion of cloud water/ice and due to evaporation; "l.s." denotes the prescribed large-scale tendency; the overbar and prime represent the horizontal mean and perturbation from that mean, respectively." The constituent species in the total water mixing ratio, $q_t$, will change depending on the specific microphysics scheme used. The species listed above are specific to the original microphysics scheme developed for SAM, which was a one-moment scheme. When the bulk and bin schemes are used, the additional cloud species are summed into the either ice or water cloud species depending on their state. For example, hail would be summed with ice, grapple and snow into cloud ice and then used model equations of motion.

## 4.6 Subgrid-Scale models of Turbulent Flow in LES models

SAM's equations of fluid motion have been given, and now the subgrid-scale models will be introduced. In a glance of turbulent motion, the fluid appears to be random and chaotic. After closer observation, rotational flow structures, turbulent eddies, can be discerned. These turbulent eddies comprise a large range of sizes and with varying life-

times. Recall that in the fluid motion the length and time scales vary. The largest eddies are aligned in the same direction as the mean flow. They are driven by the mean flow and contain the most turbulent kinetic energy. Their shapes and locations in the total fluid is anisotropic. The velocity gradient tapering from mean flow causes the largest eddies's vortex to be stretched. Their rotational movement drives the local fluid surrounding them, and energy is transferred to the smaller eddies nearby. The same relationship is continued from the second largest eddy to the next size, et cetera. As the size decreases, they loose the orientation and directionality of the larger eddies and become isotropic. The viscous forces begin to remove energy. The large eddies which carry the kinetic energy are not inviscid processes, but the smallest eddies are dominated by viscous forces. Between the largest and the smallest is the inertial subrange.

In an LES model that is well-resolved, the unresolved, subgrid-scale features should be small and carry little to no turbulent kinetic energy. They should be dissipative in nature and be in the inertial subrange. *Tannehill et al.* (1997) and *Bechmann* (2006) have both asserted that subgrid-scale motion tends to be isotropic and universal. The subgrid-scale model should mimic the energy drain as seen in viscous, dissipative scales. Some subgrid-scale models take a Boussinesq approach where the subgrid-scale stresses are assumed to be a product of the fluid strain and eddy viscosity $\mu_T$. The turbulent transport of momentum is akin to molecular transport with the small eddies modeled as molecules, and their characteristic length being similar to the mean-free path. The analogy ends with $\mu_T$, where $\mu_T$ contains the properties of the turbulence, not the properties of the fluid (unlike molecular diffusion).

SAM has three turbulence closure models that will be introduced in the following subsections. The first type is the Smagorinsky-type subgrid-scale turbulence closure model, which is a first-order scheme. The second of closure model is called a 1.5-order closure model and is described by *Deardorff* (1980a). SAM was recently coupled with Cloud Layers Unified By Binormals (CLUBB), which is a higher-order turbulent parameterization,

and is the third type of turbulence closure model within SAM.

### 4.6.1 Smagorinsky Model

The Smagorinsky subgrid-scale model in SAM was originally developed for a model used in 1963 that was a nine vertical-level general circulation model for the atmosphere. The model equations of motion in *Smagorinsky* (1963) were primitive-variable form of the equations, meaning $p$, $u$, $v$, and $w$ are used, not vorticity or the stream-function approach. The model equations of motion predict the x-and y-dimensions, and had models for radiation, subgrid-scale vertical and lateral mixing, and condensation. *Smagorinsky* (1963) closed the equations of motion for the change in momentum due to the Reynold's stress and the change in temperature due to subgrid-scale mixing by defining a mixing length that was a function of the grid spacing and coarse vertical height. This mixing length, or gradient diffusion model, assumes isotropic turbulence. The turbulent characteristic length scale, $l_s$, was given by

$$l_s = C_s \Delta, \tag{4.28}$$

where $\Delta$ is the grid resolution and $C_s$ has values ranging from 0.1 - 0.24, depending on the nature of the fluid. A common value to use is 0.1. The Smagorinsky model does not allow backscatter, or the idea that dissipative forces give energy back to the larger eddies and is derived from the assumption that there is relationship between the shear production and the dissipation of the turbulent kinetic energy.

Recalling the subgrid-scale stress tensor in the momentum equation, Equation 4.23, $\tau_{ij}$ can be represented by

$$\tau_{ij} = 2\mu_T S_{ij}, \tag{4.29}$$

where $S_{ij}$ is the rate of strain tensor,

$$S_{ij} = \frac{1}{2}\left(\frac{\partial u_i}{\partial x_j} + \frac{\partial u_i}{\partial x_i}\right), \tag{4.30}$$

and

$$\mu_T = \rho(C_s\Delta)^2\sqrt{S_{ij}S_{ij}}. \tag{4.31}$$

Because *Smagorinsky* (1963) used primitive equations, there were no unresolved, perturbation terms that resulted from the LES filtering. This is the Smagorinsky-type closure that is described in *Khairoutdinov and Randall* (2003). SAM's model equations are filtered equations, so additional relationships are needed to close the eddy correlation terms. The next section describes those relationships to close the equations.

### 4.6.2 1.5-Turbulent Kinetic Energy Model

*Deardorff* (1980a) developed a 3D model to analyze, resolve, and predict turbulence and entrainment in stratocumulus-capped mixed layers. In this development, resolved and subgrid-scale terms appear in the momentum and temperature equations, and the subgrid-scale Turbulent Kinetic Energy (TKE), $\overline{E}$ is coupled to the equations of motion. It is governed by

$$\frac{\partial E}{\partial t} = -\frac{\partial}{\partial x_i}(\overline{u}_i\overline{E}) - \overline{u_i'u_j'}\frac{\partial \overline{u}_i}{\partial x_j} + \frac{g}{\theta_0}\overline{w'\theta_v'} - \frac{\partial}{\partial x_i}\overline{[u_i'(e' + p'/\rho_0)]} - \epsilon, \tag{4.32}$$

$$\tag{4.33}$$

where $e' \equiv (u'^2 + v'^2 + w'^2)/2$ and $\epsilon$ is the rate of dissipation within the grid volume. The first term is the energy storage, the second term is turbulent energy transport, the third term is shear production, the fourth term is buoyancy production, the fifth term is a downgradient diffusion assumption, and the sixth term is the dissipation. Subgrid fluxes are parameterized by

$$\overline{u_i'u_j'} = -K_m(\partial\overline{u}_i/\partial x_i + \partial\overline{u}_j/\partial x_i) + (2/3)\delta_{ij}\overline{E}, \tag{4.34}$$

$$\overline{u_i'\theta_l'} = -K_h\partial\overline{\theta}_l/\partial x_i, \tag{4.35}$$

$$\overline{u_i'q_w'} = -K_h\partial\overline{q}_w/\partial x_i, \tag{4.36}$$

$$\overline{u_i'\theta_v'} = \overline{Au_i'\theta_l'} + B\overline{\theta u_i'q_w'}, \tag{4.37}$$

$$\overline{u_i'(e' + p/\rho)} = -2K_m\partial\overline{E}/\partial x_i, \tag{4.38}$$

where $K_m$ is the subgrid scale eddy coefficient for momentum, $K_h$ is the subgrid eddy coefficient for scalar quantities, and $A$ and $B$ are approximately constants given by

$$A = 1 + 0.61\overline{q}_w, \tag{4.39}$$

$$B = 0.61, \tag{4.40}$$

in unsaturated air, and

$$A = (1 + 0.61q_w) - E_3 \left[ \frac{L}{c_p \overline{\overline{T}}} (1 + 0.61q_w) - 1.61 \right], \tag{4.41}$$

$$B = \frac{L}{c_p \overline{\overline{T}}} - 1, \tag{4.42}$$

with

$$E_3 = 0.622 \frac{L}{R\overline{\overline{T}}} \overline{q}_s \left( 1 + 0.622 \frac{L}{R\overline{\overline{T}}} \frac{L}{c_p \overline{\overline{T}}} \overline{q}_s \right)^{-1} \tag{4.43}$$

in saturated air where $R$ is the gas constant for air, $q_s$ is the saturation specific humidity, $q_w = q + q_l$ is the total specific humidity, $\theta_l$ is the liquid water potential temperature, $\theta$ is the potential temperature, $L$ is the latent heat of vaporization, $c_p$ is the specific heat at constant pressure, and $T$ is the absolute temperature.

The subgrid-scale eddy coefficients for momentum and scalar quantities are given by

$$K_m = 0.10 l \overline{E}^{1/2}, \tag{4.44}$$

and

$$K_h = (1 + 2l/\Delta s) K_m, \tag{4.45}$$

where $\Delta s = (\Delta x \cdot \Delta y \cdot \Delta z)^{1/3}$. The subgrid-scale mixing length, $l$, is required not to exceed the grid scale, $\Delta s$ in magnitude. It is possible for $l = \Delta z$ for stable regions containing negative buoyancy, otherwise

$$l = l_s = 0.76\overline{E}^{1/2}\left(\frac{g}{\theta_0}\frac{\partial\overline{\theta}_l}{\partial z}\right)^{-1/2} \tag{4.46}$$

The final relationship needed to close Equation 4.33 to close the equations of motion is the dissipation rate, $\epsilon$, which is given by

$$\epsilon = C\overline{E}^{3/2}/l, \tag{4.47}$$

where $C = 0.19 + 0.51l/\Delta s$.

The TKE is calculated in SAM using these equations, and the relationships containing the subgrid-scale eddy coefficients are used to close the equations to predict fluid motion for diffusion and then for the next time step. A drawback of the 1.5-TKE scheme is its reliance on specifying the length scale, which changes according to the atmospheric state.

### 4.6.3 CLUBB Model

The subgrid-scale models developed by *Smagorinsky* (1963) for a global climate model (GCM) and *Deardorff* (1980a) for a boundary-layer cloud modeled in a Cloud Resolving Model (CRM) were presented. These two subgrid-scale turbulence models have been used in many types of atmospheric models. Over the decades of their use, they have both shown fidelity in simulating atmospheric processes. Recently, a new, higher-order turbulence parameterization called CLUBB was developed with the purpose that it could be used to model the subgrid-scale turbulence for all cloud types and grid resolutions. This section introduces CLUBB then evaluates its performance in modeling AMPS.

Recollect that to predict the fluid motion in time, the Navier-Stokes equations are filtered by means of LES spatial filtering. After filtering the equations, resolved, mean-flow variables and perturbed correlated variables are predicted in space and time. First-order

perturbation variables are derived from filtering the Navier-Stokes equations once. Second-order perturbation variables are derived by subtracting the first-order equations from the unfiltered equations. Higher-order terms can be generated in the same way. CLUBB predicts the mean flow, first-order, and second-order variables.

The third-order terms are calculated with a statistical Probability Distribution Function (PDF) method. The PDF method is applied as follows in Figure 4.1, which is reproduced from a presentation given by V. Larson, circa 2005. In a CLUBB time step, the first-order term represents the mean, which is predicted by the numerical model. The second-order terms are advanced by integrating the PDF which finds the third-order moments. The family of PDFsare chosen to be Gaussian and quasi-normal so that odd-ordered moments do not vanish (*Golaz et al.*, 2002; *Larson et al.*, 2002). For the moments or correlations of the variables, the variables can be computed by integrating over the PDF,

$$\overline{w'^l \theta_l'^m q_l'^n} = \int \int \int (w - \overline{w})^l (\theta_l - \overline{\theta_l})^m (q_t - \overline{q_t})^n \times P(w, \theta_l, q_t)\, dw\, d\theta_l\, dq_t, \quad (4.48)$$

where $w$ is the vertical velocity, $\theta_l$ is the liquid water potential temperature, $q_t$ is the total specific water content, $P(w, \theta_l, q_t)$ is a joint PDF, $l$, $m$, and $n$ are positive integers denoting the order of the moment. Because the PDF is a double Gaussian family, the solution is analytical and an equation consisting of the product of the widths, locations, and mean values of the variables is produced. This is written in Figure 4.1 as PDF $=$ $\mathrm{G}_1 + \mathrm{G}_2$. The PDF closed the higher order moments, which is then able to advance the prognostic equations.

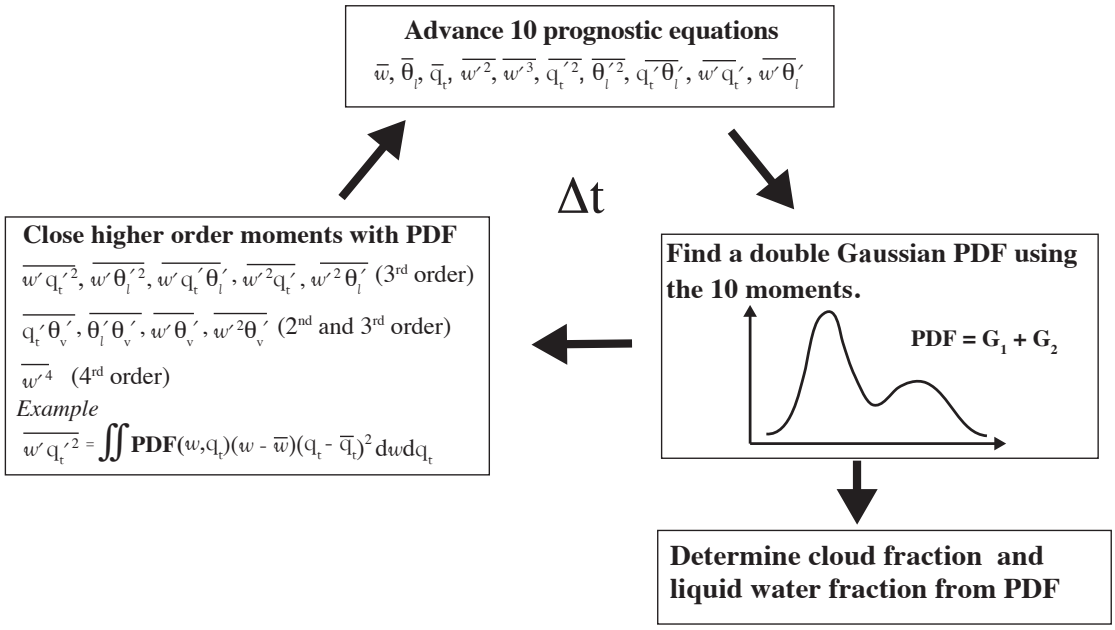


Figure 4.1: Credit: Diagram showing the algorithm of CLUBB used to close the higher-order moments and the prognostic equations. Within every CLUBB time step, the double Gaussian PDF is found for the higher order moments by integrating the PDF. The solution to the integral is analytical, as denoted by the sum of $G_1$ and $G_2$, which are functions of the mean value and widths of the PDF. This sum is the solution to the higher-order terms, which are then used to close the prognostic equations for the mean and second-order moments. The algorithm is performed in every grid box at every time step. This figure is replicated from the powerpoint created by V. Larson, circa 2005, which describes the published work of *Golaz et al.* (2002); *Larson et al.* (2002).

The second-order horizontal winds, $\overline{u'w'}$ and $\overline{v'w'}$, are closed with a downgradient diffusion approach, i.e., $\overline{u_i'w'} = -K_m \partial \overline{u_i}/\partial z$. As in the 1.5-TKE method of *Deardorff* (1980a), this gradient is proportional to $\Delta$, the grid size. In addition, the second- and third-order prognostic equations of the product of vertical velocity and thermodynamic variables closed from the joint PDF contain dissipation terms. Each of these dissipation terms are functions of an eddy length scale (*Golaz et al.*, 2002). The eddy length scale is calculated from the idea that a given parcel's buoyancy within the vertical column will vertically rise displaced by a certain distance based on its initial kinetic energy. Limits are set on the length scale for numerical instability, and the maximum value of the length scale in CLUBB can be $1/4$ $\Delta$. Table 4.1 presents a list of calculated quantities from the filtered

Navier-Stokes equations and compares which quantities are calculated by either using or not using CLUBB.

Table 4.1: A summary of the differences in calculated quantities between the 1.5-TKE scheme and CLUBB.

| Calculated Quantities | No CLUBB | CLUBB |
|---|---|---|
| Mean Flow | $\times$ | $\times$ |
| Turbulent Energy | $\times$ | $\times$ |
| $2^{nd}$-order Fluxes | $\times$ | $\times$ |
| $3^{rd}$-order Fluxes | | $\times$ |
| Max Subgrid-Scale Length Scale | $\Delta x$ | $1/4\ \Delta x$ |

## 4.7 Experiment design

The Smagorinsky, 1.5-TKE, and CLUBB models are used in SAM to see the differences in turbulence modeling schemes on the mixed-phase cloud structure. The same model set-up was used in this turbulence comparison as in the microphysics comparison in Chapter III. CLUBBv1.18 was used in SAM, and modifications to SAM to use CLUBB were made by the CLUBB development team. Appendix **??** contains the flow chart of how these models were used in SAM. CLUBB was called every dynamical time step, or every $\Delta t_{dyn}$ = 2 s.

## 4.8 Results and Discussion

### 4.8.1 Results with CLUBB and without CLUBB using the Bulk Microphysics

Figure 4.2 shows the time-height simulated cloud using SAM with and without CLUBB. The bulk without (left panels) and with (right panels) CLUBB are shown in Figure 4.2. The cloud liquid mass mixing ratio is shown in the top set of contoured plots followed by the liquid number concentration, the ice mass mixing ratio, and the ice concentration.

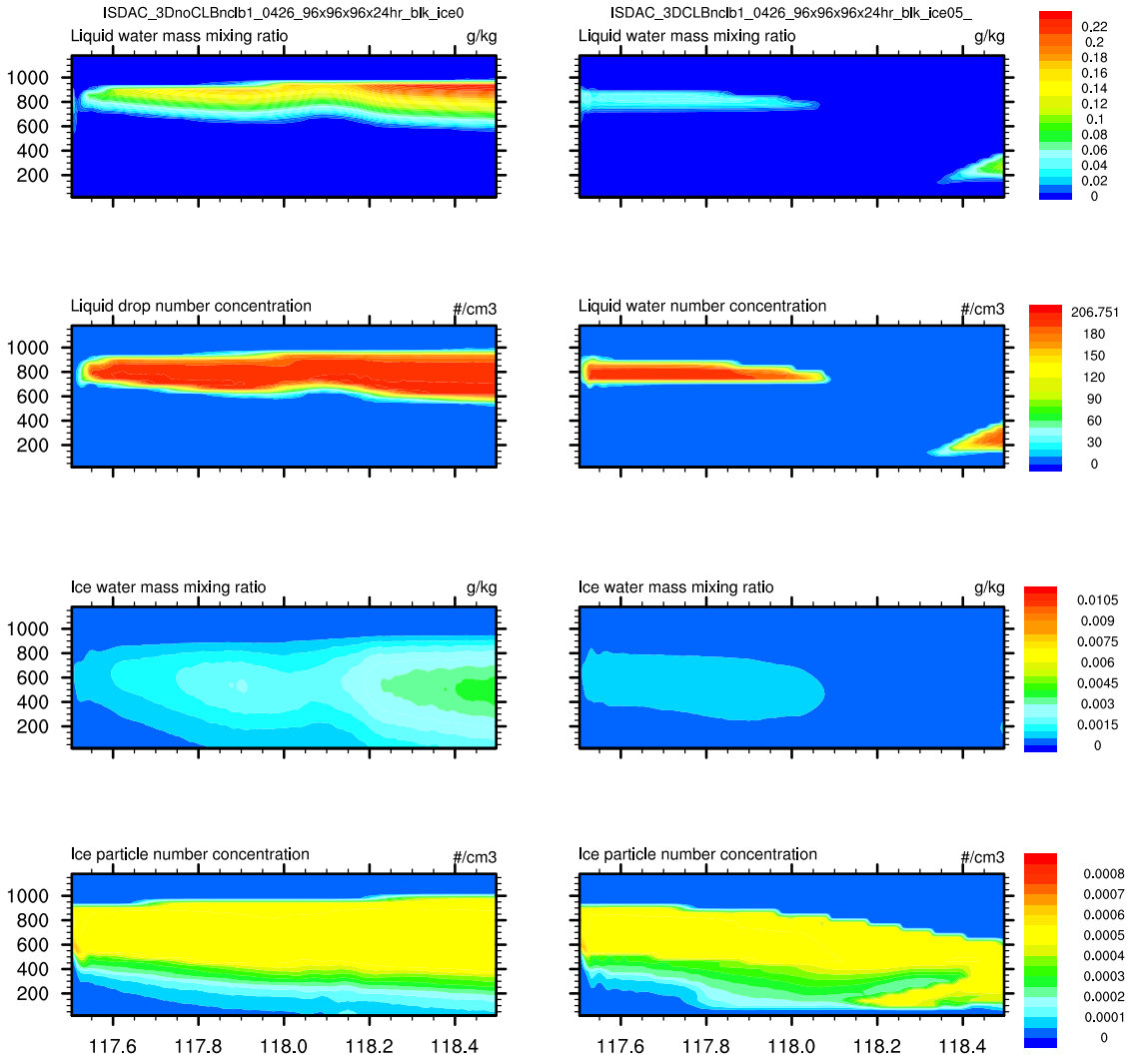


Figure 4.2: Evolution of the averaged cloud profiles of liquid and ice masses and concentration from the SAM without CLUBB (left) and SAM-CLUBB (right) with bulk microphysics from the 24 hour simulation period.

The effect of CLUBB with the bulk microphysics on the cloud properties is significant. The domain-averaged liquid water mass produced with CLUBB starts with a larger cloud depth than without CLUBB in the first few timesteps. The liquid cloud top begins to decrease, and the liquid mass of the cloud decreases and eventually dissipates just over 12 hours into the simulation. The cloud liquid is zero for about five hours until surface fluxes of water vapor begin to condense and cause a condensed layer at the surface. The ice mass mixing ratio is depleted as well. The magnitude of the ice number concentration has a

nearly constant value, and the height at which ice crystals exists decreases over time.

The loss of liquid without an increase in ice suggests a rehumidification of the atmospheric layer from the liquid being converted to vapor. The loss of liquid decreases the longwave cooling at cloud top. Figure 4.3 shows profiles of the temperature and water vapor mixing ratio, $q_v$, at four points in time during the cloud's simulation. At 117.8 UTC, about 2 hours into the simulation, the bulk microphysics without CLUBB has a temperature inversion of 4°K just below 1000 m. The inversion is maintained and increases to a 6°K as the cloud top and the liquid layer increases in Figure 4.3a. The water vapor profiles show a loss of water vapor at cloud top and above the cloud, but with an increase of water vapor below cloud in Figure 4.3c. The temperature profiles of the CLUBB cloud are initially the same magnitude as the no-CLUBB cloud in Figure 4.3b. As the cloud top height decreases and the liquid evaporates, the size of the inversion decreases. In Figure 4.3d, the water vapor increases at 100 m, which is the source of the low-level condensation later at 118.4 UTC.

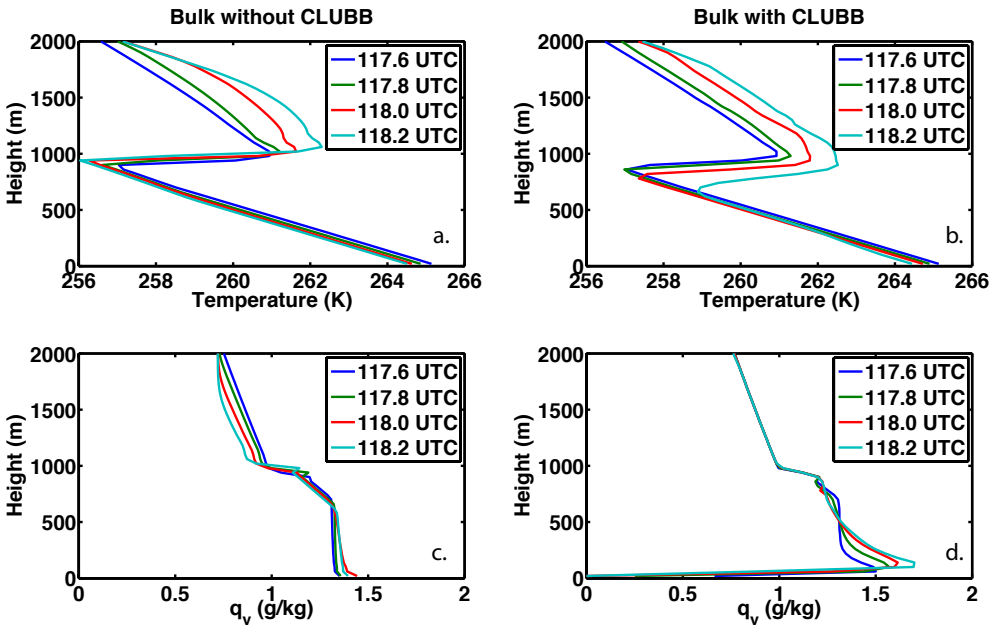


Figure 4.3: Profiles of the domain-averaged temperature (top, (a) and (b)) and water vapor mixing ratio, $q_v$, (bottom, (c) and (d)) for 3D bulk without CLUBB (left, (a) and (c)) and bulk with CLUBB (right, (b) and (d)). The profiles are given at four points in time during the simulations: 117.6 UTC in blue, 117.8 UTC in green, 118.0 UTC in red, and 118.2 UTC in turquoise.

The magnitude of the vertical velocity is the cause of the liquid water depletion in the cloud when CLUBB is used. The cooling rate of an ascending air parcel is proportional to the magnitude of the vertical velocity. Because the rate at which the parcel cools determines its supersaturation with respect to the environment, a larger vertical velocity updraft causes higher supersaturations with more liquid water formed in the parcel. Figure 4.4 shows the maximum vertical velocity in the entire domain in the 3D simulations of the bulk microphysics with and without CLUBB over the simulated 24 hours. The maximum vertical velocity in the cloud without CLUBB increases from 0.25 m/s to about 2.5 m/s within the first few hours. The magnitude of the maximum vertical velocity is held between about 2 m/s and 3 m/s throughout the simulated period. In contrast to the simulation that uses CLUBB, the magnitude of the maximum vertical velocity slowly decreases. A positive feedback is established between the maintained liquid water and with the maximum verti-

cal velocity in the cloud when CLUBB is used. The lack of buoyant parcels with energetic vertical velocities showed that CLUBB cannot lift parcels to saturation and condensation.

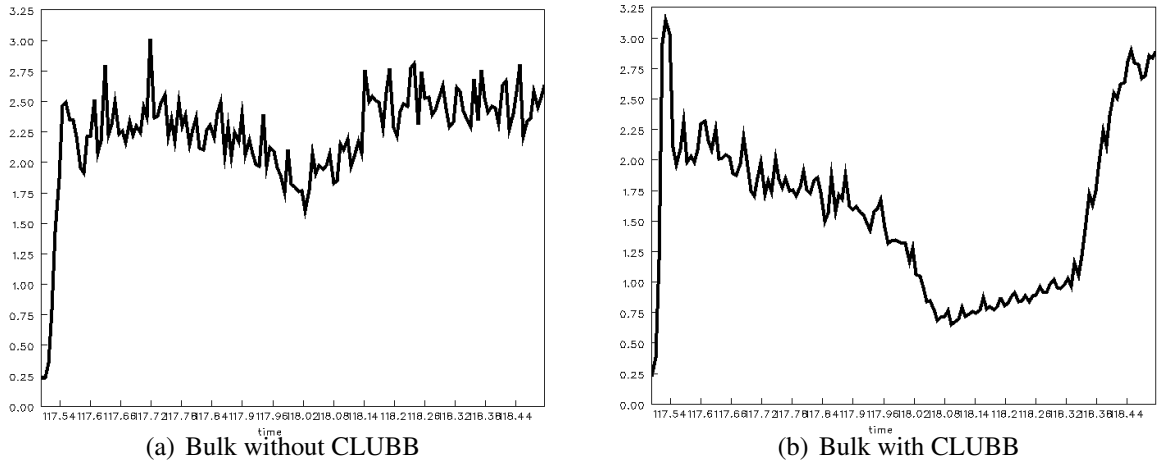


(a) Bulk without CLUBB (b) Bulk with CLUBB

Figure 4.4: The maximum vertical velocity (m/s) in the 3D domain plotted as a function of simulated time for (a) bulk microphysics without CLUBBand (b) bulk microphysics with CLUBB.

Another indication of how CLUBB is affecting the structure of the AMPS is from the vertical velocity skewness. Vertical velocity skewness, $Sk_w$, is given by

$$Sk_w = \overline{w'^3} / \overline{w'^2}^{3/2}, \tag{4.49}$$

where $w'$ is the fluctuation from the mean vertical wind, $\overline{w'^3}$ is the triple correlation, and $\overline{w'^3}$ is the variance. In the prognostic equation for $\overline{w'^2}$, the vertical transport of $\overline{w'^2}$ by the turbulence is represented by the triple correlation, $\overline{w'^3}$. When $\overline{w'^3}$ is positive, both $\overline{w'^2}$ and TKE are transported upwards (*Bougeault*, 1981; *Bougeault and Andre*, 1986; *Golaz et al.*, 2002; *Hogan et al.*, 2009). When the turbulence is generated at the top of the mixed layer due to cooling from above, TKE increases with height and is transported downwards. The energy is dissipated into heat, and the downdrafts should be more intense than the updrafts. The skewness would also be negative. *Hogan et al.* (2009) observed this scenario

in nocturnal stratocumulus where the turbulence is driven by cloud-top radiative cooling and the vertical velocity skewness was negative.

In the AMPS, the vertical velocity skewness, $Sk_w$, is shown for the bulk microphysics with and without CLUBB in Figure 4.5. When CLUBB is not used, $Sk_w$ is shown to increase from about $-3.0$ to 2.4 at the cloud top. When the time is about 118.0, the peak solar insolation occurs. This causes turbulent energy to be created at the surface from heat fluxes and transported vertically upwards. The buoyant parcels are dry compared to the air above because there is no source of water vapor at the surface. Instead of causing the vertical extent of the cloud to increase, the increase in TKE from the surface evaporates the liquid condensate because entrains dry air into the cloud. The cloud recovers as the solar insolation decreases, and the $Sk_w$ returns to being negative in the boundary layer. The AMPS cloud produced with CLUBB shows negative $Sk_w$ in the boundary layer and a positive $Sk_w$ at the cloud top height. Above the cloud, the $Sk_w$ is not definitely positive in both the simulations. These near-zero values from 1.5 kilometer upwards show TKE in this part of the domain and is dissipated in the space above the cloud.

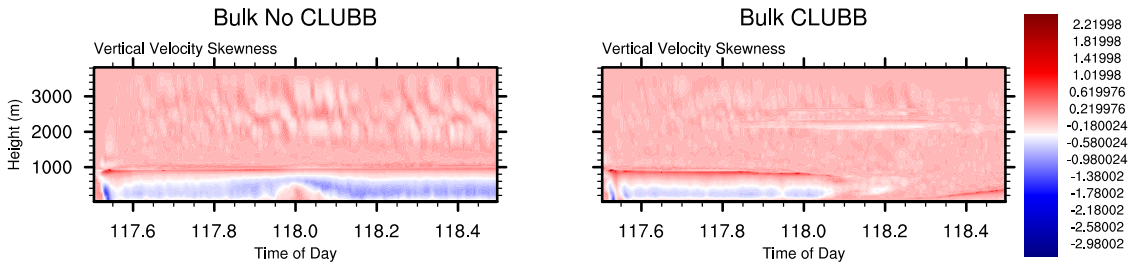


Figure 4.5: The vertical velocity skewness in the 3D domain plotted as a function of simulated time for bulk microphysics without CLUBB (left) and bulk microphysics with CLUBB (right).

As seen in the contoured plots of Figure 4.5, the values of the $Sk_w$ at a given time change significantly. The domain-mean of $Sk_w$ is shown in Figure 4.6 can summarize the time-height contoured plots. The vertical velocity skewness begins with negative values in the cloud produced with CLUBB, but after the cloud completely disappears at time 118.0,

the skewness values increase and become positive. This is due to the turbulent energy produced from the latent heat released as the condensed layer is formed at the surface towards the end of the 24 hours. The cloud produced without CLUBB has, on average, negative $Sk_w$. The skewness begins to increase as the solar insolation maximizes, but returns to values near $Sk_w = -0.40$.

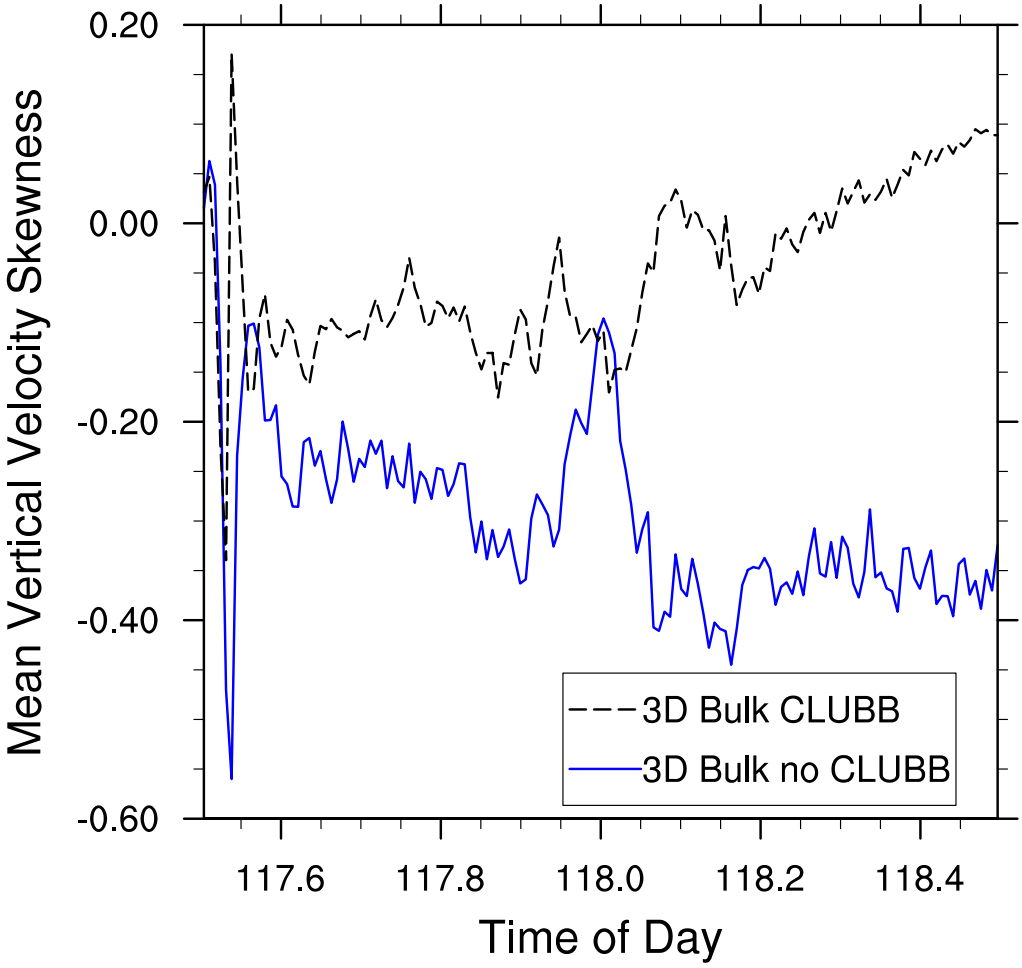


Figure 4.6: The domain-mean vertical velocity skewness in the 3D domain plotted as a function of simulated time for bulk microphysics without CLUBB (blue) and bulk microphysics with CLUBB (black).

Figures 4.7 and 4.8 show the TKE and subgrid-scale TKE, respectively, produced in the AMPS cloud simulations with and without CLUBB. In the cloud produced without CLUBB, the TKE increases with height to a maximum at the cloud top height level near

1 kilometer. The subgrid-scale TKE also increases with height to 1 kilometer. There is no predicted subgrid-scale TKE above the cloud top. However, above the cloud top height at 1 kilometer, the resolved TKE quickly decreases in magnitude showing energy is dissipated as heat into the the atmosphere above 1 kilometer. This signals the simulated cloud is driven by longwave cooling, and the temperature inversion is formed from the energy dissipation at the cloud top. In the cloud produced with CLUBB, the maximum value of the resolved TKE at cloud top height near 1 kilometer is about 25% less than the maximum resolved TKE value. The amount of TKE that is vertically advected above the cloud top is less when CLUBB is used than when it is not. This explains why the temperature inversion in the CLUBB cloud is not as large as the no-CLUBB inversion. The magnitude of the unresolved, subgrid-scale TKE with CLUBB in Figure 4.8 is also smaller than the no-CLUBB cloud.

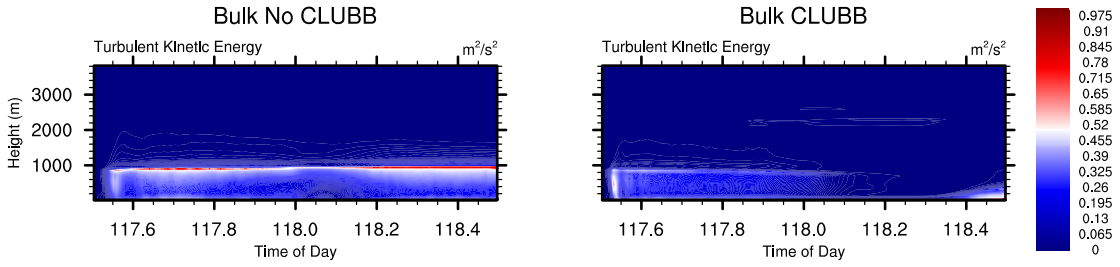


Figure 4.7: The turbulent kinetic energy ($m^2/s^2$) in the 3D domain plotted as a function of simulated time for bulk microphysics without CLUBB (left) and bulk microphysics with CLUBB (right).

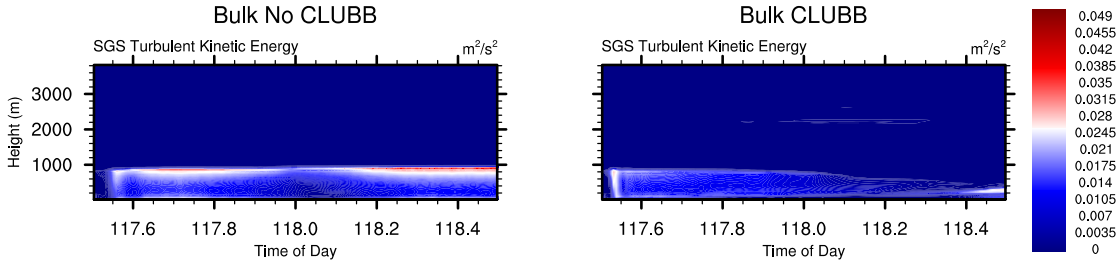


Figure 4.8: The subgrid-scale turbulent kinetic energy ($m^2/s^2$) in the 3D domain plotted as a function of simulated time for bulk microphysics without CLUBB (left) and bulk microphysics with CLUBB (right).

In summary, the sign of the vertical velocity skewness indicated the magnitudes of the resolved and unresolved TKE were not as large in the cloud produced with CLUBB compared with the simulation of the cloud produced without CLUBB. This is explained in the differences in the dissipation rate. The turbulent energy and the unresolved, modeled variables are functions of a dissipation parameter. This dissipation rate parameter is inversely proportional to a chosen length scale - mixing length, which is a function of the grid spacing. In CLUBB, the length scale is one-quarter of the size of the 1.5-TKE length scale. With a smaller length scale, the dissipation rates in CLUBB are larger, resulting in smaller values of TKE.

### 4.8.2 Results with CLUBB and without CLUBB using the Bin Microphysics

The Spectral Bin Microphysics without (left panels) and with (right panels) CLUBB are shown in Figure 4.9. The SBM microphysics with CLUBB shown in Figure 4.9 does not show the same effect with using CLUBB as the bulk does. The SBM is not coupled to the CLUBB the same way the bulk is. In the bulk scheme with CLUBB, the hydrometeors are scaled by a cloud fraction value, and hole-filling routine is applied for positive-assuredness. This scaling is not applied in the SBM with CLUBB. Therefore, there is less interaction with CLUBB and with the cloud species within the SBM microphysics parameterization.

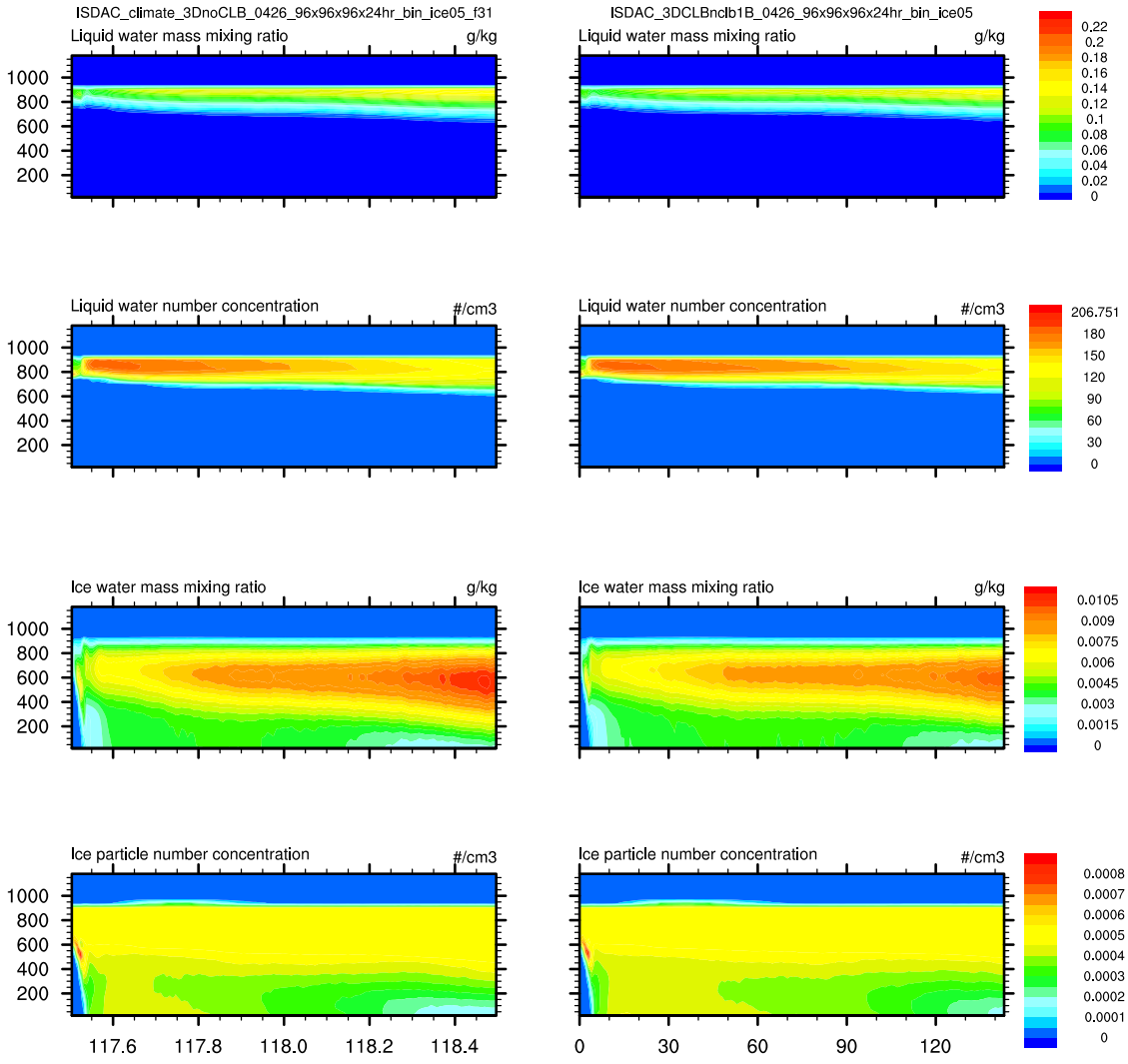


Figure 4.9: Evolution of the averaged cloud profiles of liquid and ice masses and concentration from the SAM without CLUBB (left) and SAM-CLUBB (right) with SBM microphysics from the 24 hour simulation period.

### 4.8.3 Differences in Two and Three Dimensions

Due to the computational expense of a cloud-solving LES with increasingly complex parameterizations, the dimensional configuration of the model domain was explored as a possible means to achieve accurate AMPS cloud simulations in a less time-intensive manner. The change to the cloud macrophysical and microphysical properties are negligible when the dimensionality is reduced from 3D to Two-Dimensions (2D). Figure 4.10 shows

the cloud produced with bulk microphysics and 1.5-TKE. The 3D plots have smoother features due to the increased number of grid points that have been averaged. The magnitudes of the liquid and ice hydrometeors are comparable between the 2D and 3D. Figure 4.11 shows the effect on the cloud when the dimensionality is change with CLUBB. The liquid layer continues to be depleted.

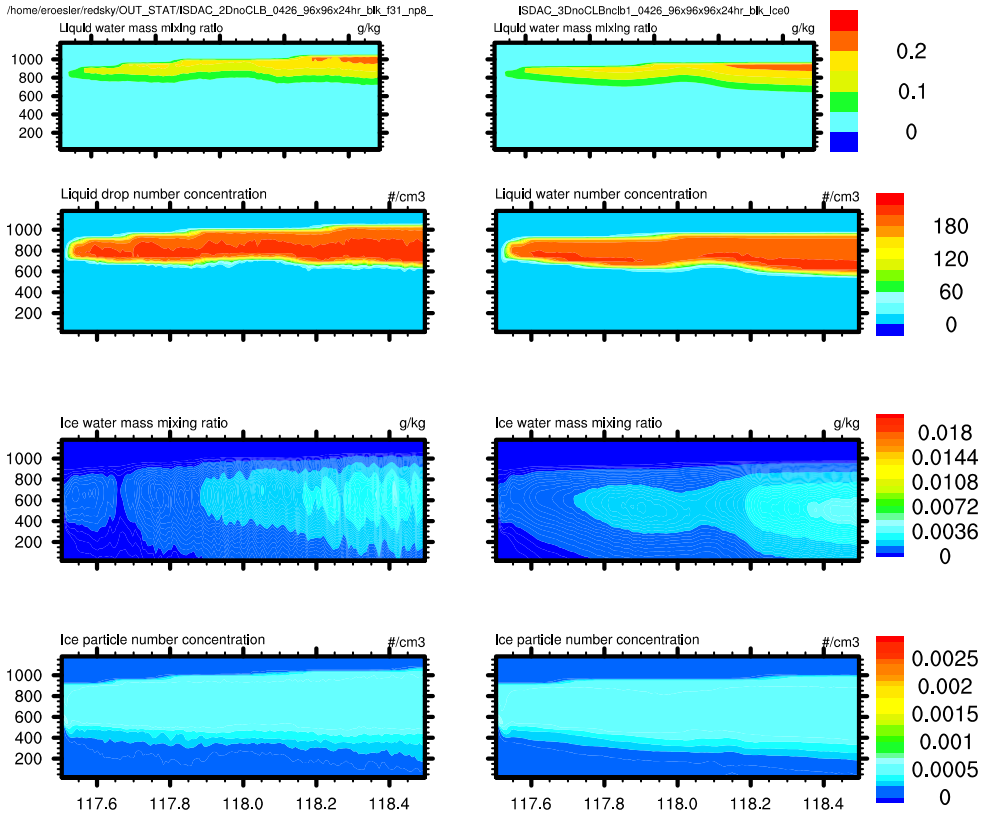


Figure 4.10: Domain-averaged profiles with respect to time for the 2D bulk without CLUBB (left) and 3D bulk without CLUBB (right) model configurations. Sets of four contour plots are shown for each cloud. The top plot in each set is the cloud liquid mass mixing ratio, followed by the cloud liquid number concentration, the ice mass mixing ratio, and the ice number concentration at the bottom of each set of contoured plot.

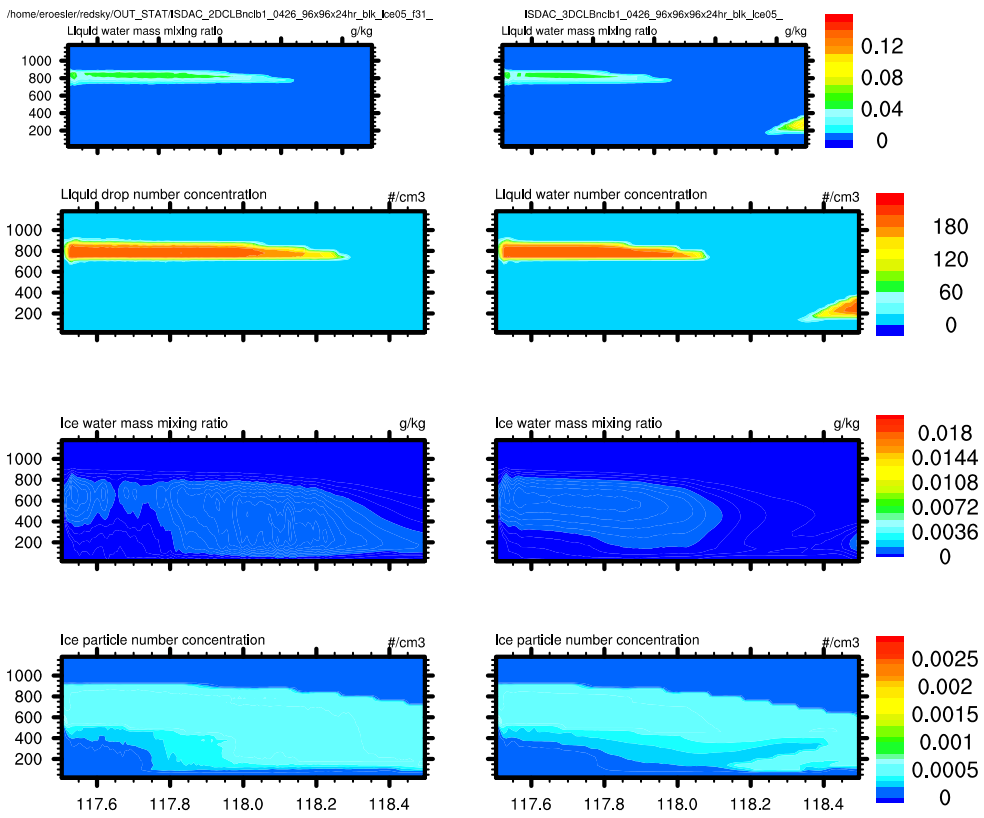


Figure 4.11: Domain-averaged profiles with respect to time for the 2D bulk with CLUBB (left) and 3D bulk with CLUBB (right) model configurations. Sets of four contour plots are shown for each cloud. The top plot in each set is the cloud liquid mass mixing ratio, followed by the cloud liquid number concentration, the ice mass mixing ratio, and the ice number concentration at the bottom of each set of contoured plot.

### 4.8.4 Sensitivity tests 1.5-TKE, and CLUBB to changes in the horizontal grids

Sensitivity test were executed with the bulk microphysics in 2D with and without CLUBB with increasing horizontal grid spacing. Figure 4.12 shows the use of CLUBB compared to without CLUBB for the $\Delta x$ equal to 100 m, 2 km, and 10 km. CLUBB looks more suited to be used in larger horizontal grid boxes.

The variability of $w$ is much less in CLUBB. CLUBB is meant for larger grid boxes, where dissipation occurs. At $\Delta x = 0.1$ km, the cloud begins to dissipate. The liquid layer begins to decrease, slowly. At $\Delta x = 2$ km, the cloud produced appeared to be in the most steady-state condition. At $\Delta x = 10$ km, the cloud decayed but overall depth didn't decrease

that much. The cloud didn't die. With no CLUBB at this same grid resolution, the cloud top keeps growing without regard to size of domain.

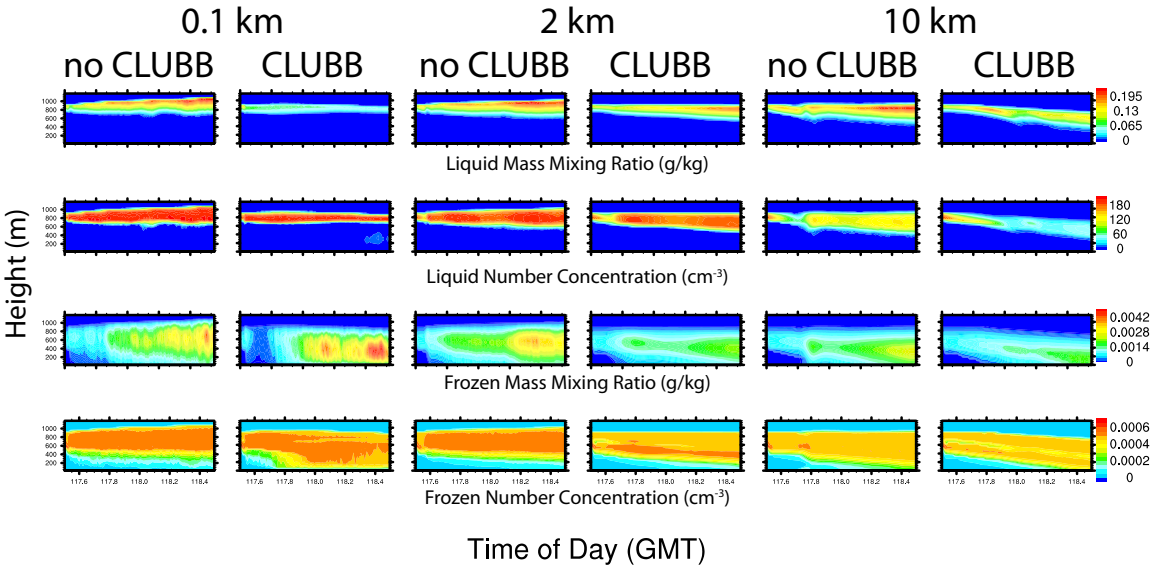


Figure 4.12: Simulations using bulk microphysics with and without CLUBB for increasing horizontal grid spacing for $\Delta x$ equal to 100 m, 2 km, and 10 km.

### 4.8.5 Sensitivity Tests with No Subgrid-Scale Turbulence

Figure 4.13 below shows cloud motion with subgrid-scale turned off, and characteristics of that cloud and CLUBB cloud are similar: tendency for liquid layer to decrease and a lack of liquid depletes ice. Turbulent mixing within the cloud replenishes the droplet population. So even at these resolutions, it is seen that the subgrid-scale model's purpose is to predict motion, turbulence, and how buoyant parcels are accelerating upwards. The magnitude of the vertical velocity values predicted by CLUBB need to be greater. CLUBB is either too dissipative, or CLUBB is not active enough.

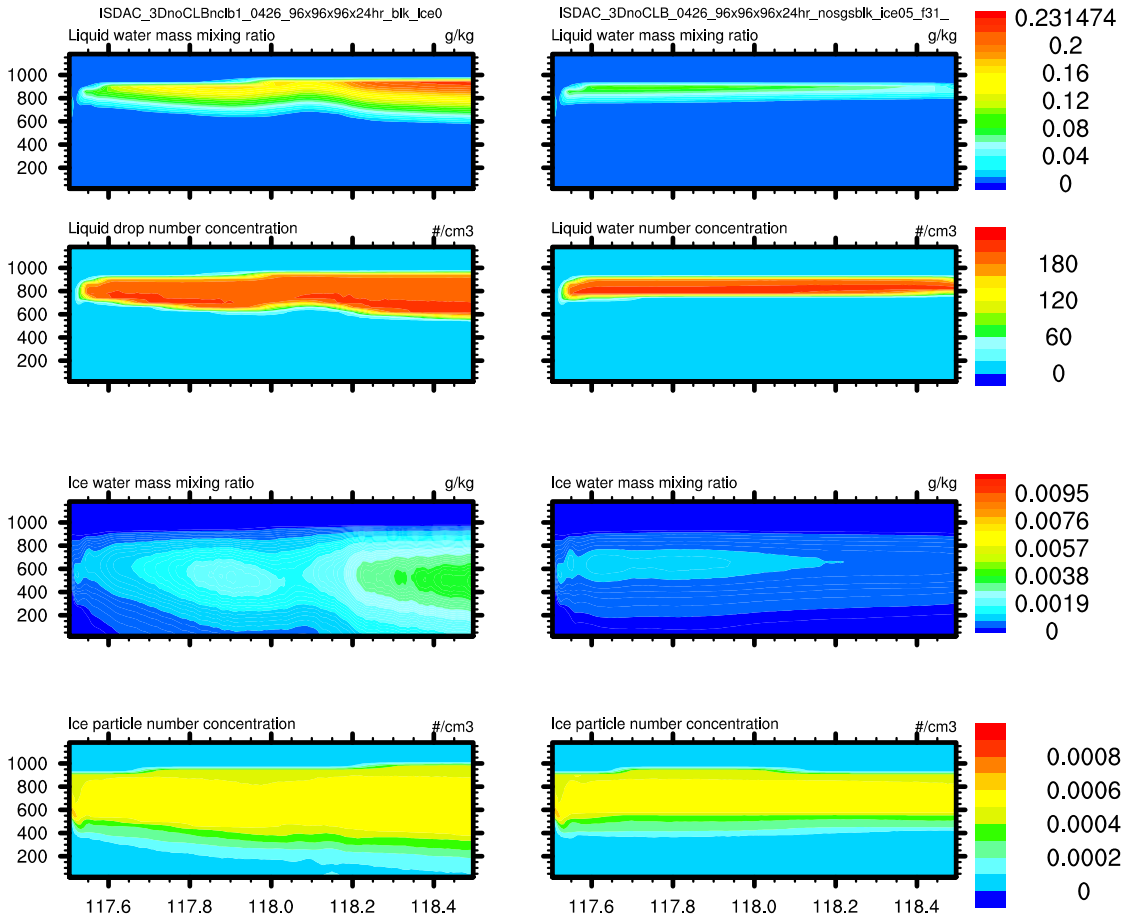


Figure 4.13: Simulations using bulk microphysics with the 1.5-TKE scheme (left panels) and without using a subgrid-scale turbulence scheme (right panels).

### 4.8.6 Sensitivity Tests with CLUBB and the Time Step

Even when using the CLUBB parameterization, the subgrid scale turbulent kinetic energy uses the *Deardorff* (1980a) closure for the first order terms. CLUBB predicts higher-order moments, which provide new information to the mean flow. We seek a way to test the influence of CLUBB without altering its internal tuning parameters and established customizations with SAM and the bulk microphysics. Sensitivity tests were performed with the bulk CLUBB simulations by increasing the time between dynamical time steps that CLUBB was called. Figure 4.14 shows the clouds produced by decreasing the usage of CLUBB 5×, 10×, and 20×, or every 10 s, 20 s, and 40 s, respectively. Generally, as

the frequency of CLUBB usage increases, the amount of ice and liquid contained in the cloud decreases. Less change is seen between the clouds that are called at $5\times$, $10\times$, and $20\times$ the original frequency. A strikingly large change occurs at $5\times$. The cloud is maintained, and a liquid layer prevails for the 24 hour simulation period. Although the cloud exists for this time period, if the simulation was carried forward another day, the cloud top would decrease, the liquid layer would dissipate, and there would be an AMPS cloud death. Essentially, using CLUBB more frequently has the affect of causing cloud death more quickly. The depth of the liquid layer is larger for a longer period of time as CLUBB is called less often. The cloud death here is related to the cloud top height. All the CLUBB clouds have a step-like decreasing pattern approximately every 5 hours which corresponds to the level spacing in the model's vertical resolution. For this AMPS cloud, CLUBB is causing the cloud top height to decrease by a 40 m approximately every 5 hours.

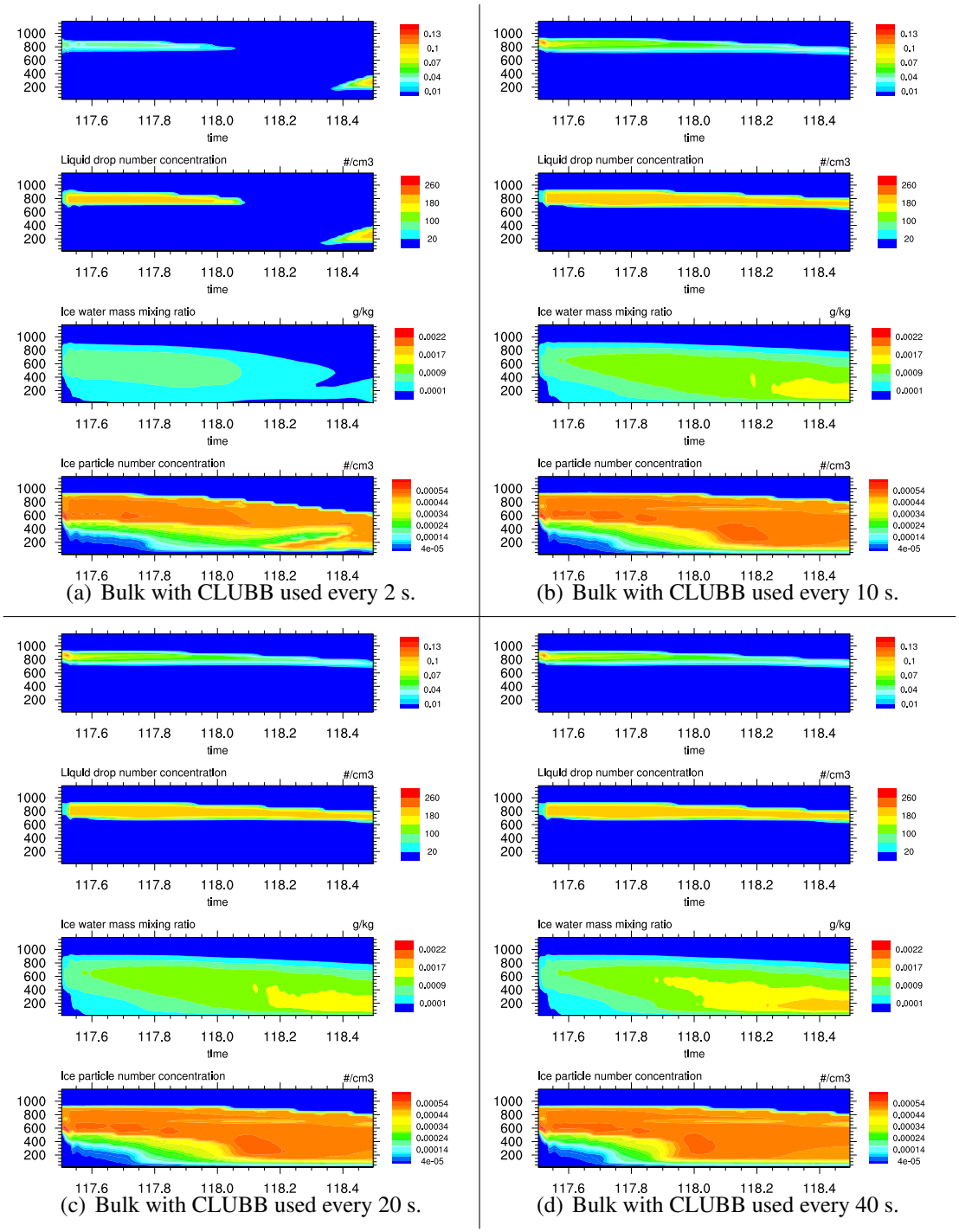


(a) Bulk with CLUBB used every 2 s.

(b) Bulk with CLUBB used every 10 s.

(c) Bulk with CLUBB used every 20 s.

(d) Bulk with CLUBB used every 40 s.

Figure 4.14: Domain-averaged profiles with respect to time for the 3D bulk with CLUBB configuration. Sets of four contour plots are shown for each cloud. The top plot in each set is the cloud liquid mass mixing ratio, followed by the cloud liquid number concentration, the ice mass mixing ratio, and the ice number concentration at the bottom of each set of contoured plot. The plots show CLUBB being used with less frequency. Plot (a) is the baseline cloud also shown in Figure 4.2 where CLUBB is used every dynamic time step, (b) is the uses CLUBB every fifth dynamic time step or every 10 simulated seconds, (c) uses CLUBB every 20 seconds, and (d) uses CLUBB every 40 seconds.

### 4.8.7 Comparison with Observations

Profiles of the averaged liquid and frozen mass concentrations and number concentrations from the SAM simulations are compared with averaged ISDAC flight 31 measurements in Figures 4.15, 4.16, 4.17, and 4.18. Both 2D and 3D results are shown with the bulk and SBM microphysics with and without CLUBB. As with the SBM and bulk comparison in Chapter III, the average liquid mass and number concentrations achieve a closer match to the averaged observations than the frozen mass and number concentrations in every model configuration.

The 3D bulk microphysics with and without CLUBB shown in Figure 4.15 reflects the contour plots previously shown. The liquid water mass mixing ratio is under predicted compared to the observations. The development of a second maximum at 200 meters reflects the low condensed material above the surface at 118.4 UTC. The ice number concentration over predicts the observations, and the mass concentration is an order of magnitude less than the observed.

Although the 2D bulk microphysics with and without CLUBB shown in Figure 4.16 falls within the first and second standard deviations of the measurement values, time means are not always indicative of model performance. Recall that in Figure 4.11, the 2D cloud with CLUBB did not exist for 24 hours. The second maximum at 200 m is missing here, reflecting what was presented in the Figure 4.11. The overall patterns of the liquid and ice hydrometeors show little change in changing dimensionality, however the cloud top height increases, and the ice number concentration sedimentation increases.

The 3D SBM microphysics with and without CLUBB is shown in Figure 4.17, and the 2D configuration is shown in Figure 4.18. The cloud profiles from the 3D configuration fall within the measurement's variability. The modeled ice mass mixing ratio is also similar to the measured ice mass mixing ratio, but the mass is under predicted from 800 m downwards. The ice number concentration is over-predicted. There is not much difference between the no CLUBB and CLUBB, and the profiles mostly overlay each other. This is

due to the independent operation of the two parameterizations, SBM and CLUBB, within SAM. The ice number concentration with the CLUBB is 0.00005 $cm^{-3}$ greater from the surface to 200 m. The reason for this difference is attributed to CLUBB's internal hole-filling and positive assuredness routines for the liquid and vapor, which indirectly affects ice values. The top of the liquid layer in the 2D is greater than the observations, and the base of the the liquid layer is shifted upwards also. The same relationship between no CLUBB and with CLUBB in 2D and 3D is seen. The ice number concentration is greater over a larger depth with CLUBB, from the surface to 600 m.

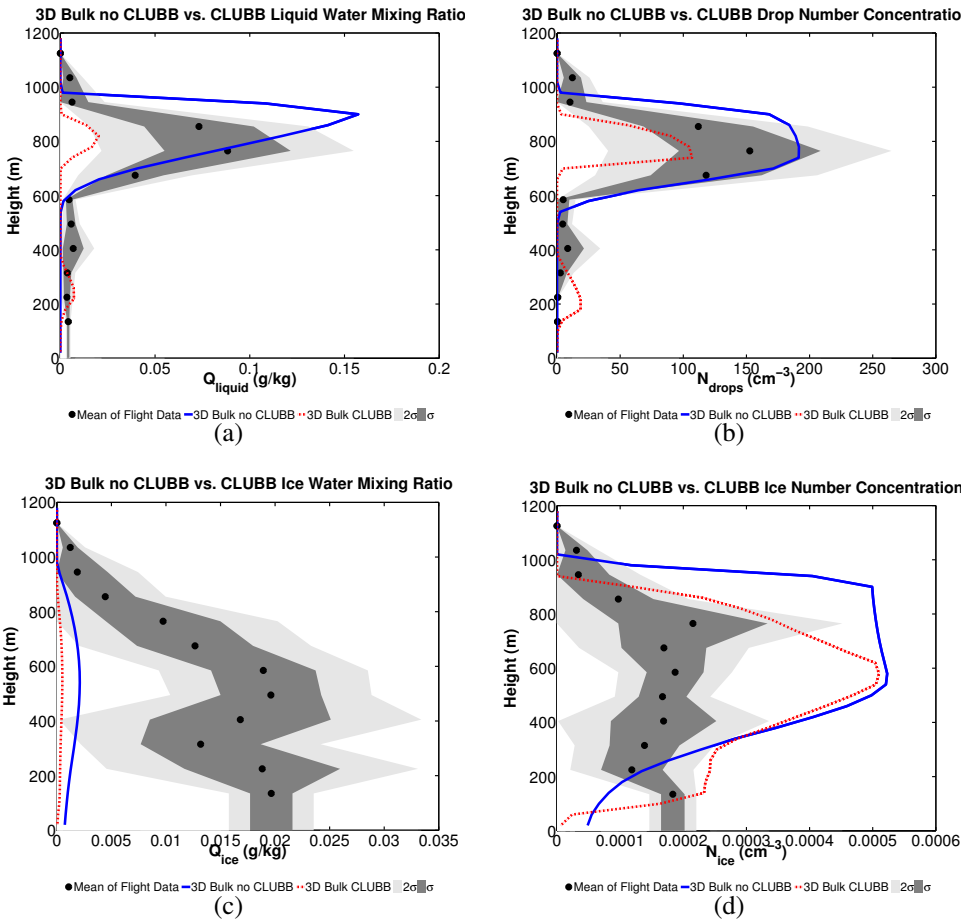


Figure 4.15: Cloud profiles from the bulk without CLUBB (blue lines) and with CLUBB (red lines). These plots are the average from the 3D-domain and 24-hour simulation period. The black dots are mean values from the measurements taken by the aircraft in the cloud on 26 April 2008. The light grey shading is two-times the standard deviation from the mean, and the darker grey shading is the standard deviation from the mean of the in situ measurements. Shown are total masses and number concentrations of the liquid and frozen hydrometeors. (a) Total liquid mass mixing ratio (g/kg), (b) Total liquid number concentration ($cm^{-3}$), (c) Total frozen mass mixing ratio (g/kg), and (d) total ice number concentration ($cm^{-3}$).

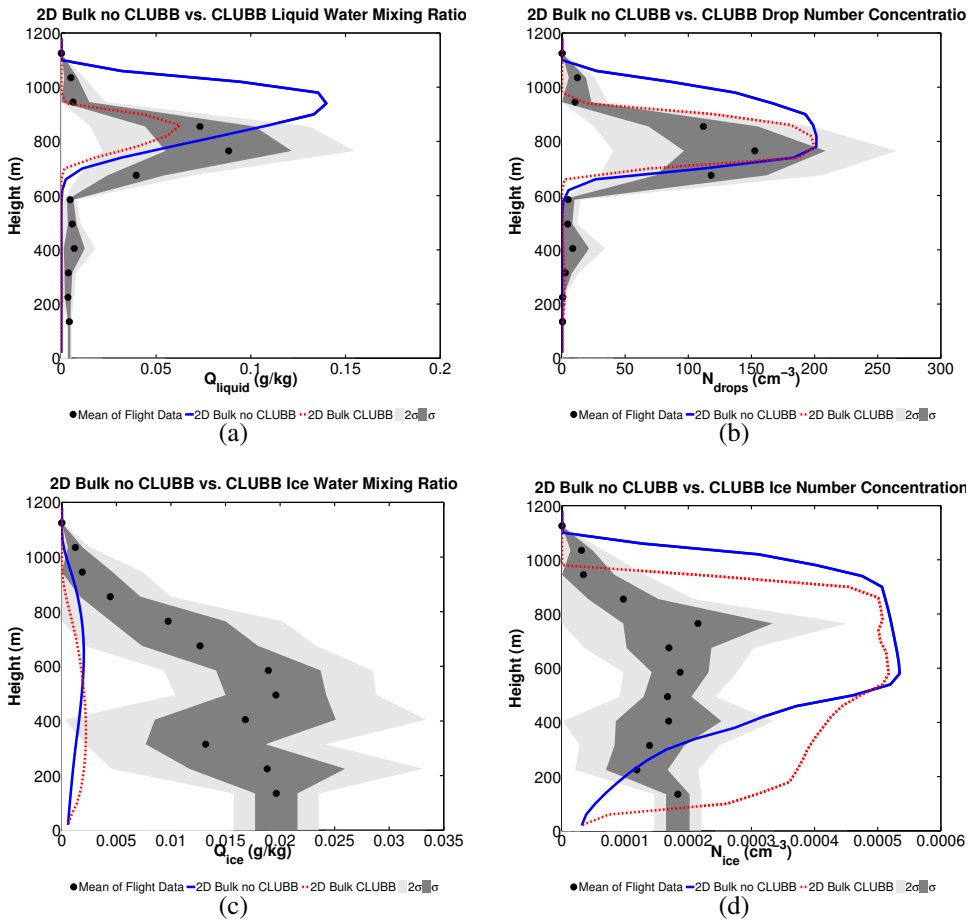


Figure 4.16: Cloud profiles from the bulk without CLUBB (blue lines) and with CLUBB (red lines). These plots are the average from the 2D-domain and 24-hour simulation period. The black dots are mean values from the measurements taken by the aircraft in the cloud on 26 April 2008. The light grey shading is two-times the standard deviation from the mean, and the darker grey shading is the standard deviation from the mean of the in situ measurements. Shown are total masses and number concentrations of the liquid and frozen hydrometeors. (a) Total liquid mass mixing ratio (g/kg), (b) Total liquid number concentration ($cm^{-3}$), (c) Total frozen mass mixing ratio (g/kg), and (d) total ice number concentration ($cm^{-3}$).

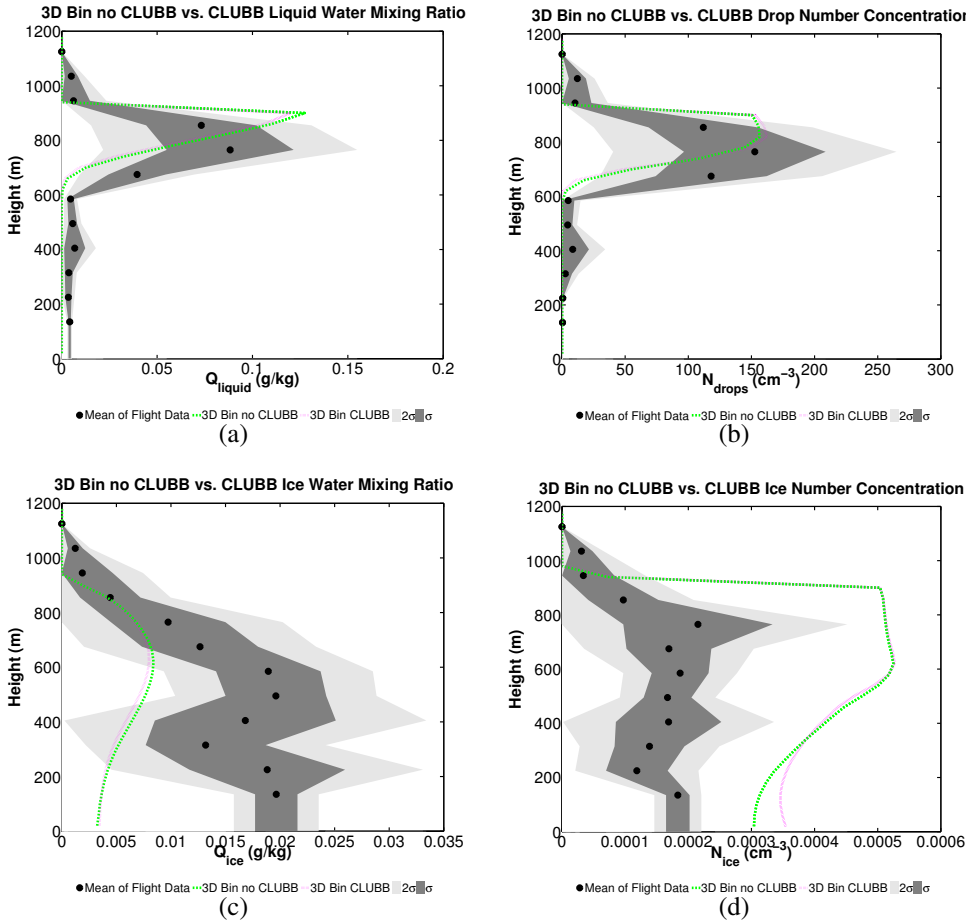


Figure 4.17: Cloud profiles from the SBM microphysics without CLUBB (green lines) and with CLUBB (red lines). These plots are the average from the 3D-domain and 24-hour simulation period. The black dots are mean values from the measurements taken by the aircraft in the cloud on 26 April 2008. The light grey shading is two-times the standard deviation from the mean, and the darker grey shading is the standard deviation from the mean of the in situ measurements. Shown are total masses and number concentrations of the liquid and frozen hydrometeors. (a) Total liquid mass mixing ratio (g/kg), (b) Total liquid number concentration ($cm^{-3}$), (c) Total frozen mass mixing ratio (g/kg), and (d) total ice number concentration ($cm^{-3}$).

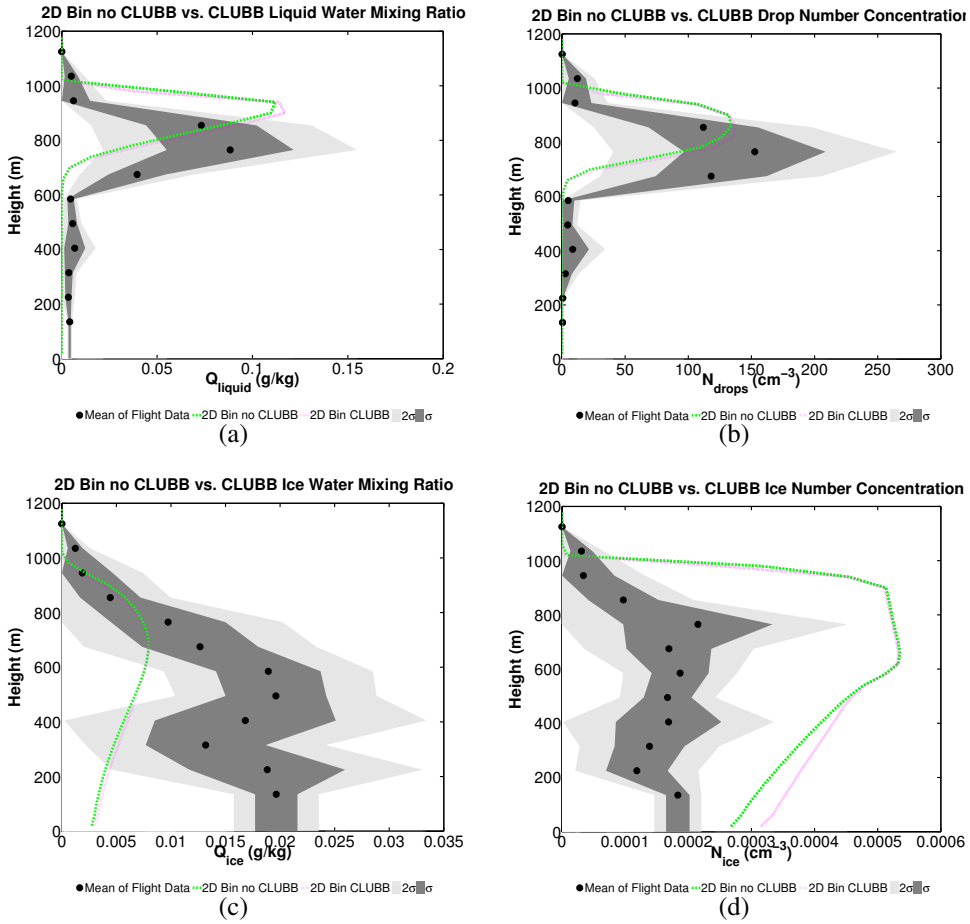


Figure 4.18: Cloud profiles from the SBM microphysics without CLUBB (green lines) and with CLUBB (red lines). These plots are the average from the 2D-domain and 24-hour simulation period. The black dots are mean values from the measurements taken by the aircraft in the cloud on 26 April 2008. The light grey shading is two-times the standard deviation from the mean, and the darker grey shading is the standard deviation from the mean of the in situ measurements. Shown are total masses and number concentrations of the liquid and frozen hydrometeors. (a) Total liquid mass mixing ratio (g/kg), (b) Total liquid number concentration ($cm^{-3}$), (c) Total frozen mass mixing ratio (g/kg), and (d) total ice number concentration ($cm^{-3}$).

## 4.9 Discussion and Summary

CLUBB's trademark ability is to provide a unified subgrid scale closure for a many cloud types. The closure method used by CLUBB has been tuned to observations to match a variety of cloud schemes (*Golaz et al.*, 2002), so re-adjusting parameters within

CLUBB for this specific case would defeat CLUBB's purpose of being a unified **subgrid-scale!** (**subgrid-scale!**) turbulent closure scheme. Similar to what was found in the results presented here, *Golaz et al.* (2002) used CLUBB in a one-dimensional model to simulate a variety of cloud types including a nocturnal stratocumulus. The cloud statistics produced by CLUBB in *Golaz et al.* (2002)'s simulations were found to be less well-mixed with smaller entrainment rates, cloud fraction values, and an underestimated cloud base and top compared to a 1.5-TKE closure scheme. The inversion was also more smooth with a lower starting height. Essentially, the cloud microphysical values that were predicted by CLUBB were found to be systematically low when compared to a 1.5-TKE closure scheme in that study. The conclusions reached by *Golaz et al.* (2002)are similar to the 3D and 2D AMPS clouds produced by CLUBB and the bulk microphysics in this research.

A solution to CLUBB's cloud representation shortcomings were made by applying it to the cloud less frequently to see the effect it would have on the inversion and liquid cloud layer. This was found to only delay the effect that CLUBB has on the evolution of the cloud. There should be another way to increase the mixing through the second and third order moments of vertical velocity, $\overline{w'^2}$ and $\overline{w'^3}$. The scaling of the microphysics by the cloud fraction and the absence of ice in CLUBB are concerning. These could be topics of future research.

It was concluded that for CRM-type simulations at these grid spacings for an AMPS the subgrid-scale turbulence is resolved well-enough to not need CLUBB. As the grid spacing increases and the subgrid-scale turbulence is not represented, CLUBB is needed to parameterize the energy-transfer between the largest resolved structures in the fluid and the dissipative scale. This would be on the order of at least a kilometer-sized grid spacing. For simulating AMPS with grid spacings of 10 km, the use of CLUBB shows a steady-state cloud is not maintained.

# CHAPTER V

# Summary of Microphysics and Turbulence Parameterizations

## 5.1 Comparisons of the Microphysics and the Turbulence Parameterizations

A summary is given on the impact of the different microphysics and subgrid scale turbulence packages on simulating the Arctic Mixed-Phase Stratocumulus (AMPS). The four parameterizations can be compared directly with each other. Figure 5.1 shows the Three-Dimensions (3D) System for Atmospheric Modeling, v6.8.2 (SAM) model results with bulk-noCloud Layers Unified By Binormals (CLUBB), Spectral Bin Microphysics (SBM)-noCLUBB, bulk-CLUBB, and SBM-CLUBB for the domain mean profiles of liquid and ice mass and concentrations in time.

These are all idealized, steady-state simulations of a cloud, and the state-of-the art SBM model produced the steady-state solution. The SBM cloud top and cloud depth did not change by more than 5%, which amounts to approximately one model level of $\Delta z =$ 40m, regardless of the configuration used (Two-Dimensions (2D), 3D, and SBM-CLUBB).

The bulk microphysics scheme is well regarded and has been shown to be robust under many cloud types and environments. However, changes in the turbulence closure package significantly altered the cloud. The CLUBB's activity within the bulk microphysics is more

invasive than in the SBM. It was found that changing the subgrid scale turbulence package has more of an influence on the macrophysical properties of the cloud (i.e., cloud lifetime and extent) than changing the microphysics packages.

## 5.2 Comparisons with known properties of Arctic Mixed-Phase Clouds

The decrease in water vapor at cloud top can cause a potentially unstable inversion as in a subtropical single layer stratocumulus (*Deardorff*, 1980b; *Randall*, 1980; *Solomon et al.*, 2011). When the vertical gradient of equivalent potential temperature, $\theta_e$, is positive, the boundary layer is stable, inhibiting vertical mixing and cloud formation. The equivalent potential temperature is given by

$$\theta_e = \left(T + \frac{L_v}{c_p} q_v\right) \left(\frac{p_0}{p}\right)^{\frac{R_d}{c_p}}, \tag{5.1}$$

where $T$ is the temperature of the air at a pressure $p$, $p$ is the pressure of the air in mbar, $p_0$ is the standard reference pressure equal to 1000 mbar, $L_v$ is a constant called the latent heat of evaporation in (kJ/(kg K), $c_p$ is the specific heat capacity of dry air at constant pressure equal to 1004 J/(kg K), and $R_d$ is the specific gas constant for air equal to 287 J/(kg K). Equation 6.8 shows $\theta_e$ is proportional to the water vapor mixing ratio, and an increasing $q_v$ with heightcan create a stable layer preventing cloud development or ensuring cloud death. The rate of the water vapor mixing ratio decreasing in height creates a positive $\theta_e$ vertical gradient, $\partial\theta_e/\partial z > 0$. The atmosphere would be stable but unfavorable for clouds.

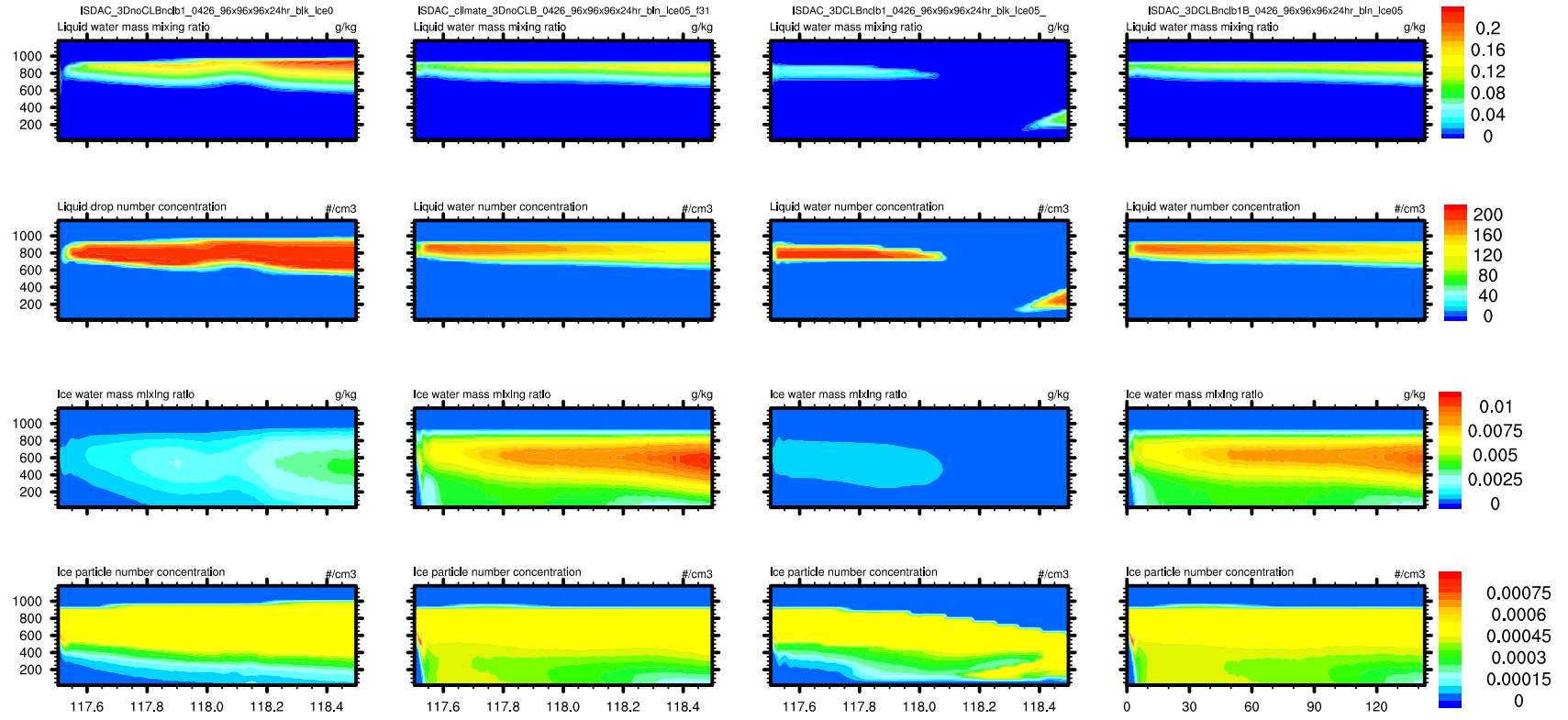


Figure 5.1: Evolution of the averaged cloud profiles of liquid and ice masses and concentration from the 3D SAM (left-to-right) bulk-noCLUBB, bin-noCLUBB, bulk-CLUBB, and bin-CLUBB during the 24 hour simulation period.

# CHAPTER VI

# Death of an Arctic Mixed-Phase Stratocumulus Cloud

## 6.1 Introduction

The reasons behind the persistence of Arctic Mixed-Phase Stratocumulus is an open scientific question. The co-location of liquid and ice for several days in the stratocumuli suggest many other processes including radiative, turbulent, microphysical, and environmental aspects of the cloud work in concert to maintain its structure. For instance, *Harrington et al.* (1999) found stability of transition season mixed-phased cloud is dependent upon temperature, ice concentration, habit of ice crystals, and most strongly the concentration of ice nuclei (IN). *Fan et al.* (2009a) investigates ice nuclei recycling and ice nucleation pathways as mechanisms to maintain the cloud. *Ovchinnikov et al.* (2011) links microphysical properties to cloud dynamics and stability. *Solomon et al.* (2011) looks at moisture budgets and buoyancy to understand the cloud persistence. *Morrison et al.* (2012) reviews the various mechanisms and pathways that have been previously studied to explain the persistence of the Arctic Mixed-Phase Stratocumulus (AMPS). They argue that the difference between having a clear Arctic sky and cloud cover is related to changes in the large-scale environment. Detailed observations and measurements of the clouds have begun to be compiled as interest is directed at knowing the sensitivity of the Arctic sea ice to large-scale changes. The near-impossible task of having a statistically significant number of clouds in a variety of states to inform models that could make projections of the future atmospheric state

would require observations for many decades. Assuming the knowledge is needed in the near time-frame, we turn to cloud resolving models to be the surrogate for reality and test proposed changes in the environment to assess the effect on AMPS.

The number and range of dynamic, thermodynamic, and microphysical variables that change from a clear Arctic sky to a cloudy Arctic sky are large. Examination of the sensitivity of model output to changes in these variables is typically performed by varying one at a time, holding the others constant. The one variable's value would be changed incrementally. All the values of the variable would be tested in the numerical model. After a single variable's range was simulated, another variable's range would be tested the same way while all other variables would be held constant. Using the state-of-the-art Spectral Bin Microphysics (SBM) microphysics in a 3D domain for one of those sensitivity analysis simulations would take a very long time to produce results and show the sensitivity of of the cloud to a changing environment. In order to perform the sensitivity analysis, a less expensive model is necessary. It is necessary to assume that changes made to the modeled cloud environment and the effect on the AMPS would be reflective of a real-world change to the cloud in the same changes to the environment. Thus, the model configuration should show good agreement between the modeled and measured microphysical structure of the cloud. From the different model configurations presented in the previous chapters, the bulk microphysics without Cloud Layers Unified By Binormals (CLUBB) in 2D would be a good model configuration to use in an AMPS sensitivity analysis because it can model the cloud in the quickest amount of time with the highest fidelity.

To test the large parameter space that influences the persistence of a mixed phase cloud, we turn to engineering optimization algorithms that can quickly absorb tens of variables that need thousands of increments of change. The idealogical problem to solve is a failure mode problem: under which environmental conditions does the AMPS die?

### 6.1.1 DAKOTA and Latin Hypercube Sampling

A freely available software package, Design Analysis Kit for Optimization and Terascale Applications (DAKOTA), supported by Sandia National Laboratories, can direct this parameter study. DAKOTA has numerous capabilities including optimization tests, uncertainty quantification, and sensitivity analysis (*Adams et al.*, 2009). DAKOTA has been used for parameter and error estimation in other geophysical models. *Larour et al.* (2012) estimated error propagation from inputs to outputs in a sea ice model. *Peterson et al.* (2010) performed a sensitivity analysis (SA) on a set of ten dynamic and thermodynamic variables common to a pair of sea ice models that were being compared. DAKOTA is used in this study is to quantify the sensitivity of the cloud to changes in the environmental variable.

There are a variety of SA analysis techniques that can be used to explore a variable space. Here, the Latin-Hypercube Sample (LHS) technique will be used. An example of LHS for a variable range is shown in Figure 6.1 Consider two input variables, $x_1$ and $x_2$, that have ranges of $[0, 1]$. In this example of LHS, four unique values, or four segments, are chosen to be used from each of the variables. These segments do not have to be equally spaced within the variable range but are for this research and in this example. It is also assumed the variables are not independently varying, so because there are two variables and four values from each of the variables will be used, then the model will need to be executed $2^4$ times for each of the variable input values. One can see that if executing the model is computationally expensive, the number of variables increases, or the number of segments in the variables' range increases, then the total number of model executions increases exponentially. The technique of LHS can be applied to this example because it is an efficient way to explore a large parameter space and reduce the number of model executions.

To implement LHS, first identify the variables and their ranges, then choose how and in what way the variable ranges should be partitioned. Finally, one cell is randomly selected from the matrix of rows and columns that comprise the variables' ranges, as in Figure

6.1. A value within that cell is chosen, and then the row and column that the cell exists is eliminated from the remaining space to be sampled again. The remaining space is sampled with another random cell chosen, then a value within that the cell is assigned, and then the row and column from the coordinates of the second cell is eliminated from the remainder of the space. This process is repeated until each row and each column has only one value. This is seen in Figure 6.1. The variable range of $x_1$ and $x_2$ is partitioned into four equal segments, then each row and column has one value represented by the black dots.

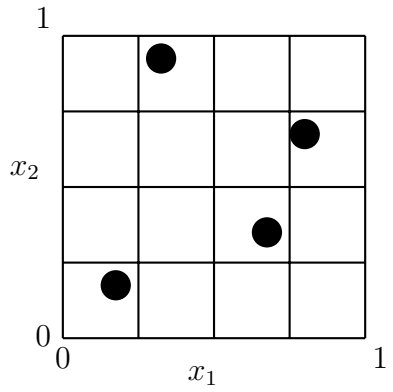


Figure 6.1: Two-variable, four-segment example of Latin Hypercube Sampling

## 6.2 Experiment design

Similar to the example of LHS previously described, the DAKOTA's technique of LHS was used to test the sensitivity of the AMPS cloud to changes in its environment with System for Atmospheric Modeling, v6.8.2 (SAM). Eleven variables comprising initial and boundary conditions describing the AMPS's environment were selected to perturb and initialize SAM. Table 6.2 has the ranges and initial points for these variables that were used in this LHS study. The initial point values listed in Table 6.2 are the values used in the baseline simulations. (The baseline simulation results are the results of SAM's AMPS in Chapters III and IV with the bulk microphysics, 1.5-Turbulent Kinetic Energy (TKE) turbulence parameterization, Two-Dimensions (2D) with 100 m horizontal grid spacing.) The first set of LHS simulations used parameter ranges that were within $\pm 10\%$ of the initial

point values. Following the $\pm 10\%$ perturbation study, a broader range of parameter values was used. The minimum and maximum values for the full range LHS parameter study are also listed in Table 6.2.

The parameter ranges for the $\pm 10\%$ and the full range need to be partitioned into segments. To do this, it was assumed that the environment in which the AMPS forms is ill-behaved and will transition abruptly from a state containing a mixed-phase stratocumulus cloud to a state without a cloud. This assumption prompts the use of many partitions so that the variables ranges will be highly-sampled and the results from SAM can show the cloud's sensitivities. The number of model executions needed to explore this space is $2^N$, where $N$ is the number of variables, or $2^{11} = 2048$. Because of the way the LHS technique samples the parameter space, the total number of partitions will equal the number of model executions, 2048. The partitions were chosen to be equally spaced.

### 6.2.1 Variable Explanations

The following explanations are given for why each of the variables was chosen and its range.

- **Initial ice concentration ($N_{ice}$)** Measurements and observations of mean in-cloud and below-cloud ice crystal concentrations have varied largely between 0-20 $L^{-1}$ (*de Boer et al.*, 2009; *McFarquhar et al.*, 2007, 2011). Part of this large variation has been attributed to observational and retrieval uncertainties, biases, and errors. In situ measurements are prone to ice crystal shattering and selectively sample certain particle size ranges (*McFarquhar et al.*, 2011). Uncertainty in observations stems from assumptions in the ice crystal size distribution in lidar-radar retrievals (*de Boer et al.*, 2009). Modeling studies investigating the sensitivity of ice concentration on the macro physical properties of the AMPS generally constrained the ice concentration to a much smaller range (*Morrison et al.*, 2011; *Ovchinnikov et al.*, 2011). Rapid glaciation resulted from $N_{ice}$ concentrations a fourth of the range used here.

- **Coarse mode aerosol concentration ($N_a$)** *Feingold et al.* (1999) and *Yin et al.* (2000) performed numerical studies of stratocumulus and convective clouds, respectively. Both found that the addition of large aerosols quickened the onset of precipitation in clouds with high levels of background aerosol. In clouds with low background aerosol, the addition of large aerosols did not significantly change cloud precipitation. *Feingold et al.* (1999) tested in the influence of increased coarse mode aerosols in a warm cloud while *Yin et al.* (2000) allowed for the mixed-phase in a convective cloud. This parameter is tested to see if AMPS behave in a consistent way as convective clouds and warm, drizzling stratocumulus clouds to increases in coarse mode aerosols. The occurrence of Arctic Haze and the increasing human activity in the North Slope of Alaska (NSA) region motivated using this parameter in this study to possibly contribute to the need to have a global cloud knowledge of aerosol-cloud interactions. The ranges used in Table 6.2 are if no coarse mode aerosols were present (minimum value) to the measured value of 8.5 $cm^{-3}$ on 26 April 2008 (see Table 2.1) to the maximum value of 100 $cm^{-3}$ occurring in a polluted winter airmass (*Barrie*, 1986). The number concentrations and size of the particles are slightly higher than concentrations observed during Mixed-Phase Arctic Clouds Experiment (MPACE) and used in a model intercomparison study (*Klein et al.*, 2009). Thus the minimum range will step towards the clean Arctic environment observed during the fall transition season.

- **Surface properties** The surface under an AMPS varies in location and season. During the melting transition month of April, the statistics of the sea surface temperature, sensible heat flux, latent heat flux, and surface momentum flux are given in Table 6.1. The sensible and latent heat fluxes are negatively correlated with sea surface temperature. The variable ranges used in the LHS study encompass the observed ranges of the surface parameters in April.

Table 6.1: Statistics of surface properties observed at the NSA facility in Barrow, Alaska, during the April 2008 ISDAC intensive observation period. Values were derived from ECMWF reanalysis and soundings for the purpose of being used in SAM (*M. Ovchinnikov, personal communication*).

| | SST | SHF$_sfc$ | LHF$_{sfc}$ | $\tau_{sfc}$ |
|---|---|---|---|---|
| Minimum | 253 | -35.0 | -17.7 | 0 |
| Average | 262 | 4.20 | 7.89 | 0 |
| Maximum | 275 | 40.6 | 32.0 | 0 |

– **Sea surface temperature (**$SST$**)** The Arctic Ocean's surface layer water temperature is near-freezing year around. The minimum and maximum $SST$ temperature range were set to lie just outside the $\pm$ 10% perturbation values or at $\pm$ 30°K from the initial value. The minimum and maximum values in the $\pm$ 10% perturbation LHS study are outside the outside the realistic range of temperatures found in the Beaufort Sea. The maximum and the 110% value from the initial point are near-tropical sea surface temperatures. These values were kept, although unrealistic, for consistency between this and the other parameter values in the $\pm$ 10% and full range LHS studies.

– **Surface sensible heat flux (SHF**$_{sfc}$**)** In the spring when the Arctic Ocean is still mostly covered by sea ice, heat sources from the warm ocean beneath are minimal (*Pinto*, 1998; *Ovchinnikov et al.*, 2011). During ISDAC, it was observed that the surface sensible heat flux was between 0 W/m$^2$ and 10 W/m$^2$. In the fall when sea ice has retreated, the heat flux from the ocean is on the order of 100 W/m$^2$, which is comparable to the heat flux responsible for the formation of lower-latitude marine stratocumulus. This condition was observed during MPACE (*Xie et al.*, 2006). The formation of AMPS in spring and fall is different, and testing the range of this variable might reveal the coupling behavior of the cloud to the boundary layer. The maximum values have been used in Cloud Resolving Model (CRM) studies of AMPS observed during MPACE (*Luo et al.*, 2008).

– **Surface latent heat flux (LHF$_{sfc}$)** The LHF follows from the same analysis and studies given for the SHF. The LHF from the surface will increase with more exposed ocean. The SHF and LHF are calculated from the ECMWF analysis described in Chapter II. These values are used in the model SAM throughout the simulation.

– **Surface roughness** ($\tau_{sfc}$) This parameter is considered surface roughness in SAM, but a more common name for this is the surface momentum flux. With increasing positive values, it decreases the magnitude of the horizontal winds at the surface. *Tremblay and Mysak* (1997) performed a sensitivity study with an sea-ice model that varied $\tau_{sfc}$ and found that the modeled sea ice properties better match observations when this parameter was varied over the Arctic sea ice. Their study comments on the range of values used in sea ice modeling studies and the effect on sea ice movement. Here, we look at the effect of a slightly larger range of $\tau_{sfc}$ on surface wind values as they affect AMPS. Equations 6.1 and 6.2 show how the $\tau_{sfc}$ affects the $u$ and $v$ wind fields at the surface where $\Delta z$ is the vertical grid spacing and $u_0$ and $v_0$ are the mean horizontal winds.

$$\left(\frac{\partial u}{\partial t}\right)_{sfc} = -\left(\frac{\tau_{sfc}}{\Delta z}\right)\frac{(u_0)_{sfc}}{\sqrt{(u_0)^2_{sfc}+(v_0)^2_{sfc}}} \tag{6.1}$$

$$\left(\frac{\partial v}{\partial t}\right)_{sfc} = -\left(\frac{\tau_{sfc}}{\Delta z}\right)\frac{(v_0)_{sfc}}{\sqrt{(u_0)^2_{sfc}+(v_0)^2_{sfc}}} \tag{6.2}$$

• **Slopes and Intercepts for the Profiles** The atmospheric profiles for wind, temperature, and humidity were shown to have much variation during ISDAC and at the NSAsite from the ECMWF analysis. Fitting polynomials to these profiles was investigated, but the variation of the coefficients of the polynomials from just the April

2008 month of ISDAC would have caused at least a $2^5$ increase in the number of SAM simulations. Only two days in this entire month contained atmospheric properties sufficient to support an AMPS. It was then decided that the profiles should be similar to the default values, giving a better chance in the LHS study to start the simulation with an AMPS. Because of the difficulty in constraining the ranges of the profile parameters, the values for the minima and maxima were rounded to create symmetric ranges from the initial point. The profiles of the baseline runs were fit to a discontinuous bilinear function. The dependent variable was pressure, $p$, starting with 1020 mbar at the surface decreasing to 765 mbar. The pressure levels were decreased by 10 mbar until 900 mbar. At 900 mbar the pressure levels were decreased by 5 mbar with the exclusion of at 895 mbar, the next pressure level was 885 mbar. These pressure stratifications developed the well-mixed homogeneous boundary layer in order to form the AMPS. The large-scale meridional wind component was set to be constant throughout, $u = -2.5(m/s)$. The longitudinal wind component was prescribed by

$$v = -0.002p + 17(m/s). \tag{6.3}$$

– **Slope of large scale vertical motion ($m_{w_{ls}}$)** The vertical wind component was set by

$$w_{ls} = m_{w_{ls}} p - 0.0431816(m/s). \tag{6.4}$$

If the initial point was used for $m_{w_{ls}}$, the average difference is 4% from the original vertical profile used.

– **Intercept of potential temperature ($b_\theta$)** If the pressure was greater than or equal to 905 mbar, then $\theta = b_\theta$. If the pressure was equal to 900 mbar, then $\theta = 269K$.

– **Slope of potential temperature ($m_\theta$)** For pressures, $p$, less than 905 mbar, the potential temperature was prescribed by

$$\theta = -m_\theta p + 314K. \tag{6.5}$$

– **Intercept of water vapor ($b_{q_v}$)** In situations of open water from leads or retreated sea ice, large heat fluxes will carry moisture upwards creating a moisture flux from the surface. Increasing the amount of water vapor available below cloud base can alter the cloud hydrometers by becoming entrained into the cloud through updrafts and increasing the total water content in the initial cloud formation. If the pressure was greater than or equal to 905 mbar, then $q_v = b_{q_v}$. If the pressure was equal to 900 mbar, then $q_v = 1K$.

– **Slope of water vapor ($m_{q_v}$)** A source of water vapor is necessary for the mixed-phase clouds that have sedimentation but still maintain the cloud. The parameter $b_{q_v}$ can encompass water vapor sources for the cloud base for clouds that are coupled with the boundary layer. For decoupled AMPS, *Solomon et al.* (2011) suggests water vapor is transported from above by turbulent fluxes. The slope of the water vapor profile can be changed to explore this cloud's sensitivity to cloud-top entrained water vapor. Thus, for pressures, $p$, less than 905 mbar, the water vapor profile was prescribed by

$$q_v = m_{q_v} p - 0.8(g/kg). \tag{6.6}$$

Table 6.2: SAM variables that and their ranges that were input to DAKOTA's LHS-generating routine. The initial point represents the baseline values used in the simulations of Chapters III and IV. The variables ranges between the 90% and 110% values from the initial points were used in the $\pm$ 10% perturbation study. The minimum and maximum values were used in a full variable range study. There are 11 variables total.

| Variable Name | Minimum Value | 90% of initial point | Initial point | 110% of Initial Point | Maximum Value |
|---|---|---|---|---|---|
| Initial ice concentration $N_{ice}$ ($L^{-1}$) | 0 | 0.45 | 0.5 | 0.55 | 20 |
| Coarse mode aerosol concentration $N_a$ ($cm^{-3}$) | 0 | 7.65 | 8.5 | 9.35 | 100 |
| Sea surface temperature $SST$ (K) | 233.15 | 236.83 | 263.15 | 289.46 | 293.15 |
| Surface sensible heat flux $SHF_{sfc}$ ($W/m^2$) | 0 | 0 | 0 | 1 | 150 |
| Surface latent heat flux $LHF_{sfc}$ ($W/m^2$) | 0 | 9 | 10 | 11 | 110 |
| Surface roughness $\tau_{sfc}$ ($m^2/s^2$) | 0 | 0 | 0 | 0.1 | 0.01 |
| Slope of large scale vertical motion $m_{w_{ls}}$ (m/s/mbar) | 0.000001 | 3.83E-05 | 4.25E-05 | 4.68E-05 | 0.0001 |
| Intercept of potential temperature $b_\theta$ (K) | 200 | 238 | 264 | 290 | 400 |
| Slope of potential temperature $m_\theta$ (K/mbar) | 0 | 0.045 | 0.05 | 0.055 | 0.5 |
| Intercept of water vapor $b_{q_v}$ (g/kg) | 0 | 1.17 | 1.3 | 1.43 | 4.5 |
| Slope of water vapor $m_{q_v}$ (g/kg/mbar) | -0.02 | 0.0018 | 0.002 | 0.0022 | 0.02 |

### 6.2.2 SAM-DAKOTA configuration

The model set-up for SAM was the same as described in Chapters III and Chapters IV. The simulations were first executed with the TKEsubgrid-scale turbulence scheme and the Morrison two-moment bulk microphysics in 2D with 96 grid points in the vertical and horizontal. The horizontal grid spacing was $\Delta$x = 100 m, and the vertical grid spacing was a uniform 40 m starting 20 m from the surface. The model was integrated forward in time for 24 hours with a $\Delta$t = 2 s. DAKOTA has several ways in which it can be coupled to a numerical model. From the experience in using SAM in 2D, Three-Dimensions (3D), and with bulk, SBM, and CLUBB, we found the optimal number of processors to produce the fastest simulations under this domain configuration was between 8 and 12. In this configuration, the simulation could take between 10 minutes and 24 hours to complete in 2D. It should be noted that all of the simulations are independent of each other, meaning that sets of simulations could be executed simultaneously. Thus, in order to best utilize multiple-core machines, we de-coupled DAKOTA from SAM by allowing DAKOTA only produce the initial SAM model parameters and put them into a file. Parallel executions of SAM would then read one of the parameter files to generate the cloud statistics. Figure 6.2 shows how DAKOTA is interfaced with SAM, and the DAKOTA input file is given in Appendix A.

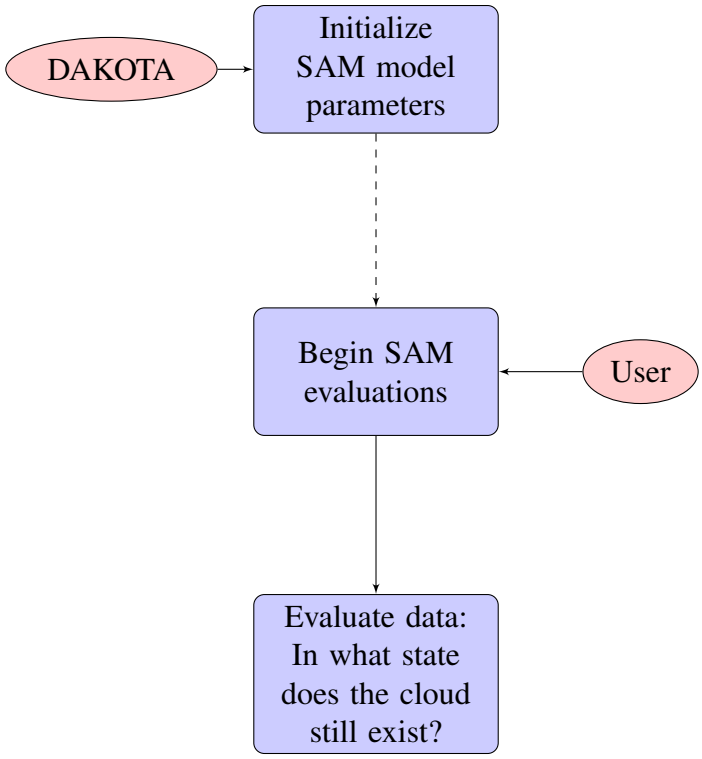


Figure 6.2: Logic chart for DAKOTA and SAM simulations. DAKOTA first produces the initial model parameters for SAM and writes each of the parameter sets into a file. Once that step is completed, the user then starts the SAM simulations. SAM reads the parameter values from the files produced by DAKOTA. After the SAM cloud simulation is complete, AMPS statistics can be generated from the results. The DAKOTA input file is given in Appendix A.

## 6.3 Results and Discussion

### 6.3.1 Time Evolution of Simulation Sets

The first set of results presented are from the $\pm$ 10% perturbation range to the initial point. Figure 6.3 shows the averaged domain cloud depth in time for all 2048 simulations. The cloud depth is calculated from the total water condensate, $q_t$, which is given by

$$q_t = q_i + q_s + q_h + q_g + q_r + q_d \tag{6.7}$$

where $q_i$, $q_s$, $q_h$, $q_g$, $q_r$, $q_d$ are the mass mixing ratios of ice, snow, hail, grapple, rain, and droplets, respectively. The cloud base and cloud top heights were defined when $q_t \geq 10^{-5}$ kg/kg. The cloud top minus the cloud base gave the cloud depth. The grey shaded region outlines the maximum and minimum cloud depth at any given time from any of the simulations. The colors of the lines have little meaning and are just used to show the variability within this set of simulations. It is interesting to note the strong similarities between every member of this set in this ensemble. There was very little variation in the spin-up period of time in the models. It was only after the first few hours of simulation time that the simulations began to diverge. Every simulation began to increase in cloud depth, just as the baseline simulations did. Just after 118.0 UTC, the cloud depth decreases and then increases to a final value between 300 and 400 m. The discrete steps in the cloud depth represent the changes in the cloud within a vertical model level of $\Delta z$ = 40 m.

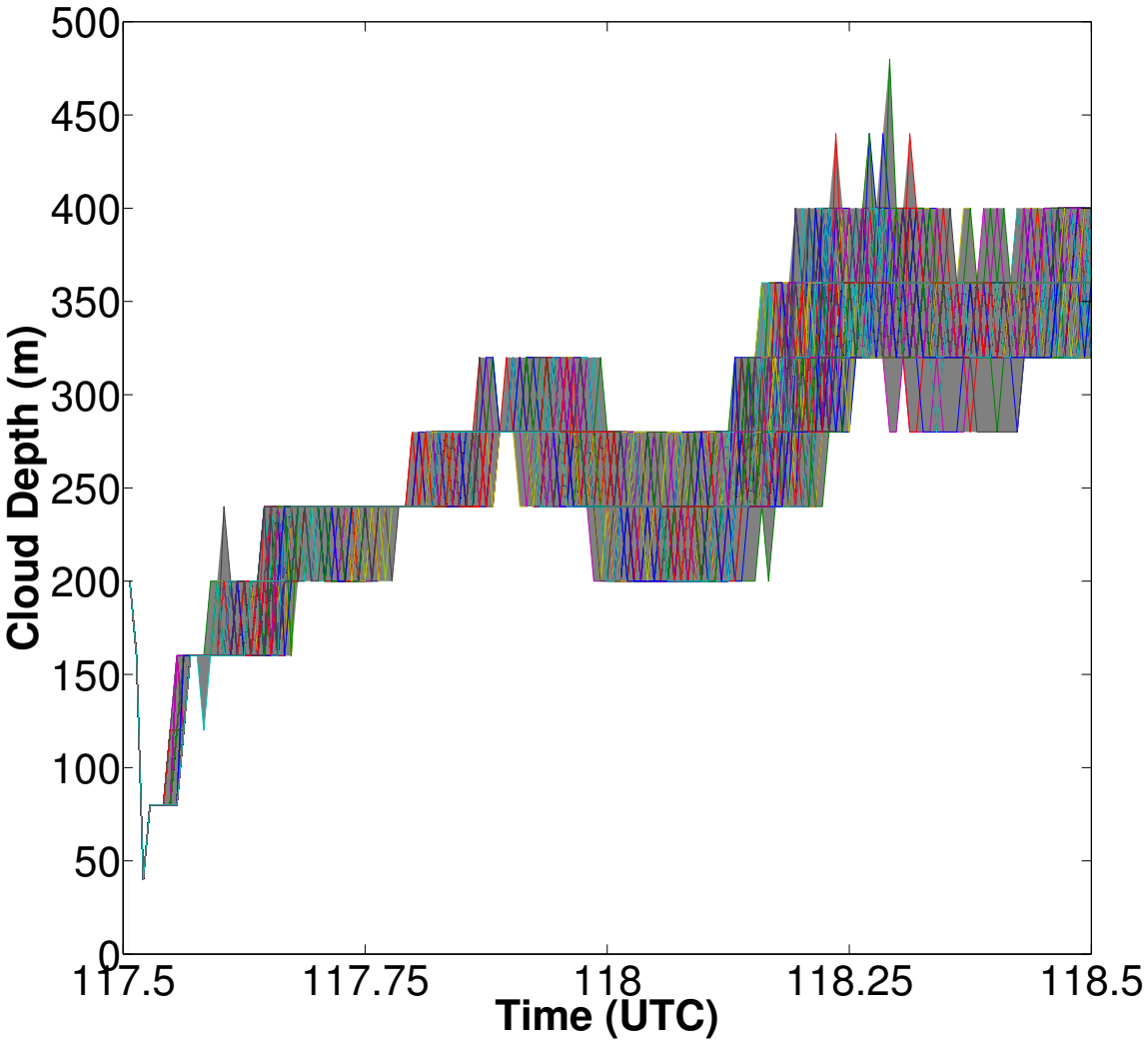


Figure 6.3: The time evolution of the cloud depth for the 2048 simulations where the variables were tested in a range $\pm 10\%$ of the initial values. Each run is represented by a colored line. However, the colors have been repeated in plotting this ensemble. For example, that means the color blue is repeated many times in this graph. The grey shading represents the absolute minimum and maximum at that time for the entire set of simulations.

Figure 6.4 shows the time evolution of the cloud depths for the full variable range. In contrast to the $\pm 10\%$ perturbation set, these results have a variety of cloud depths and evolutions, do not have many apparent similarities, and potentially develop into unphysical states. The grey shading again represents the minimum and maximum values of the cloud depth from all simulations at that time. From 0 m to 3800 m is shaded, meaning that cloud condensate extended the entire simulation domain from 20 m to 3820 m in at least one of the

2048 ensemble set. The colors have no meaning on the grouping of the simulations. From this graph, we anticipate there were few simulations that produced steady-state AMPS.

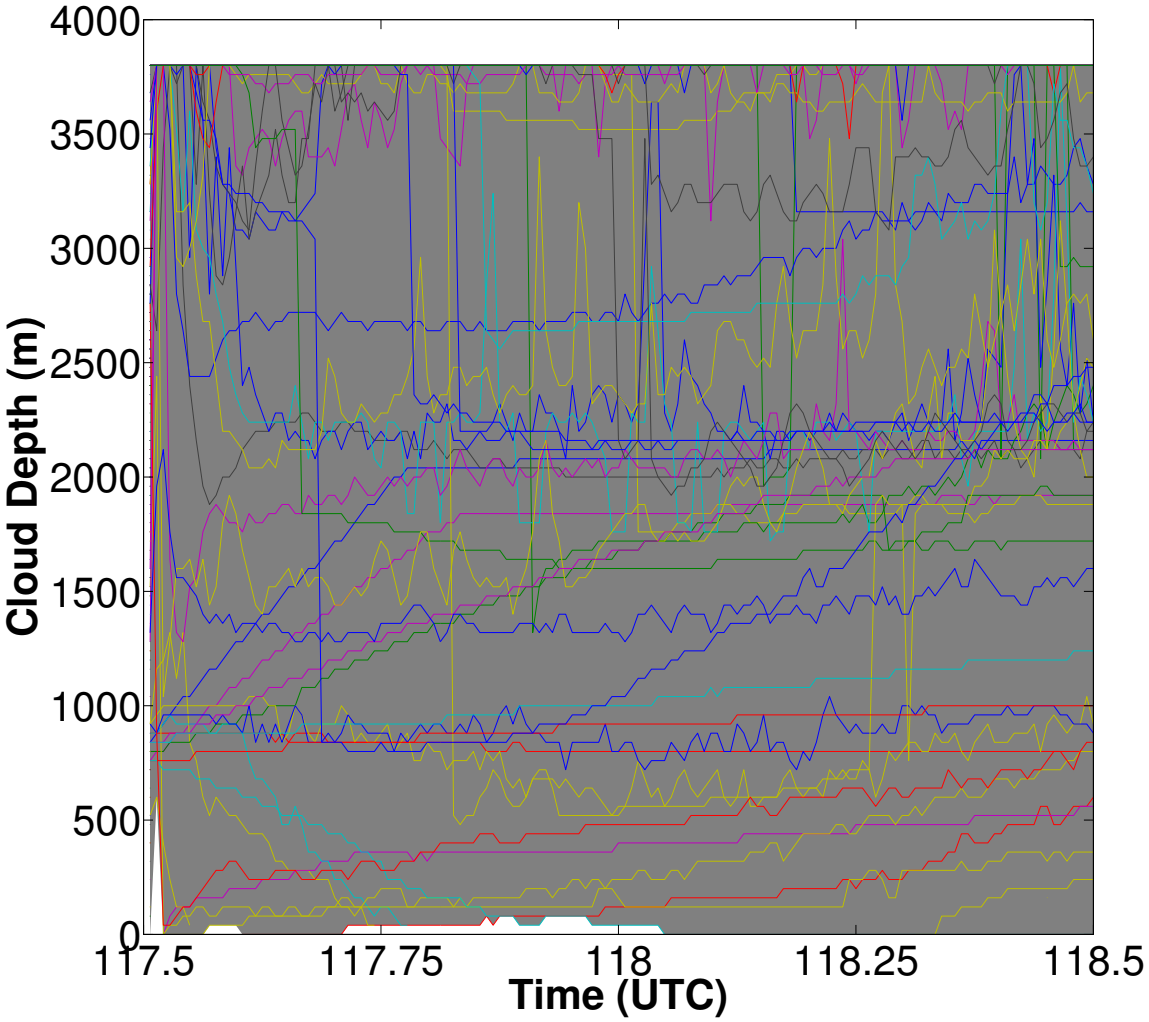


Figure 6.4: The time evolution of the cloud depth for the 2048 simulations where the variables were tested in the full range of values listed in Table 6.2. As in Figure 6.3, each run is represented by a colored line. However, the colors have been repeated in plotting this ensemble. For example, that means the color blue is repeated many times in this graph. The grey shading represents the absolute minimum and maximum at that time for the entire set of simulations.

### 6.3.2 Development of the Conditions of Cloud Evolution Groups

The deviation of each member from the ensemble mean in the $\pm 10\%$ perturbation range shown in Figure 6.3 does not suggest there will be much opportunity for isolating patterns

in the produced AMPS as a function of the perturbed variables. However, the results of the full variable range shown in Figure 6.4 needed to be grouped to ascertain any pattern or trend. Four states possible states of the cloud were considered: death, growth, decay, and stability. The well-behaved $\pm 10\%$ perturbation results can be used to guide the criteria for the groups because every simulation completed with a resolved cloud base, cloud top, and produced no unreal numbers.

Figure 6.5(a) shows the results of the total water condensate, $q_t$, of the first simulation from the SAM-DAKOTA LHS set of simulations. The input variable values for SAM produced by DAKOTA using the LHS scheme are ($N_{ice}$ = 12.5 $L^{-1}$, $N_a$ = 56.6 $cm^{-3}$, SST = 241 K, $SHF_{sfc}$ = 55.0 W/$m^2$, $LHF_{sfc}$ = 109 W/$m^2$, $\tau_{sfc}$ = 5.26$\times 10^{-3}$ $m^2/s^2$, $m_{w_{ls}}$ = 3.31$\times 10^{-5}$ m/s/mbar, $b_{theta}$ = 386 K, $m_{theta}$ =0.241 K/mbar, $b_{q_v}$0.55 g/kg, $m_{q_v}$ = 4.55$\times 10^{-3}$ g/kg/mbar), respectively. The simulated cloud has many characteristics seen in the simulations of AMPS in Chapters III and IV with the appearance of a nearly constant cloud base and cloud top over the 24 hour simulation period and a higher liquid mass concentration at the top of the cloud compared to the bottom. In the simulation from spin-up to the end, the cloud depth increases from 40 meters to 360 meters. Just over halfway into the simulation, at 118.0 UTC, the cloud depth begins to decrease. This characteristic cusp in the shape of the cloud at this time is seen in most SAM bulk simulations. The cloud base and cloud top are outlined in solid black lines. Figure 6.5(b) shows the cloud depth's evolution in time which is very characteristic of every cloud produced in this set as seen in Figure 6.3.

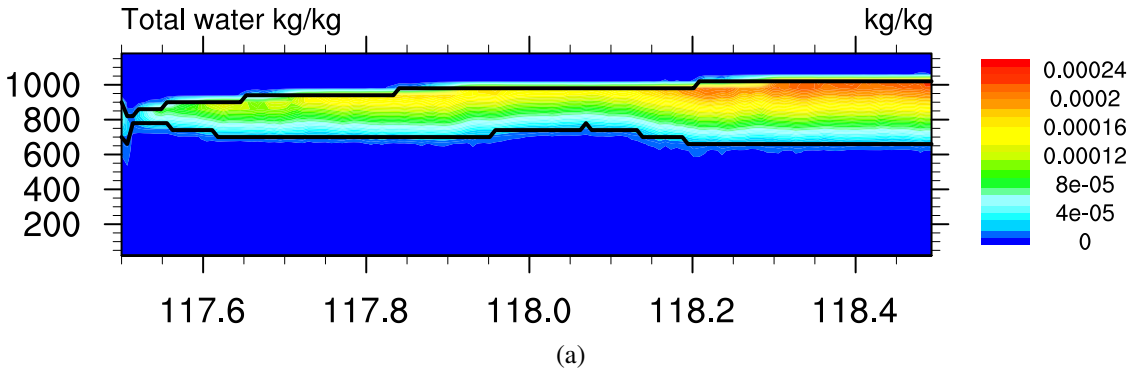


(a)

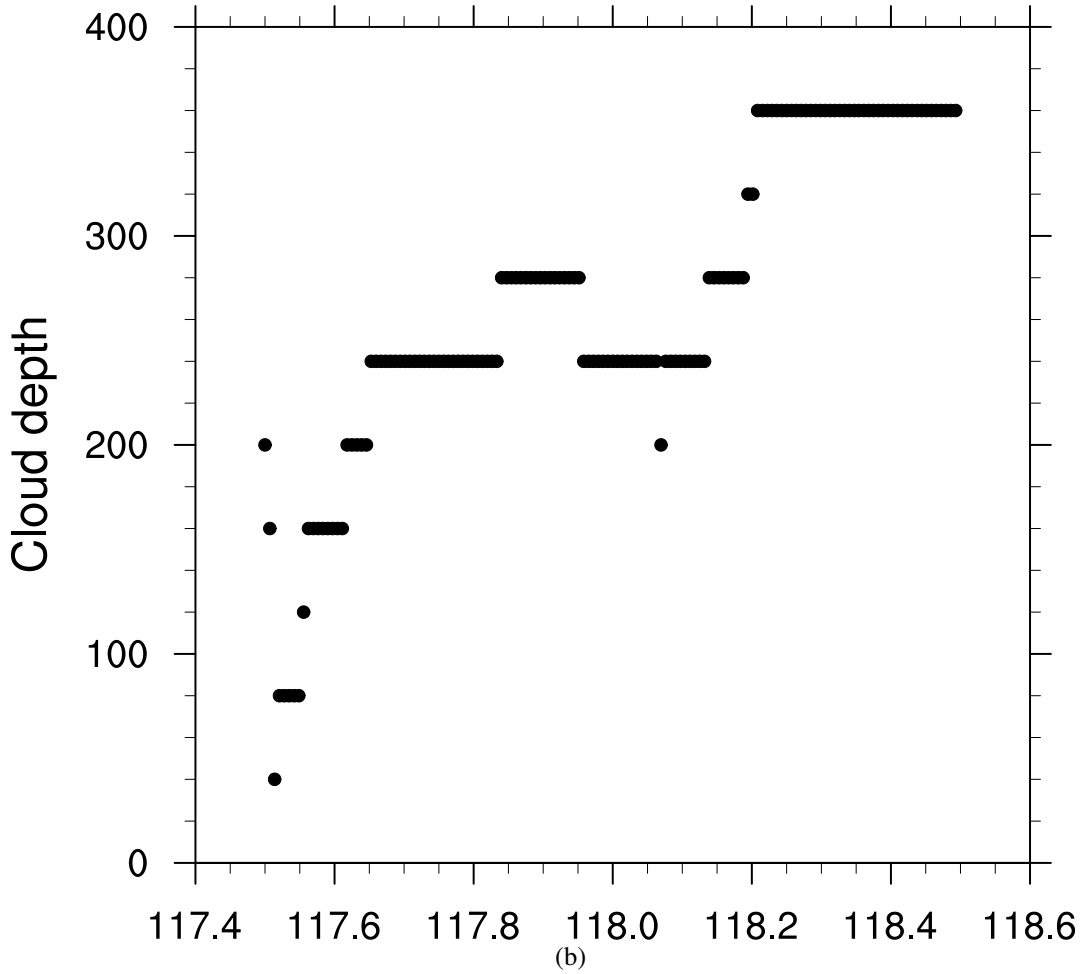


(b)

Figure 6.5: A single SAM simulation from the first set of parameters produced by DAKOTA. (a) Total water time-height plot of AMPS with the cloud top and cloud bottom outlined by the solid black lines defined where $q_t \geq 10^{-5}$ kg/kg. (b) The domain-main cloud depth in meters at every time step calculated from the difference of the cloud top and cloud base.

The cloud profile from the first simulation shown in Figure 6.5 has an increasing cloud depth with time. First, an average of the cloud depth was considered as a way to classify cloud evolution. Figure 6.6 shows the running mean (average of all previous points) and a variety of moving averages of the cloud depth. Even with these familiar results of the cloud profile shown here, the algorithm to group the data into the different cloud states would be overly complicated because none of the averages are monotonically increasing due to the cusp just past the $73^{rd}$ time step. Also, the cloud behavior in the first 2 hours, or until time step 13 in Figure 6.6, contains model-spin-up. It was concluded from Figure 6.6 that the difference between the cloud depth at the end of the simulation and the cloud depth at the start of the second hour of the simulation would be used to classify cloud growth or decay throughout the 24-hour time period. Finally, the use of cloud depth as the indicator for the AMPS state could be potentially difficult to validate in measurements. The cloud base measurement can be inaccurate to obtain (*de Boer et al.*, 2009). The cloud top height will be used instead of cloud depth to distinguish cloud death, decay, grown, or stability.

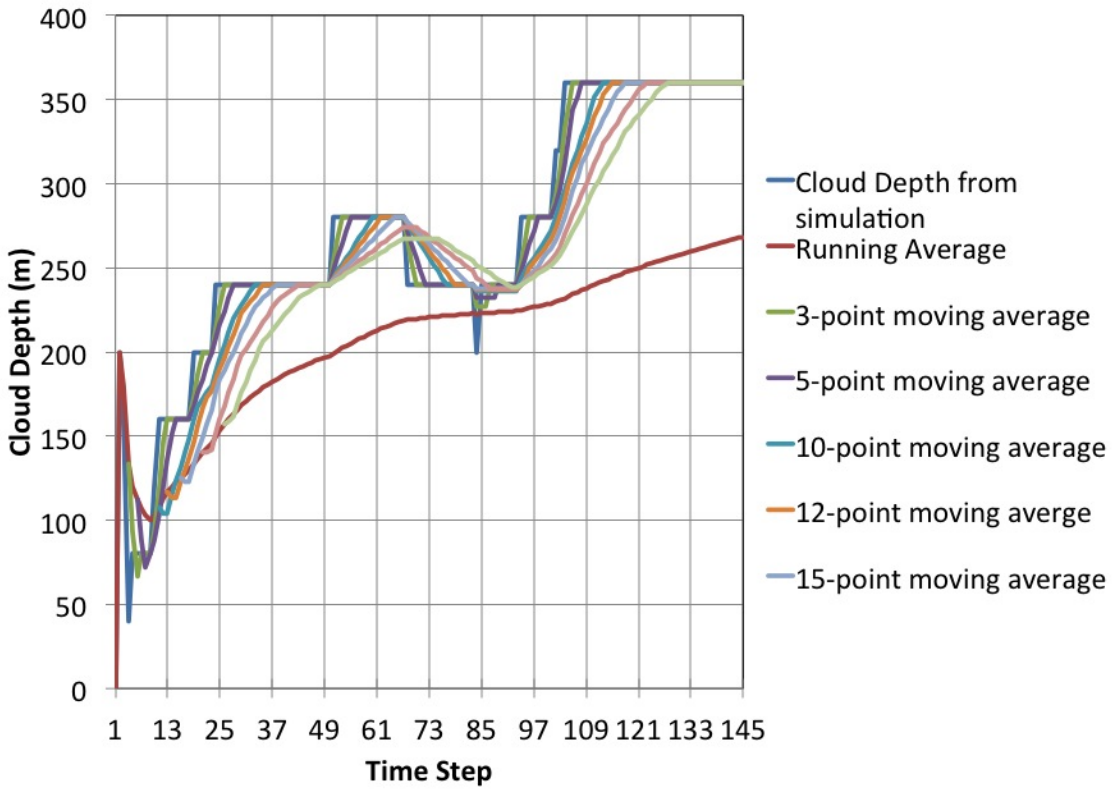


Figure 6.6: Plot of cloud depth from Figure 6.5 with the running mean (average of all previous points) and a 3-point, 5-point, 10-point, 12-point, and 15-point moving averages over the time steps from the simulation.

Thus the domain-mean cloud top, $\overline{c_{top}}(t)$ was defined at the height where $q_t \geq 10^{-5}$ kg/kg. Table 6.3 summarizes the the way the cloud results were grouped into four different cloud states. To elaborate, cloud stability was if the cloud top height at 118.5 UTC was approximately equal to the cloud top height at 117.58 UTC. The meaning of "approximately equal to" is given a $\pm$ 10% threshold where the cloud top height at 24 hours has to be within 10% of the cloud top height after 2 hours. The thresholds for this criteria are based on the cloud properties when the SBM parameterization was used. Recall from Chapter V that the cloud top and cloud depth did not change by more than 5%, which amounts to approximately one model level of $\Delta z = 40$m, regardless of the configuration used (2D, 3D, and SAM-CLUBB). These are all idealized, steady-state simulations of a cloud, and the state-of-the art SBM model produced the steady-state solution. Even thought SBM cloud

macrophysical heights did not change by more than 5%, we allowed a 10% threshold instead to reflect reality. That is, if a boundary layer cloud persisted for over 24 hours and changed the height or depth by just over 40 m, it would most likely be considered stable. The cloud was considered to be growing if the cloud top height at 24 hours was greater than the cloud top height at 2 hours. A similar condition was applied for cloud decay, only with a decrease in cloud top height between the two times.

Characterizing the cloud death was most troublesome to define than defining the other states. In doing an LHS study, the parameters generated can produce an unphysical situation which can cause model failure. Most of the results from the full variable range parameter study produced unphysical situations from which the environment in SAM could not recover. We wish to exclude these simulations from the cloud groups. In this set, there were many parameter sets from DAKOTA that caused model failure. We wish to isolate the model failures from the simulations that had a chance and made it all the way through and simulations that had successful starts but did not finish resulting in a cloud in one of the four states. We instated a condition that the cloud should exist for the first 2 simulated hours. The first two hours in previous simulations looks like model spin-up. The top of the cloud should be resolved as well. The model domain extends only 96 levels to 3640 m from the surface, and in many simulations the cloud depth exceeded the simulation's vertical domain. Those simulations were also excluded from analysis. Of the full range perturbation of variables ensemble set, 1880 runs produced unphysical results at some point during the 24 hours. There were 204 that had cloud top heights greater than the simulation domain. For requiring the that there be a cloud with a resolved cloud top 2 hours into the simulation, 1878 produced unphysical results, and 154 simulations had cloud at the 3820 m, leaving 16 simulations that could be classified into the cloud groups. Cloud death included several aspects. If the cloud depth was zero, then the cloud was classified as dead. There were no clouds from the full variable range that met his criteria. If the cloud existed at 2 hours but later became unphysical, those clouds were also considered dead.

Table 6.3: Summary of conditions of cloud evolution to group the results of the LHS perturbation results.

- **Cloud Stability** is if $\overline{c}_{top}(t = 24\,hr) \approx \overline{c}_{top}(t = 2\,hr)$.
- **Cloud Growth** is if $\overline{c}_{top}(t = 24\,hr) > \overline{c}_{top}(t = 2\,hr)$.
- **Cloud Decay** is if $\overline{c}_{top}(t = 24\,hr) < \overline{c}_{top}(t = 2\,hr)$.
- **Cloud Death** is if at any time $\overline{c}_{top} = 0$.

### 6.3.3 Dependence of Cloud Evolution on Variable Ranges

The conditions of Table 6.3 were applied to the clouds formed from the $\pm 10\%$ and full perturbed variable ranges to create the cloud groups. The average of the cloud top height was found during the time the cloud existed. The average cloud top height for every simulation plotted as a function of the the perturbed variable are in Figures 6.7(a) to 6.8(i). Figures 6.7(a) to 6.7(i) are of the $\pm$ 10% variable perturbation, and Figures 6.8(a) to 6.8(i) are of the full variable perturbation.

Every plot of the $\pm$ 10% study shows essentially zero correlation between the cloud top height and with any of the perturbed variables. The exception is the relationship of cloud top height to ice concentration in Figure 6.7(a). The mean cloud top height in this plot appears to decrease by at least a meter with a 0.1 $L^{-1}$ increase in ice concentration. For any given two cloud tops this relationship might not appear or even the sensitivity measured as a regression slope will always be less than the true sensitivity between any two points. The magnitude of the average of all the cloud top heights changing is not large compared to the cloud top changes in a single cloud and should be attributed to taking multiple averages which exclude, to a certain point, outliers. The large ensemble develops a clear trend. It has been found elsewhere that with high enough ice concentrations, the cloud begins to glaciate and precipitate away (*Ovchinnikov et al.*, 2011). Ice concentrations in this ensemble set did not exceed that threshold for these clouds, so no clouds were considered to be decaying or

be dead.

The cloud state classification was applied from Table 6.3. All 2048 AMPS had an increasing cloud top height with time. The cloud macrophysical properties are not affected by 10% changes in many environmental parameters. This can be applied to understanding the sensitivity of the AMPS to small changes in the environment. It is concluded that the sensitivity of the AMPS is small for small changes in the environment.

The domain and time average cloud top heights for the full variable range were plotted as a function of their variable values. There are many differences between the full range results and the $\pm$10% results. Some of these differences include a more disperse range of average cloud top heights. The $\pm$ 10% variable perturbation cloud top height plots had differences of meters between the clouds. The full range had cloud top heights between a few hundred meters and 2000 meters. Most of those heights were between 100% and 200% greater than the baseline cloud top height of just under 1000 m. The full range plots contain significantly fewer data points (thirteen total) and have at least one cloud belonging to one of the four cloud states. A single cloud was classified with decay. It's average cloud top height was 189.4 m. The stable cloud had an average cloud top height of 841.7 m. Three clouds were classified as 'dead'. These clouds had average cloud top heights of 1359 m, 1010 m, and 895 m. The eight clouds that fell into the 'growth' category had an average cloud top height of 1425 m. A threshold height of 2000 m appears with the cloud height. Not one of these clouds exceed 2000 m on average.

With an expanded initial ice concentration, no distinct trend is seen between the cloud tops and the ice in Figure 6.8(a). A similar conclusion can be made from Figures 6.8(b) and 6.8(c) where the initial concentration of large mode aerosols and the latent heat flux from the surface show no correlation between the cloud top height and increasing or decreasing values.

The sensible heat flux from the surface in Figure 6.8(d) and sea surface temperature in Figure 6.8(e) show a trend with the cloud top height. Increasing SHF from the surface

promotes cloud growth, with the decay and death clouds occurring with lower heat fluxes. The clouds that have growth increase their average cloud top height with higher heat fluxes. Heat from the surface drives air parcels upwards and mixes the boundary layer. These parcels can maintain the cloud and prevent the cloud from decoupling. The sea surface temperature and the heat flux at the surface are negatively correlated. This occurs because a larger heat flux will occur with a larger temperature difference between the air and sea, like with colder sea surface temperatures. The clouds with the highest top exist in the largest sensible heat flux and the lowest sea surface temperature. As sea surface temperature decreases the cloud top height of the the growing clouds begins to decrease as well. The decay and stable cloud do not follow this trend, and the death clouds congregate in a narrow range of sea surface temperatures. It is unknown if these sea surface temperatures will cause death of an AMPS, or if this grouping is circumstantial.

The cloud top height of any of the cloud states in Figure 6.8(f) does not have a strong trend with the surface momentum flux. The expectation was for this variable to increase the skin friction depth at the surface causing the speed of the fluid under the cloud to decrease, giving more time for upward moving water vapor and heat fluxes to reach condensation level before exiting the domain.

Figure 6.8(g) shows the cloud top heights increasing with increasing $m_{w_{ls}}$. Using the range of values of $m_{w_{ls}}$ in Equation 6.4 will most always produce negative vertical motion, or a general subsidence. The exception to this is when the highest values of $m_{w_{ls}}$ are multiplied by the pressure, the vertical motion will be positive. Sensitivity tests of the baseline initial point parameters were performed where the $w_{ls}$ set to zero. The SAM was integrated forward in time for 72 hours. The height of the cloud top continued to increase without hindrance for the entire duration. Diurnal effects were not seen in the clouds, reflecting the low solar forcing in the Arctic at this time. The behavior of the cloud top did not change for different configuration, i.e., CLUBB, without CLUBB, and CLUBB called every fifth dynamical time step. The cloud depth did not change so that the cloud base

was constantly increasing as well. It was understood that the profiles used in the baseline simulations would create a steady-state cloud so that the large-scale motion that pushed the cloud down and out of the domain was balanced with the rising of the boundary layer from positively buoyancy parcels. The magnitude of the $w_{ls}$ is small compared to $u$ and $v$, and the lower range of $m_{w_{ls}}$ contains some values orders of magnitude less than $w_{ls}$. When $m_{w_{ls}}p$ approaches and then exceeds 0.0431816 (m/s) to produce more positive $w_{ls}$, the cloud top grows.

Figures 6.8(h) and 6.8(i) show the plots of cloud top height with $b_\theta$ and $m_\theta$, the intercept and slope, respectively, of a line fit to the profile of potential temperature for pressure greater than 900 mb. A threshold of 300°K exists for $b_\theta$, and a slope of about 0.06 K°/mbar for $m_\theta$ with the existence of a cloud. As the average cloud tops approach these thresholds, the cloud state moves from a growth and stable cloud to a cloud that dies. An increasing slope of the potential temperature would cause a more unstable boundary layer and encourage convection. The intercept to of the potential temperature would be a corollary to the stability because changing $b_\theta$ would increase or decrease the initial value at the surface and the potential temperature at each level for a given slope. From the lack of clouds that exist for $m_\theta \geq 0.06$ and the dead clouds populating the highest values of $m_\theta$, we suggest that most of the range of $m_\theta$ used created a highly unstable vertical profile which caused first strong convective that drove many clouds through the top of the domain and ultimately into an unphysical realm.

The intercept and slope parameter ranges for water vapor profiles, $b_{q_v}$ and $m_{q_v}$, plotted with the cloud top heights are shown in Figures 6.8(j) and 6.8(k). There is a weak trend with increasing $b_{q_v}$ and average cloud top height. The higher values of $b_{q_v}$ provided more water vapor to condense and form or maintain the cloud. The cloud top increasing with increasing water vapor can be interpreted through the latent heat released. The latent heat released from the condensed water vapor provides additional heat into a parcel which in turn can continue to adiabatically rise. Cloud top is reached when the parcels become

negatively buoyant with respect to the surrounding air with heat given off in the form of the long wave inversion.

The relationship with $m_{q_v}$ and cloud top height appears to contain two thresholds. The first is with no cloud for $m_{q_v} \leq 0$, and the second is no clouds for $m_{q_v} > 0.01$. Both of these thresholds are perplexing because it was hypothesized that a simple relationship would develop where increasing the water vapor mixing ratio anywhere in the cloud's domain would be beneficial to cloud growth. When $m_{q_v} = 0$, the water vapor profile would be equal to $b_{q_v}$, so there would be water vapor available on which to form a cloud. With a negative slope, the water vapor mixing ratio would be increasing in height. A possible explanation for this is when the vertical gradient of equivalent potential temperature, $\theta_e$, is positive, the boundary layer is stable, prohibiting vertical mixing and cloud formation. The equivalent potential temperature is given by

$$\theta_e = \left( T + \frac{L_v}{c_p} q_v \right) \left( \frac{p_0}{p} \right)^{\frac{R_d}{c_p}}, \tag{6.8}$$

where $T$ is the temperature of the air at a pressure $p$, $p$ is the pressure of the air in mbar, $p_0$ is the standard reference pressure equal to 1000 mbar, $L_v$ is a constant called the latent heat of evaporation in (kJ/(kg K), $c_p$ is the specific heat capacity of dry air at constant pressure equal to 1004 J/(kg K), and $R_d$ is the specific gas constant for air equal to 287 J/(kg K). Equation 6.8 shows $\theta_e$ is proportional to the water vapor mixing ratio, and an increasing $q_v$ with height, or here a negative $m_{q_v}$, can create a stable layer preventing cloud development or ensuring cloud death.

The explanation for the threshold of cloud formation on the positive side of $m_{q_v}$ could be similar to the explanation of $m_\theta$. The rate of the water vapor mixing ratio decreasing in height creates a positive $\theta_e$ vertical gradient, $\partial\theta_e/\partial z > 0$. The atmosphere would be stable but unfavorable for clouds.

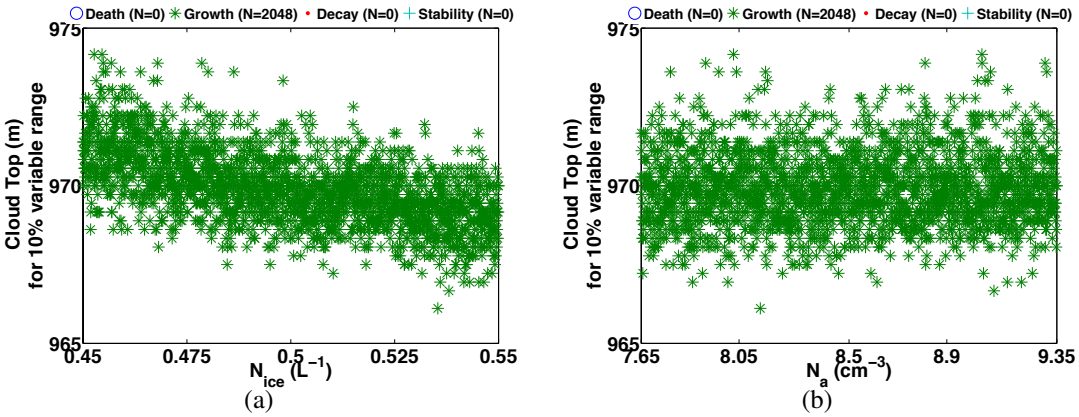
Death (N=0) Growth (N=2048) Decay (N=0) Stability (N=0)
Cloud Top (m) for 10% variable range
975
970
965
0.45
0.475
0.5
0.525
0.55
N_ice (L^-1)

(a)


Death (N=0) Growth (N=2048) Decay (N=0) Stability (N=0)
Cloud Top (m) for 10% variable range
975
970
965
7.65
8.05
8.5
8.9
9.35
N_a (cm^-3)

(b)

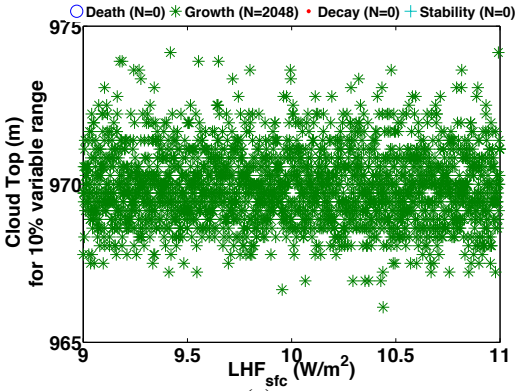
Death (N=0) Growth (N=2048) Decay (N=0) Stability (N=0)
Cloud Top (m) for 10% variable range
975
970
965
9
9.5
10
10.5
11
LHF_sfc (W/m^2)

(c)

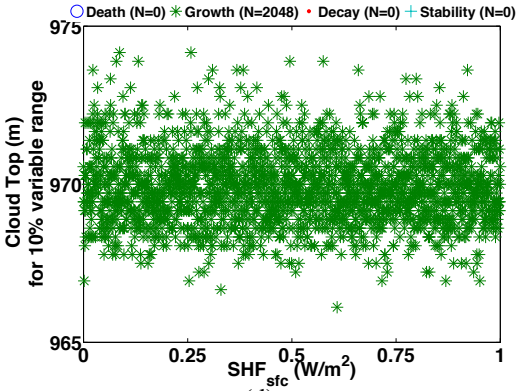
Death (N=0) Growth (N=2048) Decay (N=0) Stability (N=0)
Cloud Top (m) for 10% variable range
975
970
965
0
0.25
0.5
0.75
1
SHF_sfc (W/m^2)

(d)

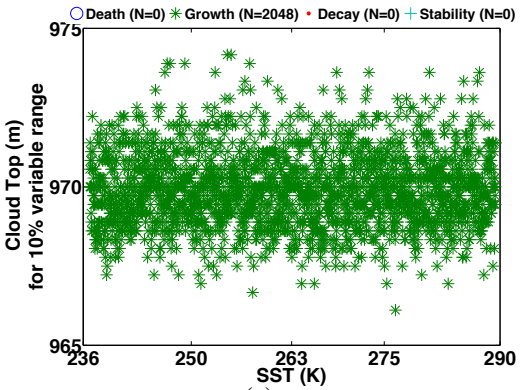
Death (N=0) Growth (N=2048) Decay (N=0) Stability (N=0)
Cloud Top (m) for 10% variable range
975
970
965
236
250
263
275
290
SST (K)

(e)

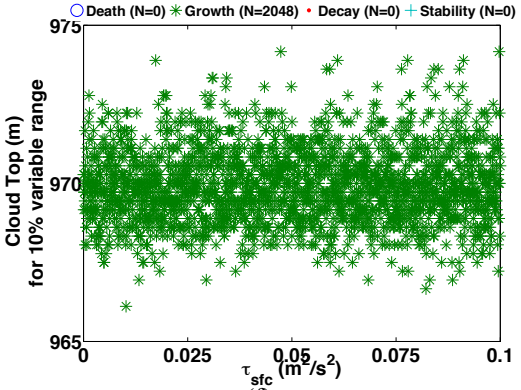
Death (N=0) Growth (N=2048) Decay (N=0) Stability (N=0)
Cloud Top (m) for 10% variable range
975
970
965
0
0.025
0.05
0.075
0.1
τ_sfc (m^2/s^2)

(f)

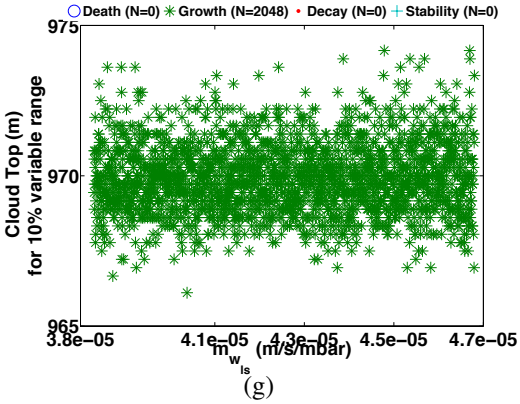
Death (N=0) Growth (N=2048) Decay (N=0) Stability (N=0)
Cloud Top (m) for 10% variable range
975
970
965
3.8e−05
4.1e−05
4.3e−05
4.5e−05
4.7e−05
m_w_ls (m/s/mbar)

(g)

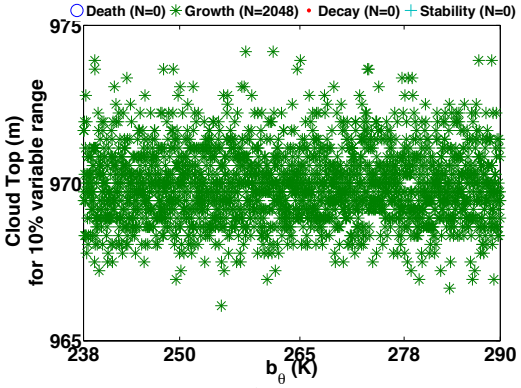
Death (N=0) Growth (N=2048) Decay (N=0) Stability (N=0)
Cloud Top (m) for 10% variable range
975
970
965
238
250
265
278
290
b_θ (K)

(h)

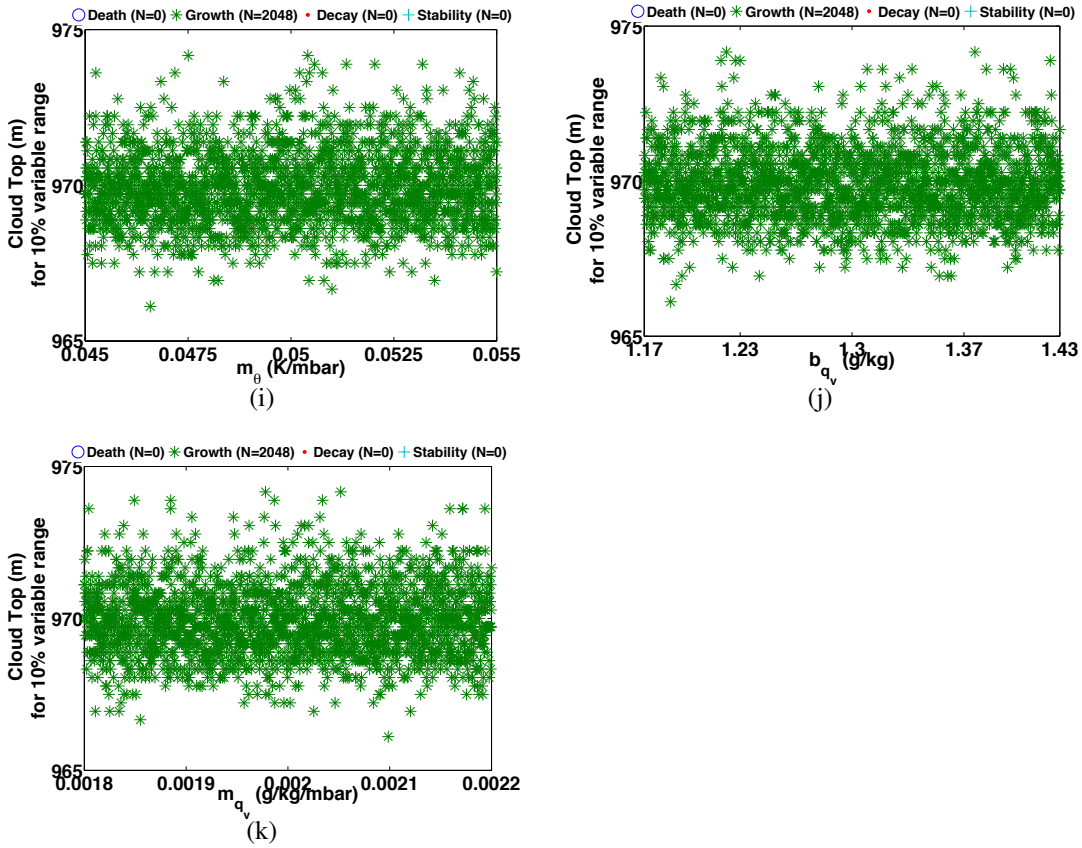


Figure 6.7: The cloud top height plotted as a function of (a) initial ice concentration, (b) initial large mode aerosol concentration, (c) latent heat flux from the surface, (d) sensible heat flux from the surface, (e) sea surface temperature, (f) surface momentum flux, (g) the slope value of a bilinear fit to the large-scale vertical motion profile that is used to initialize the atmospheric domain, (h) the y-intercept value of a bilinear fit to the potential profile that is used to initialize the atmospheric domain, (i) the slope value of a bilinear fit to the potential profile that is used to initialize the atmospheric domain, (j) the y-intercept value of a bilinear fit to the water vapor profile that is used to initialize the atmospheric domain, (k) the slope value of a bilinear fit to the potential profile that is used to initialize the atmospheric domain. The cloud top height is the domain and time-average of the simulation. The variable ranges were obtained from DAKOTA's LHS routine. The ranges were $\pm 10\%$ perturbations from the initial point value listed in Table 6.2, and 2048 simulations were executed to produced an AMPS, and every cloud was found to have an increasing cloud top height over time as defined by Table 6.3.

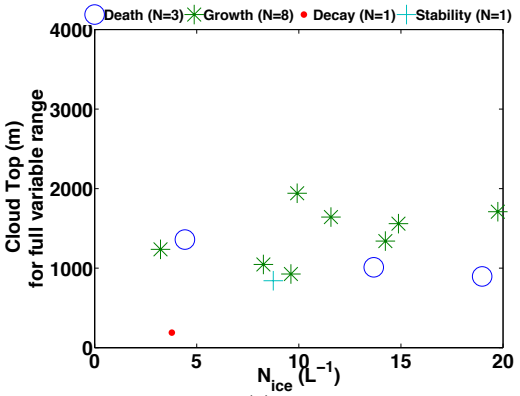
Death (N=3) Growth (N=8) Decay (N=1) Stability (N=1)
Cloud Top (m) for full variable range
0
1000
2000
3000
4000
0
5
10
15
20
N_ice (L^-1)

(a)

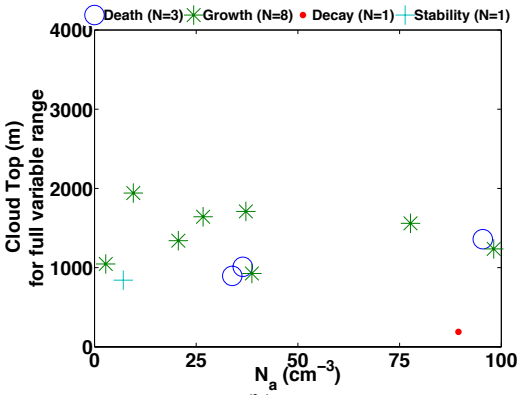
Death (N=3) Growth (N=8) Decay (N=1) Stability (N=1)
Cloud Top (m) for full variable range
0
1000
2000
3000
4000
0
25
50
75
100
N_a (cm^-3)

(b)

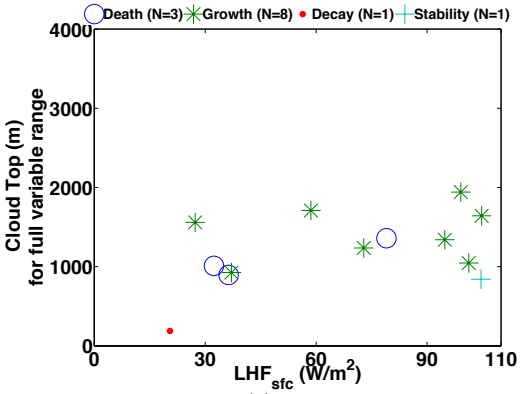
Death (N=3) Growth (N=8) Decay (N=1) Stability (N=1)
Cloud Top (m) for full variable range
0
1000
2000
3000
4000
0
30
60
90
110
LHF_sfc (W/m^2)

(c)

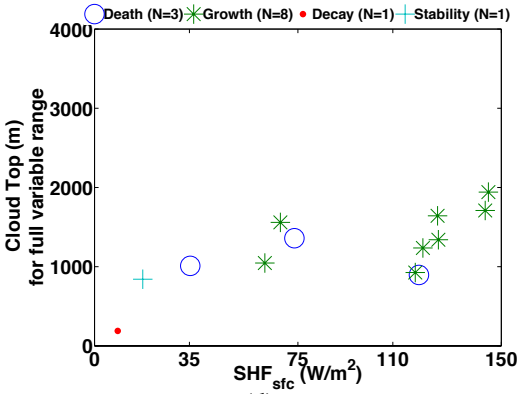
Death (N=3) Growth (N=8) Decay (N=1) Stability (N=1)
Cloud Top (m) for full variable range
0
1000
2000
3000
4000
0
35
75
110
150
SHF_sfc (W/m^2)

(d)

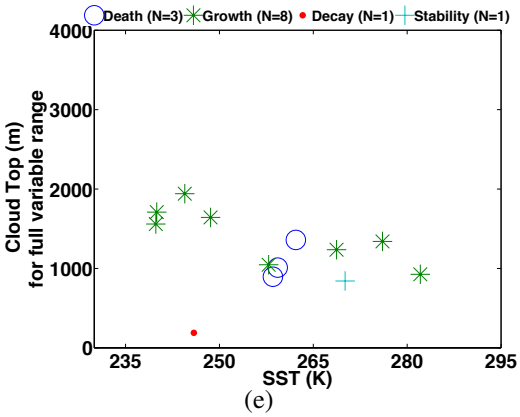
Death (N=3) Growth (N=8) Decay (N=1) Stability (N=1)
Cloud Top (m) for full variable range
0
1000
2000
3000
4000
235
250
265
280
295
SST (K)

(e)

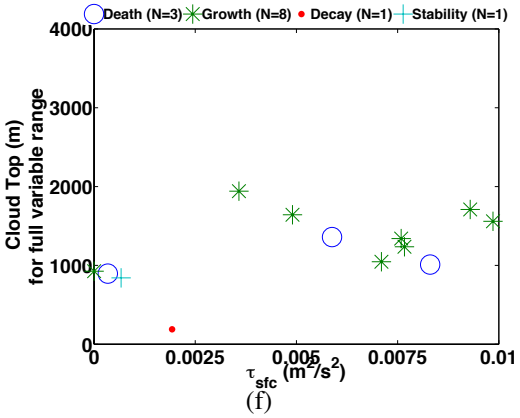
Death (N=3) Growth (N=8) Decay (N=1) Stability (N=1)
Cloud Top (m) for full variable range
0
1000
2000
3000
4000
0
0.0025
0.005
0.0075
0.01
τ_sfc (m^2/s^2)

(f)

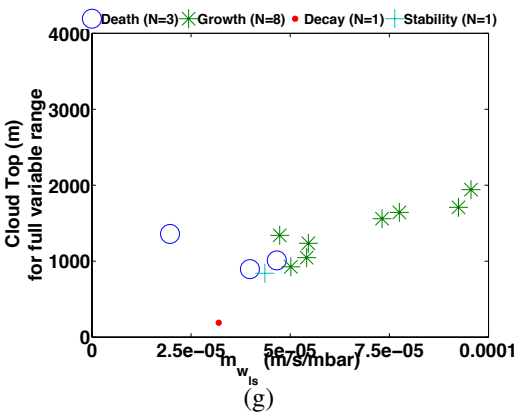
Death (N=3) Growth (N=8) Decay (N=1) Stability (N=1)
Cloud Top (m) for full variable range
0
1000
2000
3000
4000
0
2.5e−05
5e−05
7.5e−05
0.0001
m_w_ls (m/s/mbar)

(g)

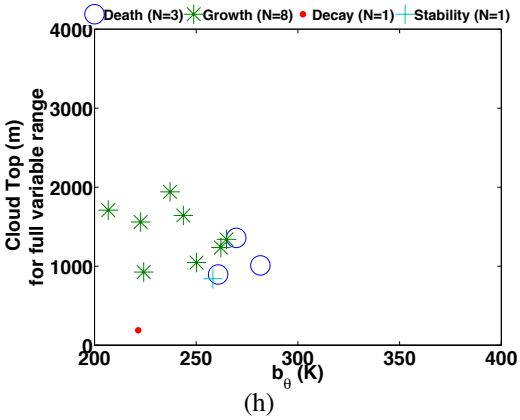
Death (N=3) Growth (N=8) Decay (N=1) Stability (N=1)
Cloud Top (m) for full variable range
0
1000
2000
3000
4000
200
250
300
350
400
b_θ (K)

(h)

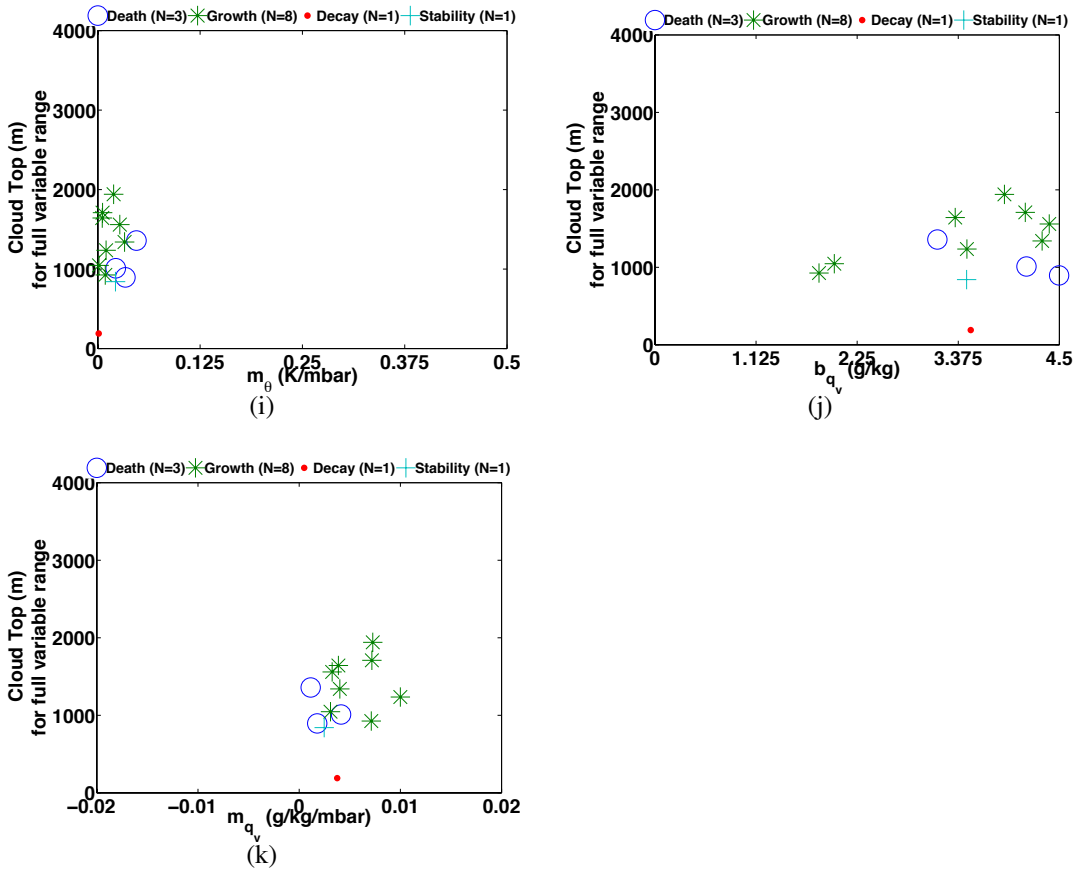


Figure 6.8: The cloud top height plotted as a function of (a) initial ice concentration, (b) initial large mode aerosol concentration, (c) latent heat flux from the surface, (d) sensible heat flux from the surface, (e) sea surface temperature, (f) surface momentum flux, (g) the slope value of a bilinear fit to the large-scale vertical motion profile that is used to initialize the atmospheric domain, (h) the y-intercept value of a bilinear fit to the potential profile that is used to initialize the atmospheric domain, (i) the slope value of a bilinear fit to the potential profile that is used to initialize the atmospheric domain, (j) the y-intercept value of a bilinear fit to the water vapor profile that is used to initialize the atmospheric domain, (k) the slope value of a bilinear fit to the potential profile that is used to initialize the atmospheric domain. The cloud top height is the domain and time-average of the simulation. The variable ranges were full variable range perturbations from the initial point value listed in Table 6.2. The variable ranges were obtained from DAKOTA's LHS routine, and 2048 simulations were executed in try to produce an AMPS. Three clouds cloud deaths occurred (blue circles), eight cloud tops displayed growth (green asterisk), one cloud decayed (red dot), and one cloud was stable (turquoise cross) in the simulated time of analysis as defined by Table 6.3.

### 6.3.4 General Cloud Properties

The clouds produced from this parameter study were initialized in some conditions that were outside what is commonly found in the Arctic. We wish to know how similar these clouds are to the steady-state AMPS clouds studied in Chapters III and IV, and if these clouds fall into the range of observed single-layer AMPS described by *de Boer et al.* (2009).

Figure 6.9 shows the average of all the cloud simulations for the $\pm$ 10% variable perturbation study. The variance between the clouds produced was smaller than in the full variable range LHS study, so it was felt the mean of all the plots would be sufficient to show the characteristics of the clouds from this ensemble set. The similarities between Figure 6.9 and the baseline bulk clouds from Chapters III and IV include the same magnitudes between the water and ice mass mixing ratios. The liquid layer increases at the cloud top in time. The ice precipitate from the cloud reaches the surface, similar to the baseline AMPS clouds.

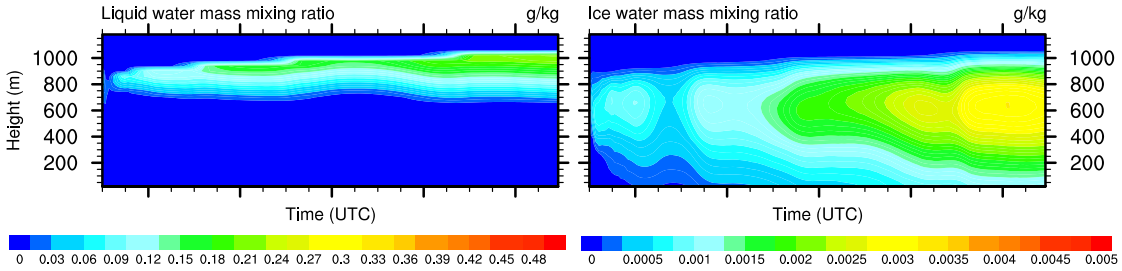


Figure 6.9: The total average liquid (panel on left) and total average ice (panel on right) mass mixing ratio of the domain-average profiles in the simulated time. The 2048-member ensemble set was averaged to produce these cloud contours. The ensemble is from the LHS $\pm$ 10% parameter range study.

Figure 6.10 shows total liquid and total ice water mass mixing ratio profiles as a function of time for the full range of variable perturbations for the thirteen simulations that were produced clouds. The contour spacing is chosen from the minimum and maximum of the thirteen cloud plots, so very small concentrations of cloud condensate cannot appear as in the eighth and twelfth plots. The states of the clouds are as follows from top to bottom:

the first two are growth; the third is death; the fourth is growth; the fifth is stability; the sixth is death; the seventh is death; the eighth is death; the ninth, tenth, and eleventh are growth; the twelfth is decay; the thirteenth is growth. The cloud develop a increasing mass concentration at the top of the cloud as the time progresses. This characteristic is seen in the baseline simulations.

A notable property of these clouds is the ratio of liquid to ice. It was expected from the findings in previous modeling studies that the up-to 400 $\times$ increase in initial ice concentration would quickly glaciate the cloud and cause cloud death or decay (*Ovchinnikov et al.*, 2011). This was not the finding here. Instead, the the initial ice concentrations in the clouds in Figure 6.10 are at least an order of magnitude greater than the initial point. This ice concentration caused ratio of the ice and liquid mixing ratios to be $\approx$1 in many of the clouds. The coexistence of liquid with such large amounts of ice needs to be observationally validated and further explored numerically. The second, fifth, seventh, eleventh, and thirteenth contour plots show modes of strong ice precipitation when the liquid precipitation appears to recede. These clouds could be dynamically driven by convection instead of long wave cooling at cloud top, which is different from the baseline simulations.

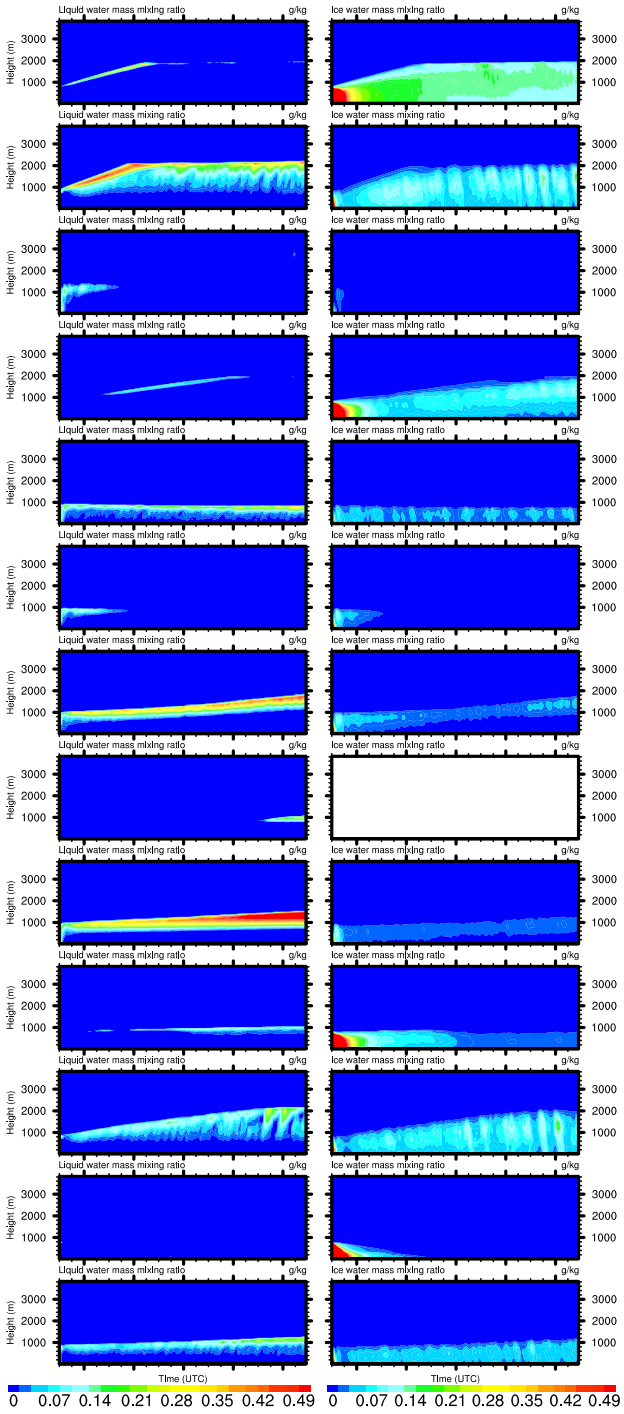


Figure 6.10: The total liquid (13 panels on left) and total ice (13 panels on right) mass mixing ratio domain-average profiles in the simulated time. These cloud contours are the thirteen (out of 2048) clouds that were produced from the LHS full parameter range study.

### 6.3.5 Sensitivity of Results to Changing Model Configurations

We would want to know the sensitivity of this system regardless of the modeling parameterizations. For instance, *Seifert et al.* (2006) found that different concentrations of CCN had more affect on the resulting cloud than using different bin and bulk microphysics schemes in a convective system. We would like to have the findings such as these and similar to the relationships in the full variable range LHS between the SBM and bulk microphysics parameterizations and the CLUBB and 1.5TKE subgrid scale parameterizations. The SBM is the state-of-the-art in microphysics, and the cloud properties have essentially no change between the dimensionality or subgrid scale turbulent parameterization. Using the bulk microphysics in concert with the CLUBB showed much change in cloud properties. The bulk microphysics without CLUBB showed no dependence on dimensionality, but with CLUBB the cloud ceased to exist just after 12 hours. We inquire as to how absolute these findings are when the environmental parameters are changed.

The same model set-up was used with DAKOTA's LHS parameter set to generate 2048 clouds, but the CLUBB parameterization was used in SAM instead of just the 1.5TKE closure. Appendix B contains the time series, scatter plots, and contour plots shown here for the $\pm 10\%$ and full range variable perturbation studies. Eleven instead of thirteen clouds were produced when CLUBB was included. The missing two clouds in Figure B.3 were the sixth and eighth clouds of the set shown in Figure 6.10.

In the time series plot, the cloud depth does not fill the entire domain and seen in the bulk with 1.5TKE scheme. There were more simulation runs that had realistic values for a longer duration with CLUBB, but most of those evolved to an unphysical state.

In the contoured plots, the clouds produced with CLUBB have greater liquid mass concentrations. The precipitation patters in the ice seen in the 1.5TKE scheme are missing with the CLUBB, and the ice has a tendency to abruptly decrease towards the end of the modeled time.

In the scatter plots of the full variable range plotted with the cloud top height, four

clouds were identified as 'death' and seven cloud were identified as 'growing'. There were no 'stability' or 'decay' clouds from this set. Some similar relationships between the cloud top and the variable ranges were seen with the CLUBB.

It is remarkable that in the baseline studies the choice of turbulence closure scheme had a large influence on cloud structure, yet when the different configurations were tested in a large parameter range, the same variable values were consistent in producing the clouds. This implies the parameterization of the cloud physics should require case-specific adjustments. The full variable range might have pushed atmospheric configurations too far from the springtime Arctic, so we also wonder if this result holds for using the other microphysics scheme, the SBM, for a 3D configuration, and for the $\pm 10\%$ variable range.

### 6.3.6 Sensitivity Analysis of Variables Held Constant

In *Peterson et al.* (2010)'s SA study, two types of parameter studies were performed. The first was a one-at-a-time parameters study which has the benefit of showing the importance of a parameter on the result, but cannot estimate interactions between the parameters and the effect on the result. The second type of parameter study was a LHS study which has the benefit of being able to give ranks to the variables on order of influence on the results. The ranking and the influence of the variables was ascertained by using two linear regression models, one for each type of SA study, and computing the standardized regression coefficient with the parameter value and the model result. This type of analysis could be applied here and would be a quantitative way to see relationships in the variables with the results. However, the scatter plots of the variable's range with the cloud top quickly show regression coefficients will be small for two reasons. The first is will be due to the large variability in the cloud top values for the $\pm 10\%$ range, and the second is due to the small sample size of the cloud states in the full variable range. For comparison, *Peterson et al.* (2010)'s standardized regression coefficients ranged from about (-1 to 1), making ranking straightforward.

Future work could include a SA study to explore linear relationships with the parameters and the cloud.

## 6.4 Summary

An extensive environmental parameter study was performed on Arctic Mixed-Phase Stratocumulus. The Design Analysis Kit for Optimization and Terascale Applications toolkit was coupled to the atmospheric Large Eddy Simulation model, System for Atmospheric Modeling, v6.8.2. DAKOTA produced 2048 values for 11 variable each that were given to SAM to create the mixed-phase cloud. Two of these 11 variables explored microphysical aspects of the cloud: initial ice concentration and large mode aerosol concentration. Four of the 11 variables were surface parameters: sea surface temperature, latent heat flux, sensible heat flux, and momentum flux. The five remaining variables were used to initialize the vertical domain of the simulation: large-scale vertical motion, y-intercept and slope of fits to the potential temperature profiles, and y-intercept and slope of fits to the water vapor profile.

Two separate variable ranges were used. The first range was a $\pm$ 10% variable range from the initial points of baseline simulations that had well-established steady-state AMPS. The second range expanded from the 10% change to a fuller range of variable perturbations. Four conditions were defined into which the cloud groups were placed: cloud stability, cloud growth, cloud decay, and cloud death.

The results of the ensembles of simulations from the $\pm$ 10% variable perturbation showed very little deviation from the baseline simulation. The exception to this was the cloud top height and initial ice concentration where an increasing ice concentration caused the average cloud top height to decrease. Increasing ice concentration is expected to increase glaciation rates so the cloud will eventually precipitate away with large enough ice concentrations.

The results from the full variable range were different than the $\pm$ 10% range. Instead

of 2048 successfully completed simulations of an AMPS, the full variable range ensemble had thirteen data points that were able to be used. Three of the thirteen were classified as clouds with death, eight clouds were considered growing, one cloud decayed, and the last cloud was stable. No apparent relationship was seen between the microphysical variables: initial ice concentration and coarse mode aerosol concentration. Changes in the surface parameters of sensible heat flux and the sea surface temperature were found to have an influence on cloud top height and cloud state. With decreasing SST (increasing SHF), the cloud top height decreased (increased). No relationship was seen between the cloud top height and neither the surface latent heat nor the surface momentum fluxes. Cloud top height had clear relationships with the profile parameters, $m_{w_{ls}}$, $b_\theta$, $m_\theta$, $m_{w_{ls}}$, and $m_{w_{ls}}$. It was found that certain values of the profile parameters caused stability thresholds to appear. As these thresholds were approached, the cloud state changed from growth and stability to death and decay.

We implemented a novel and unique way of performing a sensitivity analysis of AMPS. The response of the AMPS to changing environmental parameters was tested by marching through a parameter space constructed by a LHS routine. The existence of the AMPS was found to be highly sensitive to changes in the environment over the ranges explored here.

# CHAPTER VII

# Conclusions

Numerical experiments produced a steady-state Arctic Mixed-Phase Stratocumulus (AMPS) cloud over a 24-hour period that exhibited many of the properties of the observed cloud, including the presence of liquid water at cloud top with transition to ice below and a nearly constant cloud top height.

The level of complexity needed to simulate this cloud was found by comparing two microphysics routines, Spectral Bin Microphysics (SBM) and bulk, and two subgrid scale turbulent closure models, Cloud Layers Unified By Binormals (CLUBB) and 1.5-Turbulent Kinetic Energy (TKE). It was found the both microphysics accurately produced macrophysical properties of the observed cloud, and that the less computationally expensive microphysics parameterization could be used to reproduce the AMPS. The use of SBM resulted in more accurate simulation of frozen hydrometeor mass mixing ratio than the bulk, though both schemes consistently under-predict the mass mixing ratio of frozen hydrometers while over-predicting the ice number concentration. It was found the choice of turbulent closure model had more of an effect on the cloud properties than the choice of microphysics. The cloud-top height decreased and the cloud's condensed ice and water mass became depleted when the higher-order turbulence parameterization, CLUBB), was used. A more physically-representative solution should be applied to CLUBB which could include parameter tuning and a re-evaluation of the influence that CLUBB has within the

bulk microphysics. Additional simulation complexity was assessed through dimensionality studies. The time and resources required to perform Three-Dimensions (3D) cloud simulations motived a dimensionality study, so the impact of choosing a Two-Dimensions (2D) or 3D configuration with each of the turbulence and microphysical models was assessed. It was found that using a 2D configurations produced similar results to the 3D simulations.

The results and knowledge of the parameterizations needed for representing the AMPS were used in an Latin-Hypercube Sample (LHS) sensitivity study. It was found the bulk microphysics and 1.5-TKE turbulence scheme in a 2D configuration would be the best combination for efficiency and accuracy for a multi-variable sensitivity analysis. System for Atmospheric Modeling, v6.8.2 (SAM) model was coupled to the uncertainty quantification toolkit, Design Analysis Kit for Optimization and Terascale Applications (DAKOTA). DAKOTA produced uniform parameter ranges of specified variables to be given as input to SAM. Two sets of parameter ranges were tested: a $\pm 10\%$ perturbation from the initial variable values and a broader range. The environmental variables that were changed were the cloud ice and aerosol concentration, surface sensible and latent heat fluxes, and large scale temperature, water vapor, and vertical motion. Four characteristic fates were used to classify outcome of the simulated AMPS: stability, growth, decay, and dissipation. These fates were defined from cloud top total water mixing ratio values during the simulation period.

In the $\pm 10\%$ range, it was found that the AMPS clouds did not significantly change from the baseline value. Near-zero correlations were found between the changing variables and the cloud top with the exception of initial ice concentration. As ice concentration increased, the cloud top decreased due to cloud glaciation. In the full variable range, it was found the AMPS was most sensitive to changes in large-scale temperature, water vapor, and vertical motion in the variable ranges we investigated. There were not many clouds that formed from the full variable range compared to the size of the ensemble set. This was attributed to the appearance of environmental thresholds that made mixed-phase cloud

formation prohibitive.

The work presented here gave insight to the interactions between model parameterizations and the necessary complexity of the parameterizations needed to simulate AMPS realistically. The application of parameter estimation algorithms to investigate cloud-climate interactions has never been done before. We found this application successful to this problem. This optimization study which finds conditions of cloud failure is a new analysis tool that can be applied to many other challenging and important problems in the earth system.

# APPENDICES

# APPENDIX A

# Death of an Arctic Mixed-Phase Stratocumulus Cloud – DAKOTA scripts

## A.1 DAKOTA LHS Script Description

This Dakota input file performs a Latin Hypercube Sampling study using the SAM model.

Specification blocks are identified in the input file using the following keywords: strategy, method, variables, interface, and responses. These keyword blocks can appear in any order in a DAKOTA input file. The strategy section specifies the method and the type of output for Design Analysis Kit for Optimization and Terascale Applications (DAKOTA). The method section specifies which technique DAKOTA will use. Here a sampling technique will be used with 2048 samples. The seed specifies the random number generator seed, and the sample type specifies the lhs, or Latin Hypercube Sampling, with all the variables.

The variable section block specifies the names of the variables, their bounds, and how the variable ranges will be divided. The interface section block of the input file specifies how information will be passed between DAKOTA and the host model code. Here, the

```
# This Dakota input file performs a Latin Hypercube Sample study using the SAM model.
strategy,
  single_method
  tabular_graphics_data
method,
  sampling,
    samples = 2048
    seed = 98765 rng rnum2
    sample_type lhs
    all_variables
variables,
  uniform_uncertain = 11
  lower_bounds  =   0.0      0.0   233.15     0.0 0.0     0.00  0.000001 200     0.0     0.0    -0.020
  upper_bounds  = 20.0    100.0   293.15   150.0 110.0   0.01  0.0001   400     0.5     4.5     0.020
  descriptor    = 'Ice0' 'aer_n2' 'sst'   'se'  'le'  'tau'  'm_w'  'b_tp' 'm_tp'  'b_qv' 'm_qv'
interface,
  system
  analysis_driver = 'simulator_script_mkdir.csh'
  parameters_file = 'params.in'
  results_file    = 'results.out'
  failure_capture = recover NaN
responses,
  response_functions = 1
  no_gradients
  no_hessians
```

Figure A.1: DAKOTA input file for the LHS study used with the SAM model. Shown are the keywords used in the input file, the variable ranges, and the variables.

analysis driver keyword refers to the shell script built for this research which provides the necessary information from DAKOTA to System for Atmospheric Modeling, v6.8.2 (SAM). The parameter file and results file are placeholders but necessary files to copy information from DAKOTA. The responses section of the input file specifies the types of data that the interface will return to DAKOTA. For the example shown in Figure A.1, setting the response functions equal to 1 indicates that there is only one objective function. The keywords no gradients and no hessians indicate that no derivatives will be provided to the method; none are needed for a parameter study.

# APPENDIX B

# Death of an Arctic Mixed-Phase Stratocumulus Cloud – Bulk with CLUBB results

## B.1 Time Series

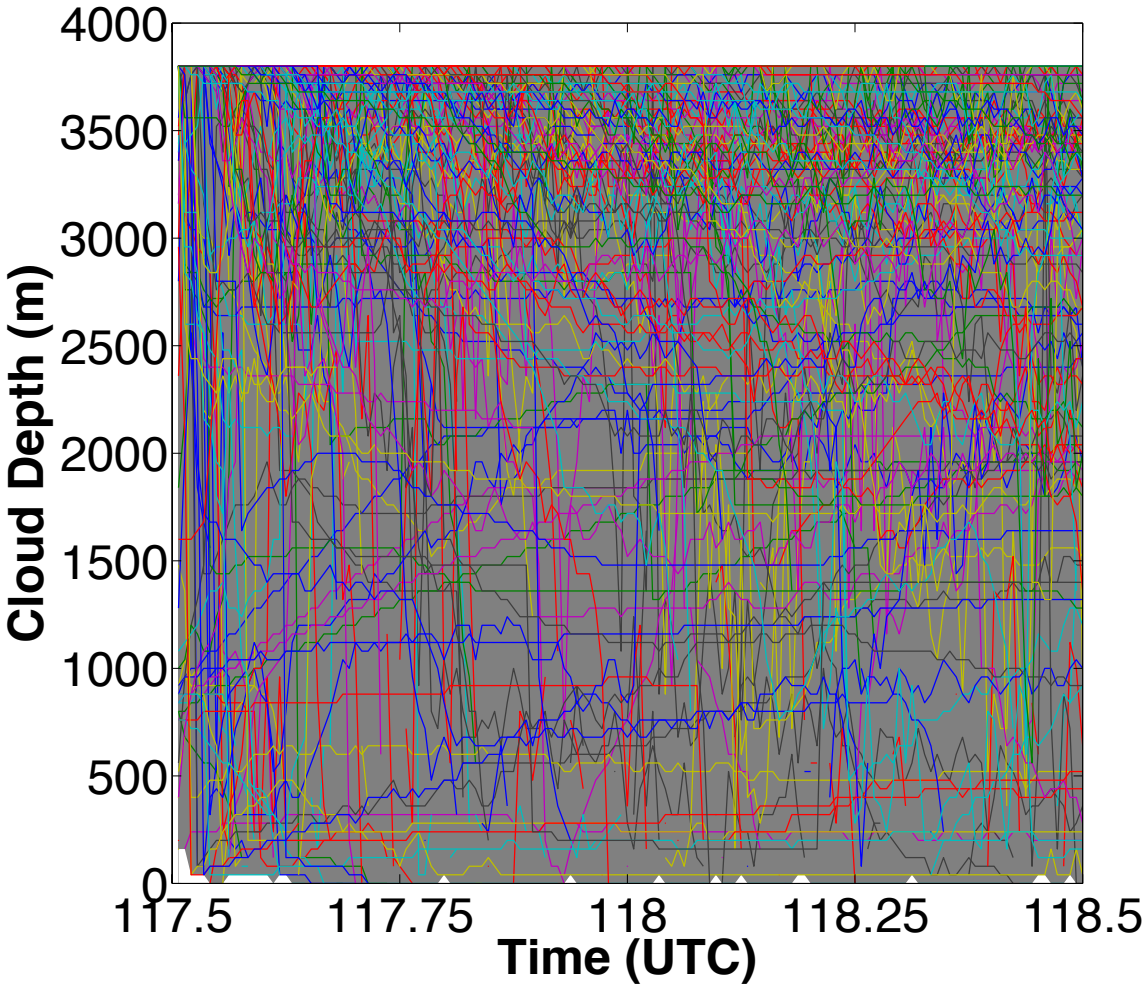


Figure B.1: The time evolution of the cloud depth for the 2048 simulations including the CLUBB turbulent parameterization in SAM where the variables were tested in the full range of values listed in Table 6.2. As in Figure 6.3, each run is represented by a colored line. However, the colors have been repeated in plotting this ensemble. For example, that means the color blue is repeated many times in this graph. The grey shading represents the absolute minimum and maximum at that time for the entire set of simulations.

## B.2 Scatter Plots

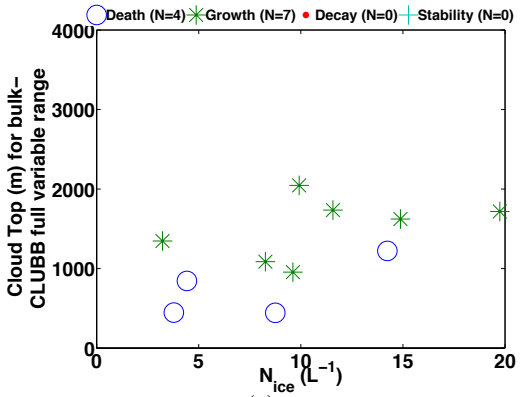


(a)

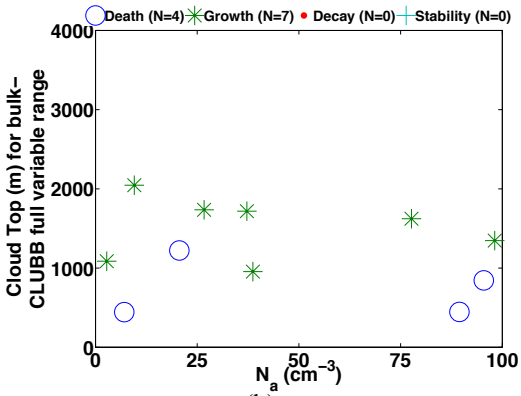


(b)

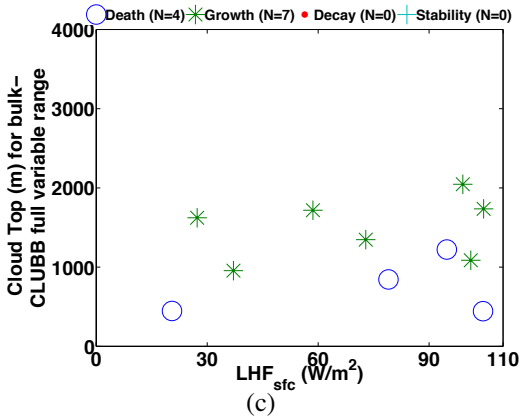


(c)

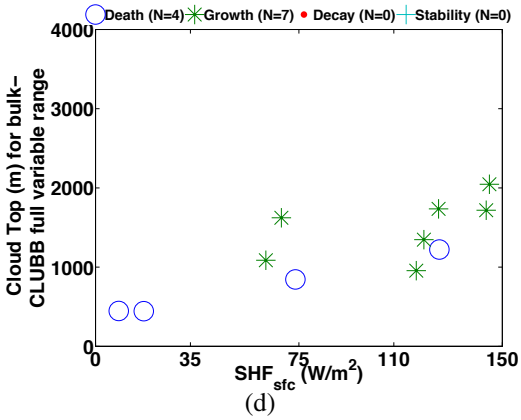


(d)

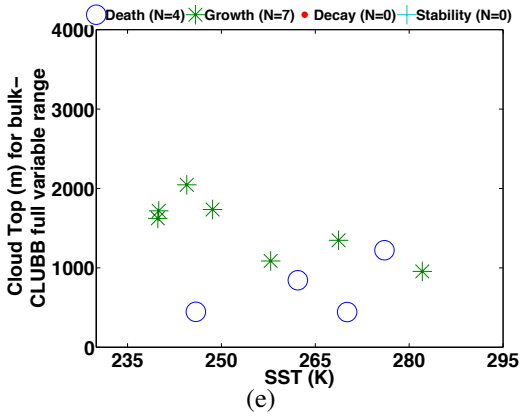


(e)

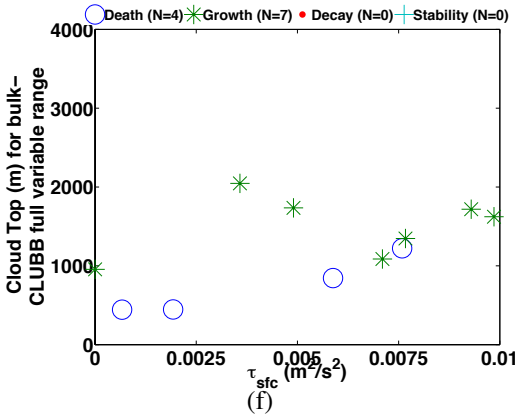


(f)

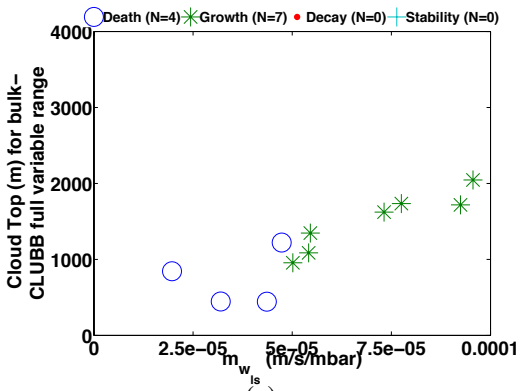
Death (N=4)
Growth (N=7)
Decay (N=0)
Stability (N=0)
Cloud Top (m) for bulk–CLUBB full variable range
4000
3000
2000
1000
0
0
2.5e−05
5e−05
7.5e−05
0.0001
m_w_ls (m/s/mbar)

(g)

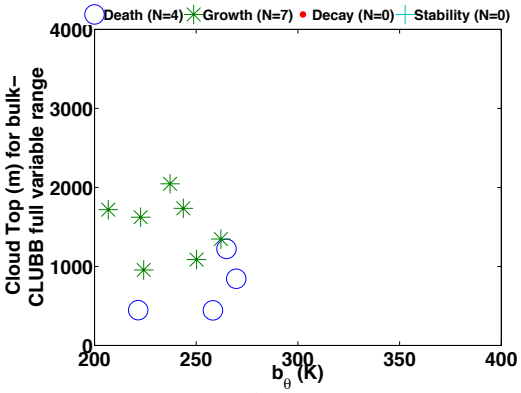
Death (N=4)
Growth (N=7)
Decay (N=0)
Stability (N=0)
Cloud Top (m) for bulk–CLUBB full variable range
4000
3000
2000
1000
0
200
250
300
350
400
b_θ (K)

(h)

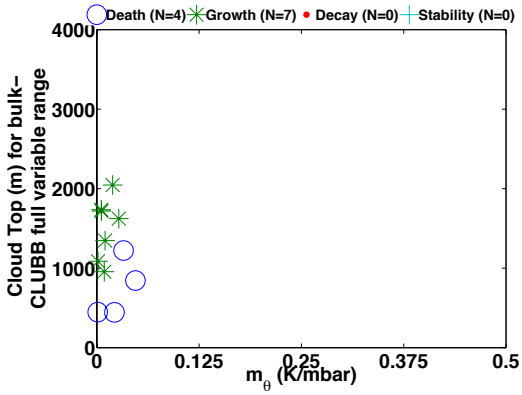
Death (N=4)
Growth (N=7)
Decay (N=0)
Stability (N=0)
Cloud Top (m) for bulk–CLUBB full variable range
4000
3000
2000
1000
0
0
0.125
0.25
0.375
0.5
m_θ (K/mbar)

(i)

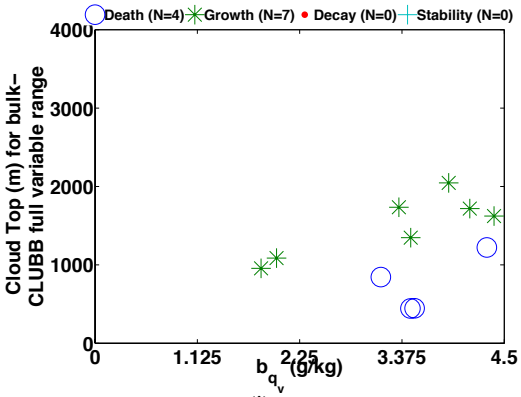
Death (N=4)
Growth (N=7)
Decay (N=0)
Stability (N=0)
Cloud Top (m) for bulk–CLUBB full variable range
4000
3000
2000
1000
0
0
1.125
2.25
3.375
4.5
b_q_v (g/kg)

(j)

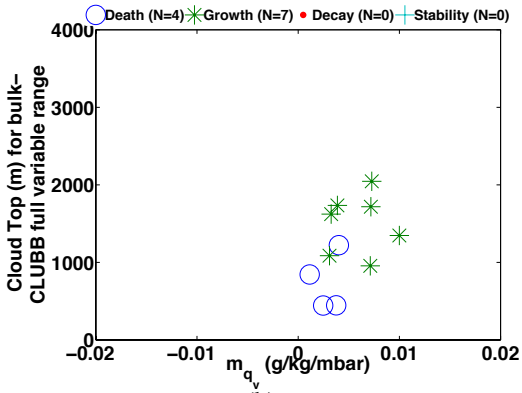
Death (N=4)
Growth (N=7)
Decay (N=0)
Stability (N=0)
Cloud Top (m) for bulk–CLUBB full variable range
4000
3000
2000
1000
0
−0.02
−0.01
0
0.01
0.02
m_q_v (g/kg/mbar)

(k)

Figure B.2: The cloud top height plotted as a function of (a) initial ice concentration, (b) initial large mode aerosol concentration, (c) latent heat flux from the surface, (d) sensible heat flux from the surface, (e) sea surface temperature, (f) surface momentum flux, (g) the slope value of a bilinear fit to the large-scale vertical motion profile that is used to initialize the atmospheric domain, (h) the y-intercept value of a bilinear fit to the potential profile that is used to initialize the atmospheric domain, (i) the slope value of a bilinear fit to the potential profile that is used to initialize the atmospheric domain, (j) the y-intercept value of a bilinear fit to the water vapor profile that is used to initialize the atmospheric domain, (k) the slope value of a bilinear fit to the potential profile that is used to initialize the atmospheric domain. The cloud top height is the domain and time-average of the simulation. The variable ranges were fobtained from DAKOTA's LHS routine, and in this case included the CLUBB turbulent parameterization in SAM. The ranges were full variable range perturbations from the initial point value listed in Table 6.2. 2048 simulations were executed in try to produce an AMPS. Three clouds cloud deaths occurred (blue circles), eight cloud tops displayed growth (green asterisk), one cloud decayed (red dot), and one cloud was stable (turquoise cross) in the simulated time of analysis as defined by Table 6.3.

## B.3 Contour Plots

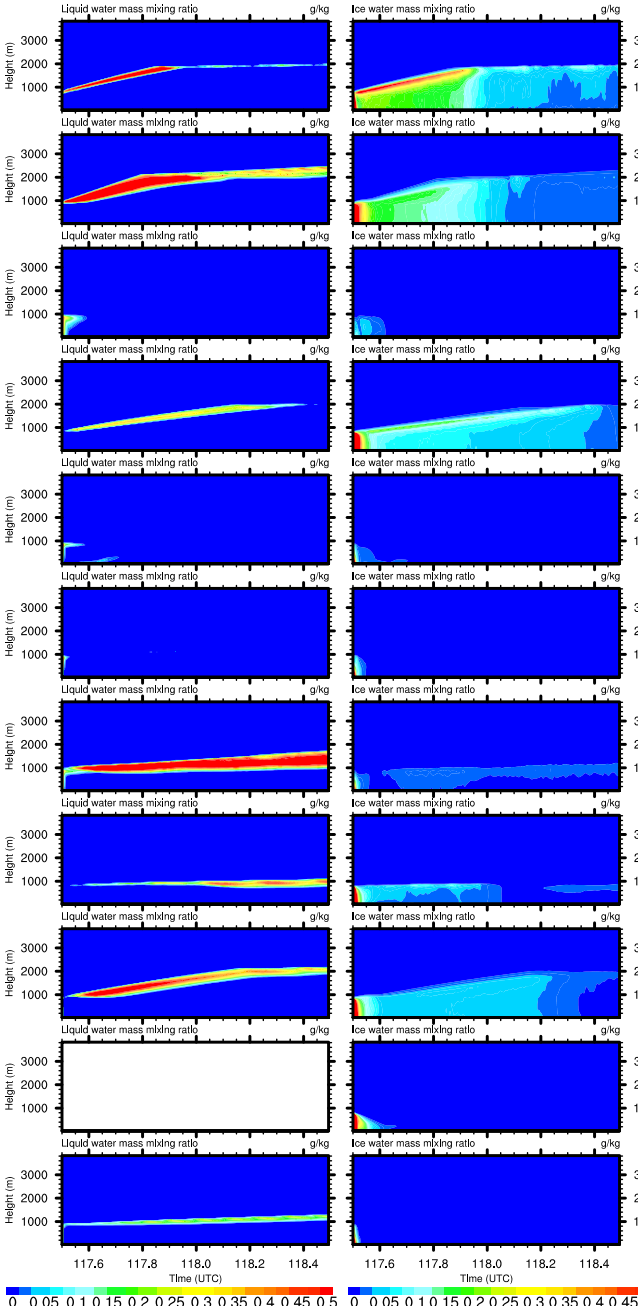


Figure B.3: The total liquid (11 panels on left) and total ice (11 panels on right) mass mixing ratio domain-average profiles in the simulated time. These cloud contours are the thirteen (out of 2048) clouds that were produced from the LHS full parameter range study with the CLUBB turbulent parameterization included in SAM.

# APPENDIX C

# A Model for Soot Chain Compaction

## C.1 Introduction

Soot particles represent one type of composition of aerosol. High concentrations of soot particles are known to adversely affect human health (*Davidson et al.*, 2005) and to exert a climatic forcing over highly industrialized and polluted regions (*Ramanathan et al.*, 2005). The structure, composition, and size of these soot particles have been imaged with electron microscopes (*Adachi and Buseck*, 2008; *Zhang et al.*, 2008). The images from the electron microscopes show that soot particles are microscopic near-spherical balls of carbon, or carbonaceous spherules, with graphitic structures. The spherules are formed from the incomplete combustion of organic material. The composition of soot chains are mostly carbon graphite with small concentrations of other chemical components that vary depending on the combustion source's characteristics. The soot chain's morphology, lifetime, and radiative properties may change if it is coated with water, sulfates, and/or organic material (*Adachi et al.*, 2010). Knowing the soot chain lifetime and morphology will help quantify its impact on human health and climate forcing.

The soot spherules have been observed as either spread-out in aggregates and chain-like structures or closely bound and compacted. *Zhang et al.* (2008) showed Transmission

Electron Microscope (TEM) images of a fresh soot aggregate and of a compacted soot mass after exposure to sulfuric acid, $H_2SO_4$, vapor at 5% relative humidity. The individual spherules appear to be $\sim$ 20 $\mu$m. The size and mobility diameter significantly decreased as seen in Figure C.1. The soot aerosol is also observed to be embedded in organic or inorganic material. *Adachi and Buseck* (2008) also imaged soot particles with a TEM that were collected from the Megacity Initiative: Local and Global Research Observations (MILAGRO) campaign in and near Mexico City. In the Mexico City plumes, they found more than half of the particles that contained soot was coated by organic matter and sulfates. These soot particles were not compacted, even though they were coated. The soot particles appear to be less coated as found by *Adachi and Buseck* (2008) than by *Zhang et al.* (2008). The direct radiative forcing of a soot aerosol particles that is not compacted and embedded at the center of other material is 20% less than a soot aerosol particle that is assumed to be the core of the aerosol (*Adachi et al.*, 2010).

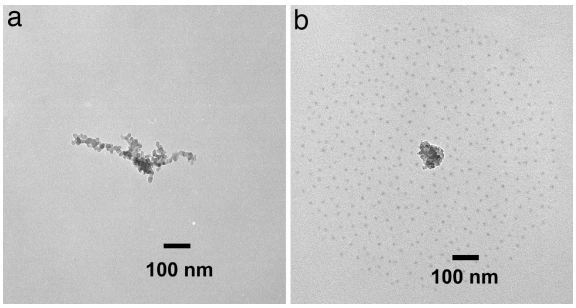


Figure C.1: *Zhang et al.* (2008)'s "TEM images of soot particles: fresh soot (a) and soot after exposure to $H_2SO_4$ vapor and 5% RH (b). The gaseous concentration of sulfuric acid is 1.4 x $10^{10}$ molecules cm$^{-3}$. "

This paper compares the results of two, Two-Dimensions (2D) models used to predict the soot chain shape evolution into a compacted soot sphere. The equations used to predict the evolution are derived in each model's method section. The equations are integrated in a numerical model, and the results from that integration are presented in each of the model's results section. A discussion and summary is given in Section C.3.

## C.2 Models

### C.2.1 Development of a Model

The method for deriving the equations of motion for the soot spherules began with developing they influence of the surrounding atmospheric gas with the soot chain. It is first assumed that nucleation from a surrounding gas begins in the cusps between two soot spherules. The atmospheric gas impacting the soot spherules is at a temperature and pressure where condensation occurs. The atmospheric gas is supersaturated with respect to the soot chain. Upon introduction of the soot chain, condensation can begin on the surface. The condensate begins to accumulate unequally in the crevasses between the soot spherules. It is also assumed that the soot granules are insoluble and no chemical reaction is occurring on the surface (*Zhang and Zhang*, 2005). Figure C.2 is a conceptual image of how the gas might accumulation unequally on the soot aggregate.

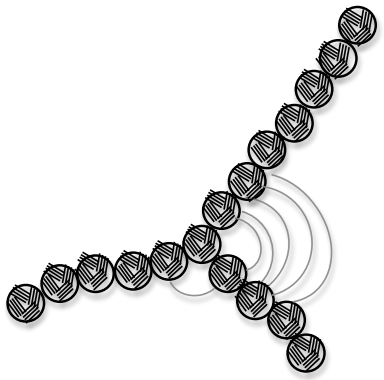

Figure C.2: Soot spherules are composed of layers of graphite. Unequal liquid accumulation causes a greater force on one arm of the soot chain aggregate than on another arm, causing the soot chain to begin to fold.

The interaction of the atmospheric gas, the condensate, and the soot spherules is further simplified by approximating the shapes in 2D. Figure C.3 shows a drawing of this simplification and conceptualizes how the soot chain might become compacted with time as the condensate, the liquid embryo, develops in a crevasse between two of the soot spherules.

The liquid embryo seeks a lower surface free energy as its size increases. The embryo's movement is assumed to cause a greater force on one arm of the soot chain aggregate than on another arm, causing the soot chain to begin to fold (*Khalizov et al.*, 2009; *Weingartner et al.*, 1995).

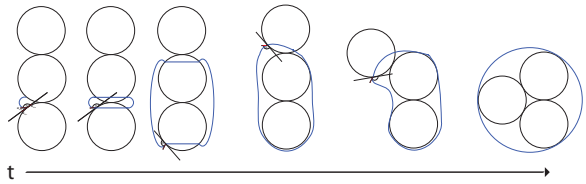


Figure C.3: The evolution of a simplified 2D soot chain with one arm under an increasing liquid embryo (blue). A tangent line to the embryo and soot spherule surface has been drawn.

### C.2.2 Derivation of an Euler-Lagrange Model

An alternative approach for describing the soot chain compaction was attempted through the use of Lagrangian Mechanics. The Euler-Lagrange equation can be written as

$$\frac{d}{dt}\left(\frac{\partial L}{\partial \dot{q}_j}\right) - \frac{\partial L}{\partial q_j} = 0, \tag{C.1}$$

where $L = T - V$ (i.e., the kinetic energy, $T$, minus the potential energy $V$) is the Lagrangian, and $q_j$ and $\dot{q}_j$ represent the generalized coordinates and their time derivative.

Two soot spherules were isolated for their movement from the entire soot chain. The two spherules were initially assumed to be vertically aligned and touching. The upper soot spherule is constrained to move in a circle on the surface of the soot spherule beneath it. The soot spherule in motion will not roll or spin down the surface beneath it; it will only slide. It is assumed the soot spherule has no initial kinetic energy, and the potential energy will be stored in the surface tension from the liquid. The origin of the coordinate system will be the center of the lower soot spherule. The equations to describe the motion of the upper soot spherule are given by $x = R\cos\theta$ and $y = R\sin\theta$ where $R$ is the radius of one

soot spherule and $\theta$ is the generalized coordinate is $\theta$. The system then has one degree of freedom. The kinetic energy term then becomes

$$T = \frac{m}{2}\left(\dot{x}^2 + \dot{y}^2\right) = \frac{1}{2}mR^2\dot{\theta}^2, \tag{C.2}$$

where $m$ is the mass of one soot spherule.

The potential energy was assumed to be a function of the surface tension of the liquid, $\sigma$, accumulated on the surface. The surface tension is assumed to be a function of the position of the spherule in motion. Thus, $V = V(\sigma(y,\theta))$. [1] Because the work is done by the liquid's surface tension, the potential energy is given by $V = -\sigma(R\theta)(y\sin\theta)$.

The Euler-Lagrange equation for this system becomes

$$\frac{d}{dt}\left(\frac{\partial L}{\partial \dot{\theta}}\right) - \frac{\partial L}{\partial \theta} = mR^2\ddot{\theta} - \sigma y R\sin\theta - \sigma y R\theta\cos\theta. \tag{C.3}$$

Setting Equation C.3 equal to zero and solving for $\ddot{\theta}$, gives

$$\ddot{\theta} \;=\; \left(\frac{\sigma y}{mR}\right)(\sin\theta + \theta\cos\theta). \tag{C.4}$$

To first order, the position of the sliding soot spherule with respect to time should be linear assuming $\sigma$, $y$, $R$, and $m$ are constants. Equation (C.4) can be discretized and solved numerically using finite difference. For a time step of $\Delta t$, the position of the upper soot spherule at a time $n+1$ can be found by integrating the finite difference equation given by

$$\theta^{n+1} = (\Delta t)^2\left(\frac{\sigma y}{mR}\right)(\sin\theta + \theta\cos\theta)) + 2\theta^n - \theta^{n-1}. \tag{C.5}$$

[1] Analogously, if gravity were the potential energy these were two macroscopic balls, then $V = -mgy\sin\theta$.

### C.2.3 Results of the Euler-Lagrange Model

The parameters used in Equation are as follows. The radius of the soot spherules can range from 5 to 25 nm (*Khalizov et al.*, 2009; *Smith*, 1982; *Zhang et al.*, 2008). Thus the soot spherule radius used in these calculations is $R$ =20 nm. The primary component in the composition of soot is elemental carbon which has a density of 2.62 g cm$^{-3}$ at 293 K. From the density and the radius, the mass of soot spherules, $m$, was calculated to be 8.78 x 10$^{-20}$ kg. The value for the surface tension, $\sigma$, of the liquid accumulated in the crevasse is assumed to be constant. The magnitude of the surface tension can vary depending on the composition of the accumulated gas in the surface. Electrolyte solutions with concentrations ranging from 0 - 9 mole kg$^{-1}$ have surface tension values ranging from $\sigma$ = 72.0 - 94.0 erg cm$^{-2}$ (*Pruppacher and Klett*, 1997). This range of $\sigma$ was tested and found to change the results insignificantly.

A variable $y$ was defined to be the distance from the origin of the coordinate system (the center of the lower soot spherule) to the center of mass of top soot sphere with an initial length equal to $2R$. As the upper soot spherule moves, this distance becomes $y = 2Rsin(\theta)$ and is updated every step in the iteration. A time step of $\Delta t = 1$ ns was chosen. This made the terms in Equation C.2.3 no more than two orders of magnitude different when the initial conditions of position were set to near-zero values. This was done because we wanted the initial movement of the soot spherule to be caused by the liquid's surface tension. Thus, the positions of the spherule were initialized to to be $\theta = 0.0$ at $n = 1$ and $\theta = 1$ x 10$^{-3}$ at $n = 2$. Equation C.2.3 was integrated numerically until the upper soot spherule moved 90 degrees from its initial position.

Figure C.4 plots the position of the upper soot spherule moving along the surface of the lower soot spherule in time from the integration of Equation C.2.3. The upper soot spherule moved 90 degrees in an unrealistic 75 ns. TEM images of soot aggregates show many soot spherules comprising an arm of the soot chain (*Zhang et al.*, 2008). The integration was repeated a second time for an arm of 100 soot spherules in synchronous movement upon

the top of a single soot spherule. The mass of the moving soot spherule was increased 100 times to reflect these additional soot particles and the center-of-mass of the moving soot arm was moved to $10\times R$ from the stationary soot spherule. Their movement as in time is also shown in C.2.3(b). It took 210 ns for the arm of soot spherules to move 90 degrees from the initial position, which is an increase the one soot spherule integration. The results are still unrealistic.

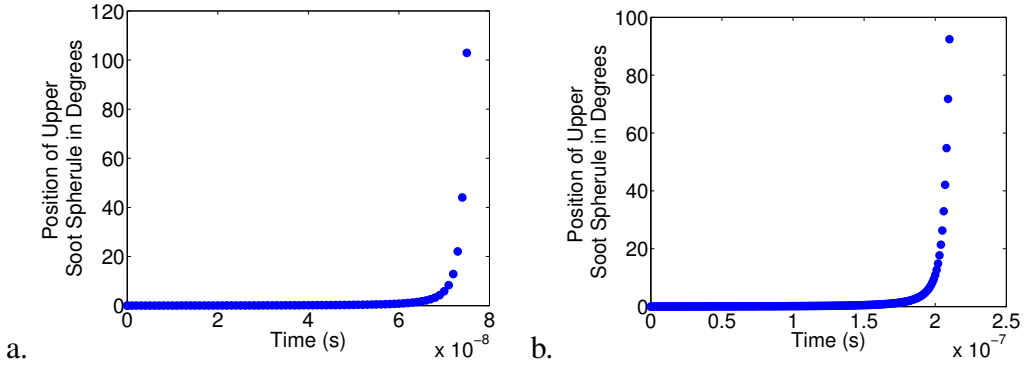


Table C.1: (a) Soot chain angle displacement with one soot spherule and (b) soot chain displacement with 100 soot spherules in the moving soot chain arm from the integration of Equation C.2.3.

The Euler-Lagrange's model is not realistic of soot chain compaction, even though it is unknown how quickly the soot chain arms fold into an aggregate. The sudden movement of the soot spherules as predicted in Figures C.4 suggests the compaction of the soot agglomerates happens quickly. In nature, the soot agglomerates have multiple arms which might interfere with the speed of the compaction. It was observed in a laboratory experiments by *Zhang et al.* (2008) and *Khalizov et al.* (2009) where the soot agglomerates were exposed to sulfuric acid for 12 seconds that soot chain compaction occurred sometime in those 12 seconds. One reason as to why this first calculation might not be representative of real soot chain compaction is with the assumed surface tension of the accumulated liquid in the crevasse. A more realistic approach to the finding the surface tension of the liquid cap in the crevasse would be to initialize the soot chain with no liquid accumulation on the surface. A concentration of the surrounding gas could be given, then a deposition rate onto the surface

of the soot could be calculated. After a threshold of the gas had accumulated on the surface, the capillary effect of the liquid could pull the soot chain into a more compact form. This calculation could be performed by consulting the developed theory of nucleation in a crevasse found in *Pruppacher and Klett* (1997). In addition to including gas dynamics, the model could be improved by re-deriving the equation of motion to include viscosity, a dynamic property of the liquid, instead of surface tension, a static property of the liquid. *Adachi et al.* (2010) shows that soot exposed to high (low) viscosity matter results in a particle with little (increases) change in fractal dimension. The viscosity of sulfuric acid is 2.42 $\times 10^{-2}$ Pa $\cdot$ s while water's viscosity is 8.94$\times 10^{-4}$ Pa $\cdot$ s at 25 C.

### C.2.4 Derivation of the Newtonian Model

The second model of soot spherule movement starts from with the equations derived by *Seinfeld and Pandis* (2006) for the dynamics of a single aerosol particle in a fluid. We assume the particle motion, $\mathbf{v}$, arises from some external forces, $\mathbf{F_i}$, acting on the particle.

$$m_p \frac{d\mathbf{v}}{dt} = \sum_{i=1}^{n} \mathbf{F_i} \tag{C.6}$$

We use Stokes' Law because it is an accurate solution to the equations of continuum mechanics for the drag exerted by the air for particles smaller than 20 $\mu$m. For a soot spherule, these external forces are gravity, $\mathbf{g}$, and fluid drag force arising once a difference between velocity of soot spherule and velocity of the fluid exists,

$$m_p \frac{d\mathbf{v}}{dt} = m_p \mathbf{g} + \frac{3\pi\mu D_p}{C_c}(\mathbf{u} - \mathbf{v}), \tag{C.7}$$

where the corrected Stokes drag force on the particle is used and the particle is moving with velocity $\mathbf{v}$ in a fluid having velocity $\mathbf{u}$. The slip correction factor, $C_c$, is introduced

into Stokes' law to account for the size of the particle approaching the same magnitude as the mean free path of the air because the drag force becomes smaller. To use the corrected Stokes drag means we assume the soot spherule's acceleration is slow. The correction term is given by

$$C_c = 1 + \frac{2\lambda}{D_p}\left[1.257 + 0.4\exp\left(-\frac{1.1D_p}{2\lambda}\right)\right] \tag{C.8}$$

For a 20 nm particle, a value of $C_c$ =11.4 was used (*Seinfeld and Pandis*, 2006). We then let $\mathbf{v} = R\dot{\theta}\hat{\theta}$ and assume the particle is in a quiescent fluid ($\mathbf{u} = 0$) and starts with zero velocity. The gravity term becomes $\mathbf{g} = g_z\hat{\mathbf{z}} = g_r\cos\theta\hat{\mathbf{r}} - g_\theta\sin\theta\hat{\theta}$. The surface tension, $\sigma$, is multiplied by a length vector, $\mathbf{L}$ to be included as an external force.

$$\frac{d\dot{\theta}}{dt} = -\frac{2g\sin\theta}{D_p} - \frac{3\pi\mu D_p}{m_p C_c}\dot{\theta} - \frac{2\sigma}{m_p D_p}\mathbf{L} \tag{C.9}$$

In assessing the magnitude of the terms in Equation C.9, the surface tension term is much larger than the other terms. Additionally, if the volume of the condensed gas in the crevasse between the two spherules is unchanging and constant, the spherical cap might not pull the spherules together but rather keep them from moving with respect to each other. Another force must be influencing the spherule movement. In the Euler-Lagrange Model, the spherules were considered macroscopic with respect to the air molecules in which they moved. The inclusion of Stoke's law in Equation C.9 recognizes the effect of drag exerted by the air molecules on the spherule as it moves.

The last external force considered is the Coulomb force. The spherules are stuck together by an attractive force. The finite difference equation for soot spherule movement becomes

$$\theta^{n+1} = \frac{2\theta^n - \theta^{n-1} - \frac{g}{a}\sin\theta^n(\Delta t)^2 + \frac{6\pi\mu a}{mC_c}\theta^n\Delta t + \frac{kq_1q_2}{r^2}(\Delta t)^2}{(1. + 6\pi\mu a\ \Delta t)/(mC_c)} \tag{C.10}$$

### C.2.5 Results of the Newtonian Model

The same values used in the Euler-Lagrange Model for mass, $m$, radius, $R$, and $y$ are used here in the Newtonian Model. The distance between the center of mass of the spherules was assumed to be $10^{-9}$m, and the product of the charges of the soot spherules was assumed to be $10^{-19}$. The of air $\mu_{air}$ = 1.8e-5 kg/m/s at 1 atm and 298K. The initial displacement of $\theta$ at $n$ and $n+1$ was set to zero.

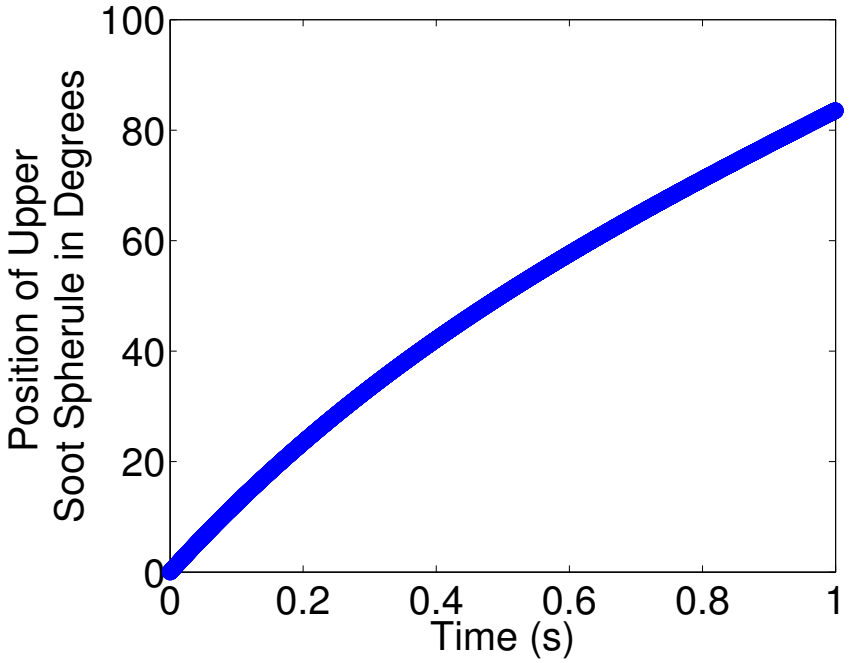


Figure C.4: Soot chain angle displacement with one soot spherule from the integration of Equation C.10.

The movement in Figure C.4 is taken to be a more realistic solution. The integration of Equation C.10 is not sensitive to the time step chosen. The solution is highly sensitive to the assumed charge and distance between the center of masses of the two spherules.

## C.3 Discussion and Summary

Soot chains are formed from freshly combusted material. These chains have complex structures on which gases have been observed to deposit on the surface. The deposition of these gases on the surface causes the soot chains to compress into a shape with a smaller aerodynamic diameter and density. A simple model based on the assumption that the motion of the spherules stems from external forces has been derived that predicts how quickly the soot chain will compress. The model's results are within the bounds of measurements and is highly sensitive to the assumed charge of the soot spherules. This assumption should be further explored in later studies. A purely mechanical model did not realistically predict soot spherule movement. It was found that aspects of fluid dynamics, electrostatics, and chemical interactions were necessary to produce realistic results.

This model assumes the soot chain will compress. However, not every measured soot agglomerate is compacted, either. *Adachi et al.* (2010) found soot aerosols remaining in the chain-like structure and not lying at the center of their host material. This is attributed to the coating being highly viscous and opposing movement of the soot agglomerate's arms. *Khalizov et al.* (2009) coated the soot chains with sulfuric acid, a low-viscoscity material, and all the soot chains in their experiment were compacted. Further application of this model would consider the composition of the condensing gas to understand the effect on compaction. Results from this model could be used to reassess the potential of freshly-emitted soot to become sources for cloud hydrometeors.

# APPENDIX D

# Publication of "Can global models ignore the chemical composition of aerosols?"

# Can global models ignore the chemical composition of aerosols?

E. L. Roesler[1] and J. E. Penner[1]

Received 9 August 2010; revised 22 October 2010; accepted 2 November 2010; published 24 December 2010.

[1] The number of cloud droplets formed from a population of aerosols depends on the aerosol number concentration, $N_A$, the size distribution, and the chemical composition. The cloud albedo effect occurs when increasing $N_A$ causes increases to the droplet concentration, $N_D$. We examined the effects of changing aerosol size, composition, and number on $N_D$ within the United States. We found that changing the water-soluble organic carbon (WSOC) fraction from 50% to 0.05% in the fine mode aerosol and from 50% to 95% in the coarse mode aerosol decreased $N_D$ by an average of 34%. Our results show that the changes to the aerosol composition cause over a 20% change to $N_D$, a magnitude previously estimated to cause a 1 W m$^{-2}$ change in radiative forcing. Given the realistic range of aerosol compositions used here, it is not possible for global models to correctly calculate the cloud albedo effect if composition is ignored. **Citation:** Roesler, E. L., and J. E. Penner (2010), Can global models ignore the chemical composition of aerosols?, *Geophys. Res. Lett.*, *37*, L24809, doi:10.1029/2010GL044282.

## 1. Introduction

[2] The largest uncertainty in climate change forcing [*Forster et al.*, 2007] is the cloud albedo effect. Global models use empirical relationships based on regional studies or mechanistic activation schemes to calculate $N_D$ [e.g., *Pringle et al.*, 2009]. A focus of current research is to understand which microphysical variables have dominant roles, thereby eliminating the need for global models to keep unnecessary variables. For example, previous studies have shown that aerosol microphysical variables such as size, number, and small concentrations of coarse mode aerosols in a population of fine mode aerosols dominate in the prediction of $N_D$ [*Chen and Penner*, 2005; *Dusek et al.*, 2006; *Feingold et al.*, 1999; *Feingold*, 2003]. Other studies have shown crustal and organic aerosols also influence $N_D$ [*Ervens et al.*, 2005; *Kelly et al.*, 2007; *Nenes et al.*, 2002]. Based on these studies, we changed the microphysical variables in a warm microphysics model to identify which variables changed $N_D$ by 10–20%. These limits of change in $N_D$ were chosen because a decrease in radiative forcing of −1 W m$^{-2}$ has been estimated if $N_D$ is increased by 20% [*Facchini et al.*, 1999].

## 2. Model Description and Input Parameters

[3] We used the Parcel Undergoing Thermodynamic Transitions (PUTT), a warm microphysics model [*Seidl*, 1989]. The initial relative humidity of the parcel was 98% and was lifted adiabatically 300 meters from an initial starting pressure of 900 mbars at a speed, $w$, of 10, 20, 50, 150, or 300 cm s$^{-1}$. The size distribution of the aerosols was modeled as the sum of two lognormal functions each discretized into ninety bins.

[4] The Interagency Monitoring of Protected Visual Environments (IMPROVE) network dataset was used to create the aerosol composition (IMPROVE, IMPROVE Archived Data, 2007, available at http://vista.cira.colostate.edu/improve). The dataset includes 187 sites within the continental United States, Alaska, Hawaii, and the U.S. Virgin Islands (see Figure 1a). Particulate matter monitoring has occurred at some but not all sites from 1988 to 2004. The data was averaged into four seasons for each of the 28 regions listed by *Malm et al.* [1994].

[5] PUTT also calculates the absorption of nitric acid gas, $HNO_{3(g)}$, into the aerosol particles. The parcel's initial gas-phase nitrate concentrations, 0.01 to 31.3 ppbv, were derived from the model results of *Feng and Penner* [2007] for each region and season. *Feng and Penner* [2007] found the model overpredicted the observations in North America. A constant value of 0.2 ppbv for each region and season, which would have given better agreement with the observations, was used in a sensitivity test.

[6] The predicted values for $N_D$ have different responses to internal and external aerosol mixtures [*McFiggans et al.*, 2006], and small concentrations of large aerosols can greatly affect $N_D$ as well as the formation of precipitation [*Feingold et al.*, 1999]. The IMPROVE dataset does not provide the coarse mode $PM_{10.0}$ aerosol composition, size distribution parameters, or the mixing state of the fine and coarse mode aerosols. Measurements taken near the Owens (dry) Lake, a saline playa with large and frequent dust storms in the spring and fall [*Labban et al.*, 2004], were used to constrain the coarse mode aerosol parameters. The composition of the fine mode was similar to the coarse mode aerosols [*Labban et al.*, 2004]. The fine mode composition in the IMPROVE regions affected by Owens (dry) Lake dust storms was also similar to the fine mode measurements by *Labban et al.* [2004]. It was assumed that the fine and coarse mode compositions were equal for these regions in PUTT. Relevant measurements were not available for the composition of the coarse mode for the remainder of the regions. All regions were then assumed to have the same fine and coarse mode composition. This assumption was tested with sensitivity tests where differing fine and coarse mode compositions were used. We assumed the IMPROVE data, when averaged, was an aged background aerosol composition, so external mixtures were not used.

[7] A large component of the fine aerosol mass in the IMPROVE network is organic carbon (OC), but the fraction of OC that is water-soluble is not given [*Malm et al.*, 1994, 2004]. We assumed 50% of the OC was WSOC. Measurements have found WSOC fractions in this range [*Lowenthal*

[1]Department of Atmospheric, Oceanic, and Space Sciences, University of Michigan, Ann Arbor, Michigan, USA.


0094-8276/10/2010GL044282

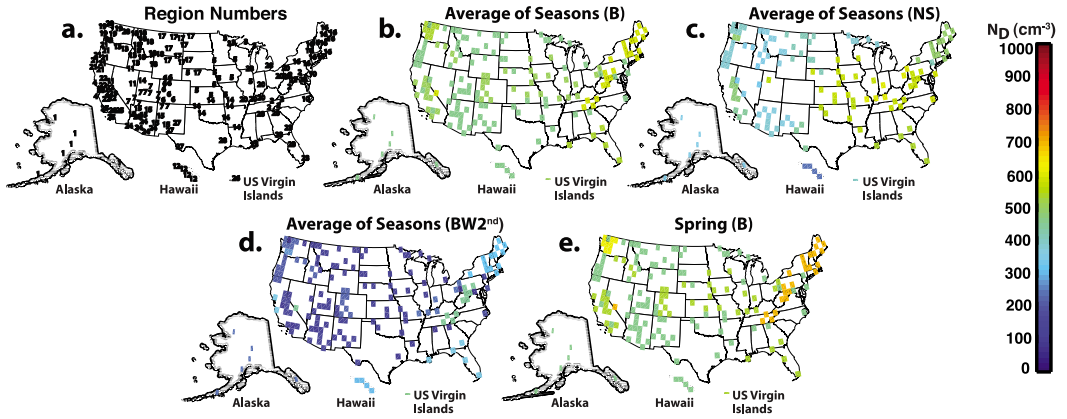


**Figure 1.** (a) The 28 regions created from the 187 IMPROVE network locations. (b) Droplet concentration, $N_D$ (cm$^{-3}$) for $w$ = 20 cm s$^{-1}$ average of seasons for case B. (c) Same as Figure 1b but with case NS. (d) Same as Figure 1b but with case BW2nd. (e) Same as Figure 1b but with the spring season compositions.

*et al.*, 2009; *Pio et al.*, 2007]. Sensitivity tests also examine this assumption.

[8] Values for the van't Hoff factor, molecular weight, density, charge, and soluble fraction of OC were needed for the WSOC. *Ervens et al.* [2005] suggested that a van't Hoff factor of one produced the lowest error in predicting $N_D$, and *Mircea et al.* [2005] showed that the average predicted $N_D$ was 20% smaller than the measured $N_D$ when the organics were assumed undissociated. *Ervens et al.* [2005] also found that high molecular weight species (M > 400 g mol$^{-1}$) influence droplet concentrations. For simplicity, we assumed the WSOC had a molecular weight of 50 grams mol$^{-1}$, a van't Hoff factor of one, a density of 2.0 grams cm$^{-3}$, and carried no charge.

[9] Two parameterizations of surface tension, $\sigma_T$, were compared in this study. *Mircea et al.*'s [2005] parameterization and treating $\sigma_T$ as the sum of the multi-component aqueous solution [e.g., *Topping et al.*, 2007]. PUTT's treatment of $\sigma_T$ had previously accounted for only the inorganic aerosol components [*Seidl*, 1989]. We included values of surface tension as a function of WSOC taken under a variety of atmospheric conditions (i.e., polluted continental, remote continental, biomass burning conditions, and wet-season) [*Facchini et al.*, 1999, 2000; *Mircea et al.*, 2005].

## 3. Description of Sensitivity Cases

[10] Table 1 lists the base cases and test cases we considered. B, N, and NS are the base cases to which other cases are compared. The base cases use the aerosol compositions created from IMPROVE and are different in $N_A$ and $\sigma_g$. Any cases not marked with an S use a geometric standard deviation and mode radius fit to the size distribution of *Dusek et al.* [2006] in the fine mode ($\sigma_{g,f}$ = 1.5) and of *Niemeyer et al.* [1999] for the coarse mode ($\sigma_{g,c}$ = 1.5). Cases marked with an S use $\sigma_{g,f}$ = 2.0 and $\sigma_{g,c}$ = 3.5. For cases 1, 3–12, and 21, $N_A$ was calculated for each region from the measured mass concentration in IMPROVE. For cases 2 and 13–20, all regions have a fine and coarse mode number concentration of $N_{A,f}$ = 1000 cm$^{-3}$ and $N_{A,c}$ = 0.75 cm$^{-3}$, respectively, based on typical continental $N_A$ values [*Seinfeld and Pandis*, 2006]. For all cases, the fine mode and coarse mode radii are 0.03 $\mu$m and 0.3 $\mu$m, respectively.

[11] Cases marked with a G assume $[HNO_3]_{(g)}$ = 0.2 ppbv in every region, otherwise results from *Feng and Penner* [2007] were used. Cases marked with a C used a simplified composition of 6% $H^+$, 48% $SO_4^{--}$, 20% WSOC, and 26% insoluble components in every region, derived from a correlation of the droplet numbers with each component of the composition over all regions and vertical velocities in cases B, BS, and BG. Surface tension was calculated using *Mircea et al.*'s [2005] parameterization, but cases marked st calculate $\sigma_T$ as the sum of the multi-component aqueous solution. Cases marked ln1 used only the fine mode mass and concentration to explore how neglecting the course mode mass would affect $N_D$. Cases marked H assumed that a gas-aerosol nitric acid equilibrium is not achieved prior to updraft. For all simulations, the accommodation coefficient for $[HNO_3]_{(g)}$ was equal to 0.05 [*Xue et al.*, 2005]. There is uncertainty in the value of the water vapor accommodation coefficient, $\alpha$ [*McFiggans et al.*, 2006]. Cases labeled A set $\alpha$ to 1.0 instead of 0.1. Cases labeled Win assume 50% and 0.05% of the OC in the fine and coarse modes, respectively, is WSOC. Cases labeled W2nd assume 0.05% and 95% of the OC in the fine and coarse modes, respectively, is WSOC. Cases Win and W2nd test ranges of measured WSOC fractions [*Lowenthal et al.*, 2009; *Pio et al.*, 2007].

## 4. Case and Regional Comparisons of $N_D$

[12] Table 1 lists the average difference between each test case and base case normalized by the mean of the base case. Mean droplet number increases with vertical velocity. The largest differences in absolute percentage values for base case B is that with test cases N and BW2nd. The largest differences in absolute percentage values for base case NS is that with test cases N and NSW2nd. An average increase in $N_A$ in test case N creates more droplets than in base cases B and NS. In cases BW2nd and NSW2nd, the amount of

**Table 1.** Base Cases N, NS, and B and Descriptions of Each Test Case[a]

| Description of Changed Microphysical Variable of Test Case From Base Case[b] | $\frac{\text{Mean of } (N_{Di,test} - N_{Di,base})}{\text{Mean of } (N_{D,base})} \times 100\%$; and Mean of $N_{D,test}$ in $cm^{-3}$ | | | | |
|---|---|---|---|---|---|
| | 10 cm/s | 20 cm/s | 50 cm/s | 150 cm/s | 300 cm/s |
| *Case N: $N_A$ Calculated Regionally From IMPROVE* | | | | | |
| 1. Changing size distribution to $\sigma_{g,f} = 2.0$ and $\sigma_{g,c} = 3.5$ **NS** | −33.9%, 250 | −43.3%, 438 | −53.2%, 850 | −64.7%, 1588 | −68.8%, 2047 |
| 2. Changing to $N_A$ constant in every region, $N_{A,f} = 1000$ $cm^{-3}$, $N_{A,c} = 0.75$ $cm^{-3}$ **B** | −27.8%, 273 | −36.7%, 495 | −53.7%, 841 | −77.2%, −991 | −84.8%, 997 |
| 3. Changing to constant nitric acid concentration of $[HNO_3]_{(g)}$ = 0.2 ppbv **NG** | −2.7%, 369 | −2.7%, 762 | −3.1%, 1760 | −1.5%, 4283 | −0.5%, 6519 |
| 4. Changing to constant composition of 6% $H^+$, 48% $SO_4^{--}$, 20% WSOC, 26% Insol. **NC** | 11.9%, 421 | 7.9%, 808 | 7.8%, 1845 | 4%, 4128 | 4%, 6409 |
| *Case NS: $N_A$ Calculated Regionally From IMPROVE With $\sigma_{g,f} = 2.0$, $\sigma_{g,c} = 3.5$* | | | | | |
| 5. Less WSOC (0.05%) in fine mode and more WSOC (95%) in coarse mode **NSW2**nd | −29.8%, 188 | −31.7%, 317 | −36.4%, 621 | −37.7%, 1207 | −35.1%, 1748 |
| 6. Changing accommodation coefficient to 1.0 from 0.1 **NSA** | −4.9%, 238 | −7.5%, 405 | −10.2%, 764 | −9.3%, 1441 | −7.6%, 1892 |
| 7. Not calculating surface tension from WSOC **NSst** | −1.8%, 246 | −3%, 425 | −3%, 825 | −1.8%, 1560 | −1.1%, 2025 |
| 8. Less WSOC (0.05%) in coarse mode **NSWin** | 0.8%, 253 | 1.1%, 434 | t 0.7%, 856 | 0.1%, 1590 | 0.2%, 2051 |
| 9. Changing to using only the fine mode **NSln1** | 0.8%, 253 | 1%, 434 | 0.7%, 856 | 0.2%, 1590 | 0.7%, 2054 |
| 10. Changing nitric acid equilibrium prior to uplift **NSH** | 2.2%, 255 | 3.8%, 446 | 4.3%, 887 | 3.8%, 1649 | 2.4%, 2097 |
| 11. Changing to constant composition of 6% $H^+$, 48% $SO_4^{--}$, 20% WSOC, 26% Insol. **NSC** | 4.2%, 233 | 3.8%, 402 | 1%, 788 | 1.1%, 1552 | 0.4%, 2054 |
| 12. Changing size distribution to $\sigma_{g,f} = 1.5$ and $\sigma_{g,c} = 1.5$ **N** | 51.3%, 379 | 76.3%, 783 | 114%, 1817 | 183%, 4349 | 220%, 6551 |
| *Case B: $N_A$ Constant Regionally, $N_{A,f} = 1000$ $cm^{-3}$, $N_{A,c} = 0.75$ $cm^{-3}$* | | | | | |
| 13. Less WSOC (0.05%) in fine mode and more WSOC (95%) in coarse mode **BW2**nd | −47.2%, 144 | −53.5%, 230 | −55.1%, 377 | −39.8%, 597 | −24.9%, 749 |
| 14. Changing size distribution to $\sigma_{g,f} = 2.0$ and $\sigma_{g,c} = 3.5$ **BS** | −29.9%, 191 | −30.8%, 342 | −27%, 614 | −10.3%, 889 | −5.5%, 943 |
| 15. Changing to constant nitric acid concentration of $[HNO_3]_{(g)}$ = 0.2 ppbv **BG** | −10.4%, 244 | −6.7%, 462 | −3.2%, 814 | −0.3%, 989 | −0%, 997 |
| 16. Changing accommodation coefficient to 1.0 from 0.1 **BA** | −4.4%, 261 | −8.4%, 453 | −6.8%, 784 | −1.5%, 976 | −0.1%, 996 |
| 17. Changing to constant composition of 6% $H^+$, 48% $SO_4^{--}$, 20% WSOC, 26% Insol. **BC** | 2.9%, 281 | −1.4%, 488 | 0.2%, 842 | 0.5%, 996 | 0%, 997 |
| 18. Changing nitric acid equilibrium prior to uplift **BH** | 5.6%, 286 | 2.6%, 504 | 2.2%, 860 | 0.1%, 992 | 0%, 997 |
| 19. Less WSOC (0.05%) in coarse mode **BWin** | 8.5%, 294 | 0.4%, 497 | 0.9%, 849 | 0.1%, 992 | 0%, 997 |
| 20. Changing to using only the fine mode **Bln1** | 9.7%, 297 | 0.6%, 498 | 1%, 850 | 0%, 991 | −0.1%, 997 |
| 21. Calculating aerosol number concentration based on IMPROVE mass concentration **N** | 38.4%, 379 | 58%, 783 | 116%, 1817 | 339%, 4349 | 557%, 6551 |

[a]The five columns from the right list the mean of the difference of $N_D$ in the ith region of the test case from the base case normalized by mean of $N_D$ for all regions in the base case. The mean $N_D$ in $cm^{-3}$ of all regions for each test case is listed after the percentage.
[b]Test case acronym is listed in bold.

soluble mass was decreased in the fine mode and increased in the coarse mode causing the larger, but fewer, more soluble aerosols to form droplets at the expense of the smaller, more numerous, less soluble fine mode aerosols. The third largest difference for $N_D$ for base case B is with test case BS. This is due to the increased width of the size distribution and higher concentration of large-radii aerosols forming droplets at the expense of the small-radii aerosols. The remainder of the sensitivity tests did not have average differences greater than 20% for $N_D$ between the base cases and test cases.

[13] The inter-regional variation (standard deviation divided by the mean $N_D$) shows how the changes in composition between regions or changes in the microphysical variables affect $N_D$. A high inter-regional variation value of $N_D$ for a case implies an empirical relationship of $N_D$ based on a region's value would not be accurate if applied to other regions. Figures 1b–1e show $N_D$ ($cm^{-3}$) in every region for a subset of the test cases from Table 1. Changes in composition between regions cause an inter-regional variation in $N_D$ of 8% when all the seasons are averaged (Figure 1b), and a 15% variation of $N_D$ in the spring (Figure 1e). The mean $N_D$ is increased by 6% to 534 $cm^{-3}$ in spring compared to the annual average mostly due to a factor-of-two average increase in $[HNO_3]_{(g)}$. The $N_D$ in spring is increased by 20% along the eastern U.S. in regions 2 and 16 primarily due to an average increase in $[HNO_3]_{(g)}$ from 13 to 26 ppbv. The $N_D$ in regions 8, 9, and 19 also increased by 15% due to the increase in $[HNO_3]_{(g)}$ from 7 to 14 ppbv. Changes to the composition caused changes to $N_D$ within and between regions by 10–20%.

[14] The annual average of $N_D$ for base case NS, shown in Figure 1c, has the same aerosol composition as the annual average of base case B (Figure 1b), and $N_A$ is also unique in every region which causes an inter-regional variation of 48%. The average $N_D$ decreased by 12% compared to case B due to an average decrease in $N_A$ in case NS. Figure 1d shows the BW2nd case which has the largest inter-regional variation of 60%. From Table 1, case BS has the third largest average difference in $N_D$ from base case B but has a negligible inter-regional variation (not shown in Figure 1). This is due to the increased width of the size distribution and higher concentration of large-radii aerosols forming droplets at the expense of the small-radii aerosols.

## 5. Changes to $N_D$ for Different $S_{max}$

[15] Figure 2 shows the computed $N_D$ at the maximum supersaturation, $S_{max}$, for test cases 5–12 against base case

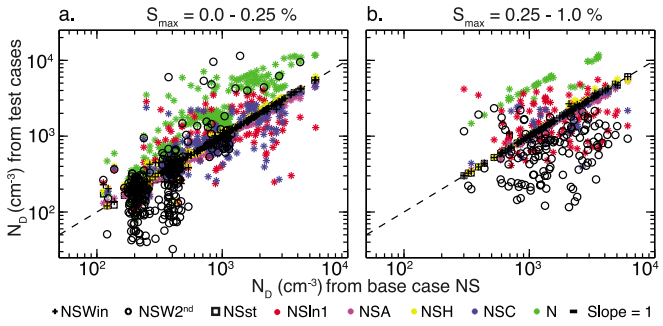


**Figure 2.** Scatter plots of droplet concentration, $N_D$, of all seasons and regions at the parcel's $S_{max}$ for different test cases compared to the base case NS in two maximum supersaturation ($S_{max}$) ranges. (a) $S_{max}$ range, 0.0–0.25%. Cases NSW2nd, NSln1, NSC, N, and NSA have correlations of 0.69, 0.72, 0.87, 0.88, and 1.0 with slopes of 2.34, 0.70, 0.79, 2.42, and 0.85, respectively. (b) $S_{max}$ range, 0.25–1.0%. Cases NSW2nd, NSln1, NSC, N, and NSA and have correlations of 0.23, 0.28, 0.83, 0.93, and 1.0 with slopes of 0.12, 0.28, 0.73, 2.59, and 0.85, respectively. In both Figures 2a and 2b, cases NSH, NSst, and NSWin have correlations of ~1.0 with slopes of ~1.0.

NS separated into two $S_{max}$ ranges. This was done to examine whether a parameterization of the base case that is a function of $S_{max}$ and $N_A$ could be used. Slopes of best-fit lines and correlation coefficients were calculated and are reported in the caption. A test case that has a low correlation with the base case NS suggests an empirical relationship formed from the base case would not correctly predict $N_D$.

[16] For both the low and high ranges of $S_{max}$, cases NSH, NSst, and NSWin have slopes and correlations of ~1.0. This indicates that a parameterization would not need to include changes in the gas-aerosol equilibrium of nitric acid prior to updraft, the parameterization of surface tension, or a small concentration of coarse-mode aerosols with less soluble mass. In both the low and high ranges of $S_{max}$, cases NSC, N, and NSA all have correlation coefficients greater than 0.83 with slopes that range from 0.73 to 2.60. If a parameterization that is based on simplified composition or inaccurate $N_A$ and $\sigma_g$ is applied, then the calculated average $N_D$ and cloud albedo effect will also be inaccurate. Case NSln1 shows a correlation and slope of ~0.70 at low $S_{max}$, but a correlation and slope of 0.28 at high $S_{max}$. For the low and high ranges of $S_{max}$, NSW2nd has correlations and slopes much different from 1.0. Thus an empirical relationship that is based on aerosol parameters similar to case NS could not correctly calculate $N_D$ if applied to other regions that had a different number of modes or amount of soluble material.

## 6. Conclusions

[17] Measurements of aerosols in Europe have shown that the aerosol size distribution mostly determines the aerosol's ability to become a cloud droplet [*Dusek et al.*, 2006]. In this study, it was found that the aerosol size distribution and composition cannot be ignored by global models when calculating the $N_D$ for the cloud albedo, which is based aerosol compositions measured in the United States from 1988 to 2004. These results are based on assumptions regarding the size-resolved and physicochemical properties of WSOC. Changing these assumptions would affect $N_D$, and further sensitivity studies could identify which WSOC properties were most important for modeling. A global model using an empirical relationship based on regional measurements could over- or under-predict $N_D$ when applied to other regions depending on differences in composition, the number of log-normal modes, $N_A$, and $\sigma_g$. Regional and seasonal differences in trace gas concentrations, organic, inorganic, and insoluble aerosol compositions cause high variability in $N_D$, suggesting a more thorough treatment and not a simplification of aerosol composition is needed for an accurate prediction of $N_D$.

[18] **Acknowledgments.** We thank Yang Chen for his contributions to PUTT. E.L. Roesler is funded by GREF within the DOE. The ARM Program provided partial support for this study through grant DOE-DE-FG02-97-ER62370.

## References

Chen, Y., and J. E. Penner (2005), Uncertainty analysis for estimates of the first indirect aerosol effect, *Atmos. Chem. Phys.*, *5*, 2935–2948.

Dusek, U., et al. (2006), Size matters more than chemistry for cloud-nucleating ability of aerosol particles, *Science*, *312*(5778), 1375–1378.

Ervens, B., G. Feingold, and S. M. Kreidenweis (2005), Influence of water-soluble organic carbon on cloud drop number concentration, *J. Geophys. Res.*, *110*, D18211, doi:10.1029/2004JD005634.

Facchini, M. C., M. Mircea, S. Fuzzi, and R. J. Charlson (1999), Cloud albedo enhancement by surface-active organic solutes in growing droplets, *Nature*, *401*(6750), 257–259.

Facchini, M. C., S. Decesari, M. Mircea, S. Fuzzi, and G. Loglio (2000), Surface tension of atmospheric wet aerosol and cloud/fog droplets in relation to their organic carbon content and chemical composition, *Atmos. Environ.*, *34*(28), 4853–4857.

Feingold, G. (2003), Modeling of the first indirect effect: Analysis of measurement requirements, *Geophys. Res. Lett.*, *30*(19), 1997, doi:10.1029/2003GL017967.

Feingold, G., W. R. Cotton, S. M. Kreidenweis, and J. T. Davis (1999), The impact of giant cloud condensation nuclei on drizzle formation in stratocumulus: Implications for cloud radiative properties, *J. Atmos. Sci.*, *56*(24), 4100–4117.

Feng, Y. and J. E. Penner (2007), Global modeling of nitrate and ammonium: Interaction of aerosols and tropospheric chemistry, *J. Geophys. Res.*, *112*, D01304, doi:10.1029/2005JD006404.

Forster, P., et al. (2007), Changes in atmospheric constituents and in radiative forcing, in *Climate Change 2007: The Physical Science Basis. Contribution of Working Group I to the Fourth Assessment Report of the Intergovernmental Panel on Climate Change*, edited by S. Solomon et al., pp. 129–234, Cambridge Univ. Press, Cambridge, U. K.

Kelly, J. T., C. C. Chuang, and A. S. Wexler (2007), Influence of dust composition on cloud droplet formation, *Atmos. Environ.*, *41*(14), 2904–2916.

Labban, R., J. M. Veranth, J. C. Chow, J. L. P. Engelbrecht, and J. G. Watson (2004), Size and geographical variation in PM1, PM2.5 and PM10: Source profiles from soils in the western United States, *Water Air Soil Pollut.*, *157*(1–4), 13–31.

Lowenthal, D., B. Zielinska, B. Mason, S. Samy, V. Samburova, D. Collins, C. Spencer, N. Taylor, J. Allen, and N. Kumar (2009), Aerosol characterization studies at Great Smoky Mountains National Park, summer 2006, *J. Geophys. Res.*, *114*, D08206, doi:10.1029/2008JD011274.

Malm, W. C., J. F. Sisler, D. Huffman, R. A. Eldred, and T. A. Cahill (1994), Spatial and seasonal trends in particle concentration and optical extinction in the United States, *J. Geophys. Res.*, *99*(D1), 1347–1370.

Malm, W. C., B. A. Schichtel, M. L. Pitchford, L. L. Ashbaugh, and R. A. Eldred (2004), Spatial and monthly trends in speciated fine particle concentration in the United States, *J. Geophys. Res.*, *109*, D03306, doi:10.1029/2003JD003739.

McFiggans, G., et al. (2006), The effect of physical and chemical aerosol properties on warm cloud droplet activation, *Atmos. Chem. Phys.*, *6*, 2593–2649.

Mircea, M., et al. (2005), Importance of the organic aerosol fraction for modeling aerosol hygroscopic growth and activation: A case study in the Amazon Basin, *Atmos. Chem. Phys.*, *5*, 3111–3126.

Nenes, A., R. J. Charlson, M. C. Facchini, M. Kulmala, A. Laaksonen, and J. H. Seinfeld (2002), Can chemical effects on cloud droplet number rival the first indirect effect?, *Geophys. Res. Lett.*, *29*(17), 1848, doi:10.1029/2002GL015295.

Niemeyer, T. C., D. A. Gillette, J. J. Deluisi, Y. J. Kim, W. F. Niemeyer, T. Ley, T. E. Gill, and D. Ono (1999), Optical depth, size distribution and flux of dust from Owens Lake, California, *Earth Surf. Processes Landforms*, *24*(5), 463–479.

Pio, C. A., et al. (2007), Climatology of aerosol composition (organic versus inorganic) at nonurban sites on a west-east transect across Europe, *J. Geophys. Res.*, *112*, D23S02, doi:10.1029/2006JD008038.

Pringle, K. J., K. S. Carslaw, D. V. Spracklen, G. M. Mann, and M. P. Chipperfield (2009), The relationship between aerosol and cloud drop number concentrations in a global aerosol microphysics model, *Atmos. Chem. Phys.*, *9*(12), 4131–4144.

Seidl, W. (1989), Ionic concentrations and initial S(IV)-oxidation rates in droplets during the condensational stage of cloud, *Tellus, Ser. B*, *41*, 32–50.

Seinfeld, J. H., and S. N. Pandis (2006), *Atmospheric Chemistry and Physics: From Air Pollution to Climate Change*, 2nd ed., J. Wiley, Hoboken, N. J.

Topping, D. O., G. B. McFiggans, G. Kiss, Z. Varga, M. C. Facchini, S. Decesari, and M. Mircea (2007), Surface tensions of multi-component mixed inorganic/organic aqueous systems of atmospheric significance: Measurements, model predictions and importance for cloud activation predictions, *Atmos. Chem. Phys.*, *7*(9), 2371–2398.

Xue, H. W., A. M. Moyle, N. Magee, J. Y. Harrington, and D. Lamb (2005), Experimental studies of droplet evaporation kinetics: Validation of models for binary and ternary aqueous solutions, *J. Atmos. Sci.*, *62*(12), 4310–4326.

E. L. Roesler and J. E. Penner, Department of Atmospheric, Oceanic, and Space Sciences, University of Michigan, Space Research Building, 2455 Hayward St., Ann Arbor, MI 48109-2143, USA. (eroesler@umich.edu)

## D.1 Additional Commentary

Much information and literature was compiled for the production of the *Roesler and Penner* (2010)paper. A few of these ideas from the published literature and Parcel Undergoing Thermodynamic Transitions (PUTT) are listed here but not discussed in *Roesler and Penner* (2010).

*Chuang et al.* (2002)discussed kinetic limitations of droplet formation in clouds. *Wex et al.* (2010)derived many $\kappa$ [1] values based on world-wide chemical compositions and asserted that knowledge of the mixing state of a particle is necessary in order to predict the number of cloud condensation nuclei (CCN). They also state that bulk or size-resolved composition information is insufficient to predict the number of CCN. *Ward et al.* (2010)applied applied aerosol composition data to a larger-scale model by using the $\kappa$ values from a Lagrangian parcel model to constrain look-up tables in a regional model, Regional Atmospheric Modeling System (RAMS).

When using PUTT to calculate activated CCN in bins, if the accumulation and coarse modes had the same composition, the maximum bin and minimum bin values were the same. This suggests that the model ran correctly. When the number of aerosols, aerosol concentration ($N_A$), in both modes was different, the maximum bin and minimum bin values would change. The same size range of aerosols does not activate when $N_A$ changes, and when a higher number of droplet concentration ($N_D$) were produced, smaller bin values are activated.

In the results from *Roesler and Penner* (2010), the seasonal results of total $N_D$ show that Fall and Winter (Spring and Summer) behave similarly. This is probably caused by seasonal differences in the nitric acid gas ($HNO_{3(g)}$) concentrations. For example, the Northeastern

[1] a parameter commonly used to describe aerosol hygroscopicity described in *Petters and Kreidenweis* (2007)

regions of the United States show the seasonal differences in $N_D$ when parameters related to the nitric acid gas are altered. The difference between the regions could be reduced by decreasing the range of initial gas concentrations between the regions and seasons or increasing the size distribution. The greatest amount of variation in $N_D$ was caused by the large range of $N_A$ between regions.

# BIBLIOGRAPHY

# BIBLIOGRAPHY


Adachi, K., and P. R. Buseck (2008), Internally mixed soot, sulfates, and organic matter in aerosol particles from mexico city, *Atmospheric Chemistry and Physics*, *8*(21), 6469–6481.

Adachi, K., S. H. Chung, and P. R. Buseck (2010), Shapes of soot aerosol particles and implications for their effects on climate, *Journal of Geophysical Research-Atmospheres*, *115*, –.

Adams, B. M., W. J. Bohnhoff, K. R. Dalbey, J. P. Eddy, M. S. Eldred, D. M. Gay, K. Haskell, P. Hough, and L. P. Swiler (2009), Dakota, a multilevel parallel object-oriented framework for design optimization, parameter estimation, uncertainty quantification, and sensitivity analysis: Version 5.0 user's manual, *Tech. rep.*, Sandia National Labs.

Aldama, A. A. (1990), *Filtering techniques for turbulent flow simulation*, Lecture notes in engineering ;56, Springer-Verlag, Berlin ; New York, viii, 397 p. Includes bibliographical references.

AMSGlossary (2012), Ams glossary.

Barrie, L. A. (1986), Arctic air-pollution - an overview of current knowledge, *Atmospheric Environment*, *20*(4), 643–663.

Bechmann, A. (2006), Large-eddy simulations of atmopsheric flow over complex terrain, Ph.D. thesis, Technical University of Denmark.

Bougeault, P. (1981), Modeling the trade-wind cumulus boundary-layer .2. a high-order one-dimensional model, *Journal of the Atmospheric Sciences*, *38*(11), 2429–2439, mx554 Times Cited:43 Cited References Count:31.

Bougeault, P., and J. C. Andre (1986), On the stability of the 3rd-order turbulence closure for the modeling of the stratocumulus-topped boundary-layer, *Journal of the Atmospheric Sciences*, *43*(15), 1574–1581, d7884 Times Cited:37 Cited References Count:19.

Chuang, C. C., J. E. Penner, J. M. Prospero, K. E. Grant, G. H. Rau, and K. Kawamoto (2002), Cloud susceptibility and the first aerosol indirect forcing: Sensitivity to black carbon and aerosol concentrations, *Journal of Geophysical Research-Atmospheres*, *107*(D21).

Curry, J. A., and E. E. Ebert (1992), Annual cycle of radiation fluxes over the arctic-ocean - sensitivity to cloud optical-properties, *Journal of Climate*, *5*(11), 1267–1280.

Curry, J. A., W. B. Rossow, D. Randall, and J. L. Schramm (1996), Overview of arctic cloud and radiation characteristics, *Journal of Climate*, *9*(8), 1731–1764.

Davidson, C. I., R. F. Phalen, and P. A. Solomon (2005), Airborne particulate matter and human health: A review, *Aerosol Science and Technology*, *39*(8), 737–749.

de Boer, G., E. W. Eloranta, and M. D. Shupe (2009), Arctic mixed-phase stratiform cloud properties from multiple years of surface-based measurements at two high-latitude locations, *Journal of the Atmospheric Sciences*, *66*(9), 2874–2887.

Deardorff, J. W. (1980a), Stratocumulus-capped mixed layers derived from a 3-dimensional model, *Boundary-Layer Meteorology*, *18*(4), 495–527.

Deardorff, J. W. (1980b), Cloud top entrainment instability, *Journal of the Atmospheric Sciences*, *37*(1), 131–147.

Deser, C., J. Walsh, and M. Timlin (2000), Arctic sea ice variability in the context of recent atmospheric circulation trends, *Journal of Climate*, *13*(3), 617–633.

Durran, D. R. (1991), The third-order adams-bashforth method: An attractive alternative to leapfrog time differencing, *Monthly Weather Review*, *119*(3), 702–720, doi: 10.1175/1520-0493(1991)119¡0702:TTOABM¿2.0.CO;2.

Dyson, J. (1979), *The hot Arctic*, 1st american ed., Little, Brown, Boston.

Fan, J. W., R. Y. Zhang, G. H. Li, W. K. Tao, and X. W. Li (2007), Simulations of cumulus clouds using a spectral microphysics cloud-resolving model, *Journal of Geophysical Research-Atmospheres*, *112*(D4).

Fan, J. W., M. Ovtchinnikov, J. M. Comstock, S. A. McFarlane, and A. Khain (2009a), Ice formation in arctic mixed-phase clouds: Insights from a 3-d cloud-resolving model with size-resolved aerosol and cloud microphysics, *Journal of Geophysical Research-Atmospheres*, *114*, –.

Fan, J. W., T. L. Yuan, J. M. Comstock, S. Ghan, A. Khain, L. R. Leung, Z. Q. Li, V. J. Martins, and M. Ovchinnikov (2009b), Dominant role by vertical wind shear in regulating aerosol effects on deep convective clouds, *Journal of Geophysical Research-Atmospheres*, *114*, –.

Feingold, G., W. R. Cotton, S. M. Kreidenweis, and J. T. Davis (1999), The impact of giant cloud condensation nuclei on drizzle formation in stratocumulus: Implications for cloud radiative properties, *Journal of the Atmospheric Sciences*, *56*(24), 4100–4117.

Forster, P., V. Ramaswamy, P. Artaxo, T. Berntsen, R. Betts, D. Fahey, J. Haywood, J. Lean, D. Lowe, G. Myhre, J. Nganga, R. Prinn, G. Raga, M. Schulz, and R. Van Dorland (2007), Changes in atmospheric constituents and in radiative forcing, in *Climate Change*

*2007: The Physical Science Basis. Contribution of Working Group I to the Fourth Assessment Report of the Intergovernmental Panel on Climate Change*, edited by S. Solomon, D. Qin, M. Manning, Z. Chen, M. Marquis, K. Averyt, M. Tignor, and H. Miller, pp. viii, 996 p., Cambridge University, Cambridge, United Kingdom and New York, NY, USA.

Francis, J., and E. Hunter (2006), New insight into the disappearing arctic sea ice.

Francis, J. A., W. Chan, D. J. Leathers, J. R. Miller, and D. E. Veron (2009), Winter northern hemisphere weather patterns remember summer arctic sea ice extent, *Geophys. Res. Lett.*, *36*(7), L07,503.

Ghan, S. J., B. Schmid, J. Hubbe, C. Flynn, A. Laskin, A. Zelenyuk, D. Czizco, C. Long, G. McFarquhar, J. Verlinde, J. Harrington, W. Strapp, P. Liu, A. Korolev, A. McDonald, M. Wolde, A. Fridlind, T. Garrett, G. Mace, G. Kok, S. Brooks, D. Collins, D. Lubin, P. Lawson, M. Dubey, C. Mazzoleni, M. Shupe, S. Xie, D. Turner, Q. Min, E. Mlawer, and D. Mitchell (2007), Science overview document indirect and semi-direct aerosol campaign (isdac) april 2008.

Golaz, J. C., V. E. Larson, and W. R. Cotton (2002), A pdf-based model for boundary layer clouds. part i: Method and model description, *Journal of the Atmospheric Sciences*, *59*(24), 3540–3551.

Harrington, J. Y., T. Reisin, W. R. Cotton, and S. M. Kreidenweis (1999), Cloud resolving simulations of arctic stratus - part ii: Transition-season clouds, *Atmospheric Research*, *51*(1), 45–75.

Herman, G., and R. Goody (1976), Formation and persistence of summertime arctic stratus clouds, *Journal of the Atmospheric Sciences*, *33*(8), 1537–1553.

Hinze, J. O. (1975), *Turbulence*, 2d ed., McGraw-Hill, New York, 75005765 J. O. Hinze. ill. ; 24 cm. McGraw-Hill series in mechanical engineering Includes bibliographical references and indexes.

Hogan, R. J., A. L. M. Grant, A. J. Illingworth, G. N. Pearson, and E. J. O'Connor (2009), Vertical velocity variance and skewness in clear and cloud-topped boundary layers as revealed by doppler lidar, *Quarterly Journal of the Royal Meteorological Society*, *135*(640), 635–643, 452PB Times Cited:7 Cited References Count:25.

Holland, M. M., and C. M. Bitz (2003), Polar amplification of climate change in coupled models, *Climate Dynamics*, *21*(3), 221–232.

Huschke, R. E. (1969), Arctic cloud statistics from "air calibrated" surface weather observations, *Tech. rep.*, RAND Corporation.

Iguchi, T., T. Nakajima, A. P. Khain, K. Saito, T. Takemura, and K. Suzuki (2008), Modeling the influence of aerosols on cloud microphysical properties in the east asia region using a mesoscale model coupled with a bin-based cloud microphysics scheme, *Journal of Geophysical Research-Atmospheres*, *113*(D14), –.

Inc., M.-W. (2005), *The Merriam-Webster dictionary*, Merriam-Webster, Springfield, Mass.

Intrieri, J. M., C. W. Fairall, M. D. Shupe, P. O. G. Persson, E. L. Andreas, P. S. Guest, and R. E. Moritz (2002), An annual cycle of arctic surface cloud forcing at sheba, *Journal of Geophysical Research-Oceans*, *107*(C10).

Judah, L. C., C. F. Jason, A. B. Mathew, A. A. Vladimir, and E. C. Jessica (), Arctic warming, increasing snow cover and widespread boreal winter cooling, *Environmental Research Letters*, *7*(1), 014,007.

Kaufman, D. S., D. P. Schneider, N. P. McKay, C. M. Ammann, R. S. Bradley, K. R. Briffa, G. H. Miller, B. L. Otto-Bliesner, J. T. Overpeck, B. M. Vinther, and A. L. k. P. Members (2009), Recent warming reverses long-term arctic cooling, *Science*, *325*(5945), 1236–1239.

Kay, J. E., T. L'Ecuyer, A. Gettelman, G. Stephens, and C. O'Dell (2008), The contribution of cloud and radiation anomalies to the 2007 arctic sea ice extent minimum, *Geophysical Research Letters*, *35*(8), –.

Khain, A., and A. Pokrovsky (2004), Simulation of effects of atmospheric aerosols on deep turbulent convective clouds using a spectral microphysics mixed-phase cumulus cloud model. part ii: Sensitivity study, *Journal of the Atmospheric Sciences*, *61*(24), 2983–3001.

Khain, A., A. Pokrovsky, M. Pinsky, A. Seifert, and V. Phillips (2004), Simulation of effects of atmospheric aerosols on deep turbulent convective clouds using a spectral microphysics mixed-phase cumulus cloud model. part i: Model description and possible applications, *Journal of the Atmospheric Sciences*, *61*(24), 2963–2982.

Khain, A., D. Rosenfeld, and A. Pokrovsky (2005), Aerosol impact on the dynamics and microphysics of deep convective clouds, *Quarterly Journal of the Royal Meteorological Society*, *131*(611), 2639–2663.

Khain, A., N. Cohen, B. Lynn, and A. Pokrovsky (2008a), Possible aerosol effects on lightning activity and structure of hurricanes, *Journal of the Atmospheric Sciences*, *65*(12), 3652–3677.

Khain, A., B. Lynn, and J. Dudhia (2010), Aerosol effects on intensity of landfalling hurricanes as seen from simulations with the wrf model with spectral bin microphysics, *Journal of the Atmospheric Sciences*, *67*(2), 365–384.

Khain, A., D. Rosenfeld, A. Pokrovsky, U. Blahak, and A. Ryzhkov (2011), The role of ccn in precipitation and hail in a mid-latitude storm as seen in simulations using a spectral (bin) microphysics model in a 2d dynamic frame, *Atmospheric Research*, *99*(1), 129–146.

Khain, A. P., N. BenMoshe, and A. Pokrovsky (2008b), Factors determining the impact of aerosols on surface precipitation from clouds: An attempt at classification, *Journal of the Atmospheric Sciences*, *65*(6), 1721–1748.

Khain, A. P., L. R. Leung, B. Lynn, and S. Ghan (2009), Effects of aerosols on the dynamics and microphysics of squall lines simulated by spectral bin and bulk parameterization schemes, *Journal of Geophysical Research-Atmospheres*, *114*, –.

Khairoutdinov, M. F., and D. A. Randall (2003), Cloud resolving modeling of the arm summer 1997 iop: Model formulation, results, uncertainties, and sensitivities, *Journal of the Atmospheric Sciences*, *60*(4), 607–625.

Khalizov, A. F., R. Y. Zhang, D. Zhang, H. X. Xue, J. Pagels, and P. H. McMurry (2009), Formation of highly hygroscopic soot aerosols upon internal mixing with sulfuric acid vapor, *Journal of Geophysical Research-Atmospheres*, *114*, –.

Klein, S. A., R. B. McCoy, H. Morrison, A. S. Ackerman, A. Avramov, G. d. Boer, M. Chen, J. N. S. Cole, A. D. Del Genio, M. Falk, M. J. Foster, A. Fridlind, J.-C. Golaz, T. Hashino, J. Y. Harrington, C. Hoose, M. F. Khairoutdinov, V. E. Larson, X. Liu, Y. Luo, G. M. McFarquhar, S. Menon, R. A. J. Neggers, S. Park, M. R. Poellot, J. M. Schmidt, I. Sednev, B. J. Shipway, M. D. Shupe, D. A. Spangenberg, Y. C. Sud, D. D. Turner, D. E. Veron, K. v. Salzen, G. K. Walker, Z. Wang, A. B. Wolf, S. Xie, K.-M. Xu, F. Yang, and G. Zhang (2009), Intercomparison of model simulations of mixed-phase clouds observed during the arm mixed-phase arctic cloud experiment. i: Single-layer cloud, *Quarterly Journal of the Royal Meteorological Society*, *135*(641), 979–1002.

Koch, D., and A. D. Del Genio (2010), Black carbon semi-direct effects on cloud cover: review and synthesis, *Atmospheric Chemistry and Physics*, *10*(16), 7685–7696, 645ED Times Cited:38 Cited References Count:48.

Larour, E., J. Schiermeier, E. Rignot, H. Seroussi, M. Morlighem, and J. Paden (2012), Sensitivity analysis of pine island glacier ice flow using issm and dakota, *Journal of Geophysical Research-Earth Surface*, *117*.

Larson, V. E., J.-C. Golaz, and W. R. Cotton (2002), Small-scale and mesoscale variability in cloudy boundary layers: Joint probability density functions, *Journal of the Atmospheric Sciences*, *59*(24), 3519–3539, doi: 10.1175/1520-0469(2002)059¡3519:SSAMVI¿2.0.CO;2.

Lemke, P., J. Ren, R. Alley, I. Allison, J. Carrasco, G. Flato, Y. Fujii, G. Kaser, P. Mote, R. Thomas, and T. Zhang (2007), Observations: Changes in snow, ice and frozen ground, in *Climate Change 2007: The Physical Science Basis. Contribution of Working Group I to the Fourth Assessment Report of the Intergovernmental Panel on Climate Change*, edited by S. Solomon, D. Qin, M. Manning, Z. Chen, M. Marquis, K. Averyt, M. Tignor, and H. Miller, Cambridge University Press, Cambridge, United Kingdom and New York, NY, USA.

Leonard, A., F. N. Frenkiel, and R. E. Munn (1975), Energy cascade in large-eddy simulations of turbulent fluid flows, in *Advances in Geophysics*, vol. Volume 18, Part A, pp. 237–248, Elsevier, doi: 10.1016/S0065-2687(08)60464-1.

Li, X. W., W. K. Tao, A. P. Khain, J. Simpson, and D. E. Johnson (2009a), Sensitivity of a cloud-resolving model to bulk and explicit bin microphysical schemes. part i: Comparisons, *Journal of the Atmospheric Sciences*, *66*(1), 3–21.

Li, X. W., W. K. Tao, A. P. Khain, J. Simpson, and D. E. Johnson (2009b), Sensitivity of a cloud-resolving model to bulk and explicit bin microphysical schemes. part ii: Cloud microphysics and storm dynamics interactions, *Journal of the Atmospheric Sciences*, *66*(1), 22–40.

Luo, Y. L., K. M. Xu, H. Morrison, and G. McFarquhar (2008), Arctic mixed-phase clouds simulated by a cloud-resolving model: Comparison with arm observations and sensitivity to microphysics parameterizations, *Journal of the Atmospheric Sciences*, *65*(4), 1285–1303.

Lynn, B., and A. Khain (2007), Utilization of spectral bin microphysics and bulk parameterization schemes to simulate the cloud structure and precipitation in a mesoscale rain event, *Journal of Geophysical Research-Atmospheres*, *112*(D22), –.

Lynn, B., A. Khain, D. Rosenfeld, and W. L. Woodley (2007), Effects of aerosols on precipitation from orographic clouds, *J. Geophys. Res.*, *112*(D10), D10,225.

Lynn, B. H., A. P. Khain, J. Dudhia, D. Rosenfeld, A. Pokrovsky, and A. Seifert (2005a), Spectral (bin) microphysics coupled with a mesoscale model (mm5). part i: Model description and first results, *Monthly Weather Review*, *133*(1), 44–58.

Lynn, B. H., A. P. Khain, J. Dudhia, D. Rosenfeld, A. Pokrovsky, and A. Seifert (2005b), Spectral (bin) microphysics coupled with a mesoscale model (mm5). part ii: Simulation of a cape rain event with a squall line, *Monthly Weather Review*, *133*(1), 59–71.

Magaritz, L., M. Pinsky, O. Krasnov, and A. Khain (2009), Investigation of droplet size distributions and drizzle formation using a new trajectory ensemble model. part ii: Lucky parcels, *Journal of the Atmospheric Sciences*, *66*(4), 781–805.

McFarquhar, G. M., G. Zhang, M. R. Poellot, G. L. Kok, R. Mccoy, T. Tooman, A. Fridlind, and A. J. Heymsfield (2007), Ice properties of single-layer stratocumulus during the mixed-phase arctic cloud experiment: 1. observations, *Journal of Geophysical Research-Atmospheres*, *112*(D24), –.

McFarquhar, G. M., S. Ghan, J. Verlinde, A. Korolev, J. W. Strapp, B. Schmid, J. M. Tomlinson, M. Wolde, S. D. Brooks, D. Cziczo, M. K. Dubey, J. W. Fan, C. Flynn, I. Gultepe, J. Hubbe, M. K. Gilles, A. Laskin, P. Lawson, W. R. Leaitch, P. Liu, X. H. Liu, D. Lubin, C. Mazzoleni, A. M. Macdonald, R. C. Moffet, H. Morrison, M. Ovchinnikov, M. D. Shupe, D. D. Turner, S. C. Xie, A. Zelenyuk, K. Bae, M. Freer, and A. Glen (2011), Indirect and semi-direct aerosol campaign the impact of arctic aerosols on clouds, *Bulletin of the American Meteorological Society*, *92*(2), 183–+.

Morrison, H., J. A. Curry, and V. I. Khvorostyanov (2005), A new double-moment microphysics parameterization for application in cloud and climate models. part i: Description, *Journal of the Atmospheric Sciences*, *62*(6), 1665–1677.

Morrison, H., P. Zuidema, A. S. Ackerman, A. Avramov, G. de Boer, J. W. Fan, A. M. Fridlind, T. Hashino, J. Y. Harrington, Y. L. Luo, M. Ovchinnikov, and B. Shipway (2011), Intercomparison of cloud model simulations of arctic mixed-phase boundary layer clouds observed during sheba/fire-ace, *Journal of Advances in Modeling Earth Systems*, *3*.

Morrison, H., G. de Boer, G. Feingold, J. Harrington, M. D. Shupe, and K. Sulia (2012), Resilience of persistent arctic mixed-phase clouds, *Nature Geoscience*, *5*(1), 11–17.

Noppel, H., A. Pokrovsky, B. Lynn, A. P. Khain, and K. D. Beheng (2010), A spatial shift of precipitation from the sea to the land caused by introducing submicron soluble aerosols: Numerical modeling, *Journal of Geophysical Research-Atmospheres*, *115*, –.

Ovchinnikov, M., A. Korolev, and J. W. Fan (2011), Effects of ice number concentration on dynamics of a shallow mixed-phase stratiform cloud, *Journal of Geophysical Research-Atmospheres*, *116*.

Peixoto, J. P., and A. H. Oort (1992), *Physics of climate*, American Institute of Physics, New York.

Peterson, K., P. Bochev, and B. Paskaleva (2010), Development, sensitivity analysis, and uncertainty quantification of high-fidelity arctic sea ice models, *Tech. rep.*, Sandia National Laboratories.

Petters, M. D., and S. M. Kreidenweis (2007), A single parameter representation of hygroscopic growth and cloud condensation nucleus activity, *Atmospheric Chemistry and Physics*, *7*(8), 1961–1971.

Pinto, J. O. (1998), Autumnal mixed-phase cloudy boundary layers in the arctic, *Journal of the Atmospheric Sciences*, *55*(11), 2016–2038.

Pruppacher, H. R., and J. D. Klett (1997), *Microphysics of clouds and precipitation*, Atmospheric and oceanographic sciences library, 2nd rev. and enl. ed., Kluwer Academic Publishers, Dordrecht ; Boston.

Przybylak, R. (2003), *The climate of the Arctic*, Atmospheric and oceanographic sciences library, Kluwer Academic Publishers, Dordrecht Boston.

Quinn, P. K., G. Shaw, E. Andrews, E. G. Dutton, T. Ruoho-Airola, and S. L. Gong (2007), Arctic haze: current trends and knowledge gaps, *Tellus Series B-Chemical and Physical Meteorology*, *59*(1), 99–114.

Ramanathan, V., C. Chung, D. Kim, T. Bettge, L. Buja, J. T. Kiehl, W. M. Washington, Q. Fu, D. R. Sikka, and M. Wild (2005), Atmospheric brown clouds: Impacts on south asian climate and hydrological cycle, *Proceedings of the National Academy of Sciences of the United States of America*, *102*(15), 5326–5333.

Randall, D. A. (1980), Conditional instability of the 1st kind upside-down, *Journal of the Atmospheric Sciences*, *37*(1), 125–130.

Roesler, E. L., and J. E. Penner (2010), Can global models ignore the chemical composition of aerosols?, *Geophysical Research Letters*, *37*.

Schlichting, H. (1968), *Boundary-layer theory*, McGraw-Hill series in mechanical engineering, 6th ed., McGraw-Hill, New York,, 67029199 Translated by J. Kestin. illus. 24 cm. Translation of Grenzschicht-Theorie. Includes bibliographies.

Schweiger, A. J., R. W. Lindsay, S. Vavrus, and J. A. Francis (2008), Relationships between arctic sea ice and clouds during autumn, *Journal of Climate*, *21*(18), 4799–4810.

Seifert, A., A. Khain, A. Pokrovsky, and K. D. Beheng (2006), A comparison of spectral bin and two-moment bulk mixed-phase cloud microphysics, *Atmospheric Research*, *80*(1), 46–66.

Seinfeld, J. H., and S. N. Pandis (2006), *Atmospheric chemistry and physics : from air pollution to climate change*, 2nd ed., J. Wiley, Hoboken, N.J.

Serreze, M., and J. Francis (2006), The arctic amplification debate, *Climatic Change*, *76*(3), 241–264.

Serreze, M., A. Barrett, A. Slater, M. Steele, J. Zhang, and K. Trenberth (2007), The large-scale energy budget of the arctic, *Journal of geophysical research*, *112*(d11), D11,122.

Serreze, M. C., A. P. Barrett, J. C. Stroeve, D. N. Kindig, and M. M. Holland (2009a), The emergence of surface-based arctic amplification, *The Cryosphere*, *3*(1), 11–19.

Serreze, M. C., J. Stroeve, C. Mauritzen, A. Cazenave, E. Rignot, N. R. Bates, J. Canadell, M. Raupach, N. Shakhova, and I. Semiletov (2009b), Arctic climate feedbacks: Global implications, *Tech. rep.*, World Wildlife Federation International Arctic Programme.

Shupe, M. D., T. Uttal, and S. Y. Matrosov (2005a), Arctic cloud microphysics retrievals from surface-based remote sensors at sheba, *Journal of Applied Meteorology*, *44*(10), 1544–1562.

Shupe, M. D., T. Uttal, and S. Y. Matrosov (2005b), Arctic cloud microphysics retrievals from surface-based remote sensors at sheba, *Journal of Applied Meteorology*, *44*(10), 1544–1562.

Shupe, M. D., S. Y. Matrosov, and T. Uttal (2006), Arctic mixed-phase cloud properties derived from surface-based sensors at sheba, *Journal of the Atmospheric Sciences*, *63*(2), 697–711.

Smagorinsky, J. (1963), General circulation experiments with the primitive equations, *Monthly Weather Review*, *91*(3), 99–164, doi: 10.1175/1520-0493(1963)091¡0099:GCEWTP¿2.3.CO;2.

Smith, G. W. (1982), A simple nucleation depletion model for the spherule size of particulate carbon, *Combustion and Flame*, *48*(3), 265–272.

Solomon, A., M. D. Shupe, P. O. G. Persson, and H. Morrison (2011), Moisture and dynamical interactions maintaining decoupled arctic mixed-phase stratocumulus in the presence of a humidity inversion, *Atmospheric Chemistry and Physics*, *11*(19), 10,127–10,148.

Suzuki, K., T. Nakajma, T. Y. Nakajima, and A. P. Khain (2010), A study of microphysical mechanisms for correlation patterns between droplet radius and optical thickness of warm clouds with a spectral bin microphysics cloud model, *Journal of the Atmospheric Sciences*, *67*(4), 1126–1141.

Tannehill, J. C., D. A. Anderson, and R. H. Pletcher (1997), *Computational fluid mechanics and heat transfer*, Series in computational and physical processes in mechanics and thermal sciences, 2nd ed., Taylor and Francis, Washington, DC, 96041097 John C. Tannehill, Dale A. Anderson, Richard H. Pletcher. ill. ; 25 cm. Anderson's name appears first on the earlier ed. Includes bibliographical references (p. 745-782) and index.

Tao, W. K., X. W. Li, A. Khain, T. Matsui, S. Lang, and J. Simpson (2007), Role of atmospheric aerosol concentration on deep convective precipitation: Cloud-resolving model simulations, *Journal of Geophysical Research-Atmospheres*, *112*(D24), –.

Tremblay, L. B., and L. A. Mysak (1997), The possible effects of including ridge-related roughness in air-ice drag parameterization: a sensitivity study, in *Annals of Glaciology, Vol 25, 1997: Papers from the International Symposium on Representation of the Cryosphere in Climate and Hydrological Models Held at Victoria, British Columbia, Canada, 12-15 August 1996*, *Annals of Glaciology*, vol. 25, pp. 22–25, Int Glaciological Soc, Cambridge.

Trenberth, K., P. Jones, P. Ambenje, R. Bojariu, D. Easterling, A. Klein Tank, D. Parker, F. Rahimzadeh, J. Renwick, M. Rusticucci, B. Soden, and P. Zhai (2007), Observations: Surface and atmospheric climate change, in *Climate Change 2007: The Physical Science Basis. Contribution of Working Group I to the Fourth Assessment Report of the Intergovernmental Panel on Climate Change*, edited by S. Solomon, D. Qin, M. Manning, Z. Chen, M. Marquis, K. Averyt, M. Tignor, and H. Miller, Cambridge University Press, Cambridge, United Kingdom and New York, NY, USA.

Trenberth, K. E., J. T. Fasullo, and J. Kiehl (2009), Earth's global energy budget, *Bulletin of the American Meteorological Society*, *90*(3), 311–+.

Walsh, J. E., W. L. Chapman, V. Romanovsky, J. H. Christensen, and M. Stendel (2008), Global climate model performance over alaska and greenland, *Journal of Climate*, *21*(23), 6156–6174.

Ward, D. S., T. Eidhammer, W. R. Cotton, and S. M. Kreidenweis (2010), The role of the particle size distribution in assessing aerosol composition effects on simulated droplet activation, *Atmospheric Chemistry and Physics*, *10*(12), 5435–5447.

Weingartner, E., U. Baltensperger, and H. Burtscher (1995), Growth and structural-change of combustion aerosols at high relative-humidity, *Environmental Science and Technology*, *29*(12), 2982–2986.

Wex, H., G. McFiggans, S. Henning, and F. Stratmann (2010), Influence of the external mixing state of atmospheric aerosol on derived ccn number concentrations, *Geophysical Research Letters*, *37*.

Wohlforth, C. P. (2004), *The whale and the supercomputer : on the northern front of climate change*, 1st ed., North Point Press, New York.

Xie, S. C., S. A. Klein, M. H. Zhang, J. J. Yio, R. T. Cederwall, and R. McCoy (2006), Developing large-scale forcing data for single-column and cloud-resolving models from the mixed-phase arctic cloud experiment, *Journal of Geophysical Research-Atmospheres*, *111*(D19).

Xiquan, D., X. Baike, K. Crosby, C. Long, and R. Stone (2009), A 10-year climatology of arctic cloud fractions and their impact on surface radiation budget at barrow, alaska.

Yin, Y., Z. Levin, T. G. Reisin, and S. Tzivion (2000), The effects of giant cloud condensation nuclei on the development of precipitation in convective clouds - a numerical study, *Atmospheric Research*, *53*(1-3), 91–116.

Zelenyuk, A., D. Imre, M. Earle, R. Easter, A. Korolev, R. Leaitch, P. Liu, A. M. Macdonald, M. Ovchinnikov, and W. Strapp (2010), In situ characterization of cloud condensation nuclei, interstitial, and background particles using the single particle mass spectrometer, splat ii, *Analytical Chemistry*, *82*(19), 7943–7951.

Zhang, D., and R. Y. Zhang (2005), Laboratory investigation of heterogeneous interaction of sulfuric acid with soot, *Environmental Science and Technology*, *39*(15), 5722–5728.

Zhang, M. H., and J. L. Lin (1997), Constrained variational analysis of sounding data based on column-integrated budgets of mass, heat, moisture, and momentum: Approach and application to arm measurements, *Journal of the Atmospheric Sciences*, *54*(11), 1503–1524.

Zhang, M. H., J. L. Lin, R. T. Cederwall, J. J. Yio, and S. C. Xie (2001), Objective analysis of arm iop data: Method and sensitivity, *Monthly Weather Review*, *129*(2), 295–311.

Zhang, R. Y., A. F. Khalizov, J. Pagels, D. Zhang, H. X. Xue, and P. H. McMurry (2008), Variability in morphology, hygroscopicity, and optical properties of soot aerosols during atmospheric processing, *Proceedings of the National Academy of Sciences of the United States of America*, *105*(30), 10,291–10,296.